Publication Series of the John von Neumann Institute for Computing (NIC)
NIC Series Volume 12

John von Neumann Institute for Computing (NIC)

Yu-cheng Lin

Strongly Disordered Quantum Spin Systems in Low Dimensions:

Numerical Study of Spin Chains, Spin Ladders and Two-Dimensional Systems

NIC Series Volume 12 ISBN 3-00-009056-8

Research Group Complex Systems

Die Deutsche Bibliothek – CIP-Cataloguing-in-Publication-Data
A catalogue record for this publication is available from Die Deutsche Bibliothek

Publisher: NIC-Directors
Distributor: NIC-Secretariat
Research Centre Jülich
52425 Jülich
Germany
Internet: www.fz-juelich.de/nic
Printer: Graphische Betriebe, Forschungszentrum Jülich

NIC Series Volume 12 ISBN 3-00-009056-8

Strongly Disordered Quantum Spin Systems in Low Dimensions:
Numerical Study of Spin Chains, Spin Ladders and Two-Dimensional Systems

Inaugural - Dissertation

zur

Erlangung des Doktorgrades

der Mathematisch-Naturwissenschaftlichen Fakultät

der Universität zu Köln

vorgelegt von

YU-CHENG LIN

aus Tainan, Taiwan

JOHN VON NEUMANN-INSTITUT FÜR COMPUTING
FORSCHUNGSZENTRUM JÜLICH

2002

Berichterstatter: Prof. Dr. H. RIEGER
Prof. Dr. D. STAUFFER

Tag der mündlichen Prüfung: 10. Dezember 2001

Contents

Chapter 1

Introduction to Quantum Phase Transitions with Disorder

Very recently, quantum spin systems have been studied intensively in the context of investigations on their zero-temperature (quantum) phase transitions. In particular, disorder effects arising from quenched randomness are novel phenomena observed in some low-dimensional quantum spin systems. In this thesis, we examine the rich physical properties of random quantum spin systems at criticality and in the off-critical phases from numerical aspects.

The thesis is organized as follows: We begin in this chapter with a brief account of some basic features of quantum phase transitions (good reviews can be found in e.g. [118], [123], [68] and [52]) and explain in what ways the quenched disorder affects the critical and the off-critical properties. The prototype of a quantum phase transition with/without disorder is the transverse-field Ising chain, which we will introduce also in this chapter. In Chapter 2 we describe a new quantum Monte Carlo method introduced by Rieger and Kawashima [99], which is based on the Swendsen-Wang cluster update method and the continuous time algorithm. We present our results of the transverse-field Ising model from Monte Carlo simulations in Chapter 3. Another numerical approach, which we used to study random quantum spin systems, is a strong-randomness renormalization group technique built on the perturbation theory [20, 21, 37, 41, 49]. In Chapter 4 we describe this renormalization group scheme and highlight the analytical results of some one-dimensional quantum spin systems, including the transverse-field Ising model, the antiferromagnetic XX- and XXX-chains. Our numerical studies using the renormalization group method are presented in Chapter 5-7. They include the transverse-field Ising model in two dimensions with a regular disorder distribution (Chapter 5), as well as with a highly singular disorder distribution (Chapter 6) and antiferromagnetic spin ladders (Chapter 7). A Summary is given in Chapter 8.

1.1 Continuous Quantum phase transitions

Quantum phase transitions[1] are transitions occur at the absolute zero of temperature $T = 0$, triggered by some non-thermal parameter, Δ, in the system, e.g. composition or the strength of an external magnetic field. For such a transition, there is no thermal energy, $k_B T = 0$, so that the critical fluctuations that destroy the long-range order are quantum fluctuations.

Like classical phase transitions, a quantum phase transition is characterized by a diverging length scale,

$$\xi \sim |\delta|^{-\nu} , \tag{1.1}$$

where $|\delta| \equiv |\Delta - \Delta_c|$ represents the distance from the quantum critical point, Δ_c, at $T = 0$, and ν is the correlation length exponent. Apart from the long-range correlation in space, phase transitions are generally accompanied by a diverging relaxation time ξ_τ, i.e., the time scale for the system to return to equilibrium after it has been disturbed, diverges as the transition is approached. This phenomenon is known as critical slowing down, and can be described as

$$\xi_\tau \sim \xi^z , \tag{1.2}$$

which defines the dynamical exponent, z. As a result, there is a characteristic frequency associated with the critical fluctuations that vanishes at criticality,

$$\omega_c \sim \xi_\tau^{-1} \sim |\delta|^{z\nu} . \tag{1.3}$$

For any finite-temperature phase transitions, the thermal energy $k_B T_c$ becomes much greater than the characteristic quantum of energy $\hbar\omega_c \to 0$. Hence, quantum effects are irrelevant for critical phenomena as long as $T_c \neq 0$. Such finite temperature phase transitions are referred to as classical or thermal phase transitions.

The physical properties of the quantum fluctuations are quite distinct from those of the thermal fluctuations responsible for classical, finite-temperature phase transitions. We then need a theoretical treatment of quantum phase transitions that somewhat different from that of classical ones.

1.2 The path-integral formulation of the quantum statistical mechanics

To see the crucial difference between a classical and quantum phase transition one has to realize, how statics and dynamics of the latter are inextricably linked, which we elaborate now.

[1] We will deal only with continuous phase transitions, and will use phase transitions as a shorthand for that.

One of the important task in statistical mechanics is to calculate the partition function $Z = \mathrm{Tr} e^{-\beta\mathcal{H}}$ of the considered system governed by a Hamiltonian $\mathcal{H}$, and the expectation values $\langle O\rangle = \mathrm{Tr}(Oe^{-\beta\mathcal{H}})/Z$ of the thermodynamic quantities of interest. For a quantum statistical system, the partition function is harder to evaluate because the quantum Hamiltonian $\mathcal{H}$ depends on non-commuting operators. One of the techniques for calculating the trace in the expression of Z is the Feynman's path-integral formulation of quantum mechanics [5]. In this formulation, Z takes the form of an integral of transition amplitudes for the system to start in some state $|q\rangle$ and return to the same state after an imaginary time interval $\tau = -i\beta$,

$$Z = \int dq \, \langle q| \, e^{-\beta\mathcal{H}} \, |q\rangle = \int dq \, \langle q, t_b| \, q, t_a\rangle \, |_{t_b - t_a = -i\beta}, \tag{1.4}$$

which is based on the observation that the density matrix $e^{-\beta\mathcal{H}}$ given in the partition function is formally identical to the expression for time-evolution operator $e^{-i\tau\mathcal{H}}$ (for convenience of notation we set $\hbar = 1$) if we replace the time interval τ with the imaginary value $\tau = -i\beta$. Following Feynman, the transition amplitude between two states of the system can be calculated by summing amplitudes for all possible paths between them. Formally the partition function can be written as a functional integral over the degrees of freedom $\{q\}$ and their canonical conjugates $\{p\}$

$$Z = \int \mathcal{D}p\mathcal{D}q \, e^{-\int_0^\beta \mathcal{L}(q,p)d\tau}, \tag{1.5}$$

where $\mathcal{L}$ is the Lagrangian. Since the Lagrangian has the form of an integral over a time interval $[0, \beta]$, we may regard (1.5) as the partition function for a classical system with classical action $\mathcal{S} = \int \mathcal{L}d\tau$, in which imaginary time appears as an extra dimension with a length β. In contrast to the classical phase transition, the statics and the dynamics of the quantum system are inextricably linked since the quantum Hamiltonian at some imaginary time does not commute with the Hamiltonian at another imaginary time.

This equivalence of the quantum and classical models may be helpful to see why quantum effects are irrelevant for finite temperature critical behavior [52, 68]. At any $T \neq 0$, the corresponding classical model of a d-dimensional quantum system is a slab in $d+1$ dimensions with an infinite spatial dimension but a finite temporal dimension of length $\beta = 1/T$ (we set $k_B \equiv 1$). As the transition is approached, the correlation length in the time direction ξ_τ grows and eventually exceeds the thickness of the slab, $\xi_\tau > \beta$, due to critical slowing down. Thus the system has now effectively d dimensions and behaves classically. However, when $T = 0$, the thickness in the time direction goes to infinite as in the space directions, the critical behavior is therefore not only controlled by the diverging correlation length in the space direction but also that in the time direction, i.e. we have to deal with a $(d + 1)$-dimensional problem which is equivalent to the quantum system with dominant quantum fluctuations at the transition.

There are also practical advantages of using this quantum-classical mapping. In many cases, the universality class of a quantum phase transition is one that has been studied for a classical system, and a great deal may already known about it. Moreover, it is possible to carry out classical Monte Carlo simulations of the appropriate $(d+1)$-dimensional model to study the quantum transitions in new universality classes. In Chapter 2 and 3 we will discuss more about this.

1.3 Examples of quantum phase transitions

The study of quantum phase transitions in not only of a theoretical interest. Recent experimental developments have indeed found hints of quantum phase transitions [118].

Consider for instance a quantum Ising ferromagnet - $LiHoF_4$ - investigated by Bitko and co-workers [57]. At low temperatures, the magnetic Ho^{+3} ions are in a doublet state that plays the role of the spin-1/2 eigenstates. The spins on neighboring ions are coupled by the magnetic dipolar interaction. Such an arrangement of spins on a lattice is known as an Ising model, which undergoes a paramagnet-ferromagnet phase transition at some finite temperature T_c. In Bitko's experiment, this material was placed in a magnetic field perpendicular to the spin ordering direction. Such a field induces quantum tunneling between the two states of each Ho ion. Increasing the strength of the applied field, the critical temperature T_c is found to decrease monotonically. If the strength of the magnetic field becomes larger than some critical value, the critical temperature T_c can be driven to zero and the ferromagnetic long-rang order will be destroyed exclusively by quantum fluctuations.

A theoretical model for $LiHoF_4$ in an applied transverse field can be described by the Hamiltonian

$$\mathcal{H} = -\sum_{<i,j>} J_{ij}\sigma_i^z\sigma_j^z - \sum_i h_i\sigma_i^x \ , \tag{1.6}$$

where σ_i^x, σ_i^z are Pauli matrices at site i, $J_{ij} = J > 0$ are nearest neighbor ferromagnetic interactions and the $h_i = h$ are transverse fields. If $\mathcal{H}$ involves only the σ_i^z, it reduces to the classical Ising model. The ferromagnetic interaction J describes the magnetic dipolar interactions between the spins, which tend to align the spins in a preferred directions. With the term proportional to h, the model becomes quantum mechanical since σ^x and σ^z do not commute. The external transverse magnetic field h tends to flip the orientation of the spins via a quantum mechanical tunneling motion. This model may be the easiest example of a quantum phase transition, and will be discussed further in this thesis.

As indicated previously, we can map a quantum model onto an effective classical model by using the imaginary-time path integral approach. The corresponding classical system for the transverse Ising model defined by (1.6) is the Ising model with an extra dimension representing the imaginary time evolution over a time length β. The exchange couplings in

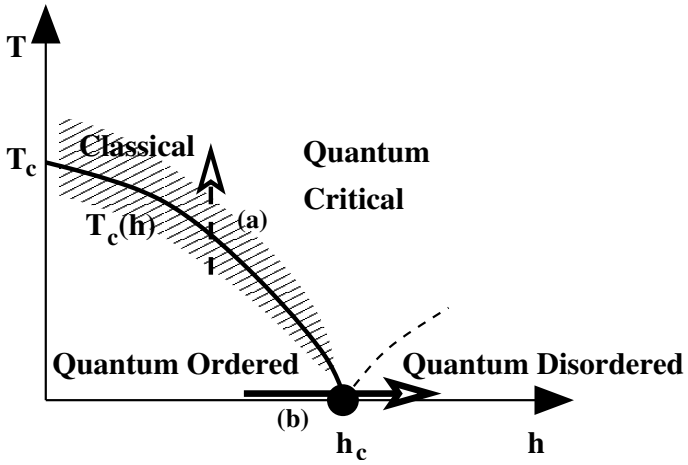

Figure 1.1: Phase diagram of a quantum Ising model in a transverse field. The figure corresponds to high dimensions $d > 1$, so a phase transition exists at nonzero temperature $T_c(h = 0) \neq 0$. The full line denotes the phase boundary $T_c(h)$ separating the ordered and disordered phase. As long as h is less than its critical value h_c, the system will undergo a phase transition from a ferromagnetic ordered phase to a paramagnetic phase, as the temperature is varied along (a) (the dashed line), which is classical and driven by thermal fluctuations. Alternatively, with a measurement along path (b) by varying the strength of the transverse field, we will observe the ferromagnet-paramagnet transition at the critical value h_c. This is the quantum phase transition we are interested in. For $d = 1$, the ordered phase is confined to zero temperature. (See the text for more information.).

the added imaginary time direction are associated with the transverse field h.[2] It has been analytically established that a d-dimensional transverse-field Ising model is in the same universality class as the $(d+1)$-dimensional classical Ising model, i.e. the critical exponents associated with the phase transition of the quantum system are identical to the critical exponents of the thermal phase transition in the equivalent $(d + 1)$-dimensional classical model [11, 12, 17]. Thus, for the pure case (without randomness in the system), we can apply the well known solutions of the classical Ising model to the quantum transverse Ising model.

Fig. 1.1 shows a schematic phase diagram for the transverse Ising model in the (h, T) plane [57, 50, 52]. The model in high dimensions $d > 1$ has a phase transition driven by thermal fluctuations at some finite temperature T_c. For $T_c(h) \neq 0$, critical fluctuations in the vicinity of the phase boundary between ordered and disordered phase are classical. This classical critical regime, the gray region in the diagram, becomes narrower with decreasing temperature and shrinks to zero at zero temperature at some strength of the transverse field, $h = h_c$, at which the critical exponents are expressed by those of the $(d + 1)$-dimensional Ising model. The critical point at h_c divides two phases: one is the quantum ordered phase

[2]This mapping to the classical model is the central part of the quantum Monte Carlo methods, and we will discuss it in more detail in Chapter 2.

in which quantum, as well as thermal, fluctuations are sufficiently weak ($h < h_c$, low T); the other is the quantum disordered phase in which the long-range order is destroyed mainly by quantum fluctuations ($h > h_c$, low T). Between the quantum disordered and the thermally disordered regions where thermal fluctuations dominate, there is an intermediate regime called the quantum critical regime [30], in which both quantum and thermal fluctuations are relevant. For $d = 1$, there is no phase transition at finite temperature, so the ordered phase is confined to the zero temperature

The diluted magnet $LiHo_xY_{1-x}F_4$ with non-magnetic Y^{3+} ions have also been investigated during the past few years [35, 39], and provided very useful experimental realizations of quantum spin glasses that undergo a quantum phase transition driven by an applied transverse field. In this case, quenched randomness appears and causes new physical phenomena, which we will discuss in the following section.

1.4 Effects of quenched randomness on quantum phase transitions

In this thesis we deal with quantum phase transitions mainly in the presence of quenched disorder, i.e. time-independent disorder. One important question to address is whether the critical behavior in a pure system is stable against disorder. According to the Harris criterion [14], if the correlation length exponent $\nu_{\rm pure}$ of a d-dimensional pure system obeys the inequality

$$\nu_{\rm pure} < 2/d \, , \tag{1.7}$$

the pure critical behavior is unstable, and weak randomness may lead to a different universality class. For the d-dimensional transverse-field Ising model, which is equivalent to the Ising model in $d + 1$ dimensions, the Harris criterion indicates that weak randomness is relevant at the pure critical point for $d < 4$, since $\nu_{\rm pure} = 1$ for $d = 1$, $\nu_{\rm pure} \approx 0.63$ for $d = 2$ and $\nu_{\rm pure} = 1/2$ for $d \geq 3$ are known [13, 113].

More profound effects of quenched disorder on quantum phase transitions have been found theoretically and experimentally, including Griffiths-McCoy singularities and activated dynamical scaling, which we will discuss in this section.

1.4.1 Griffiths-McCoy singularities

An effect of quenched disorder that has been known for a long time is a non-analytic behavior of the free energy in the regions even away from the critical point. This arises from rare regions that are locally in the "wrong phase", and was first discussed many years ago by Griffiths, in the context of classical diluted Ising ferromagnets [9]. In the paramagnetic phase, one can find some regions where the local quenched random variables

deviate strongly from their global averages. As a result of the deviations, these regions form strongly-coupled clusters and show local magnetic order, even though the global order in this phase vanishes. Since the local ordered regions have a large response to an external magnetic field h, they lead to a non-analytic free energy at $h = 0$ in the off-critical phase, called Griffiths phase. However, the probability of having such a strongly-coupled region is exponentially small. This is easy to understand by considering a diluted Ising ferromagnet below the percolation threshold $p < p_c$, where long-range order is not possible. If c is the concentration of magnetic atoms in the system, then the probability of having a connected big cluster involving $n = l^d$ atoms is $p(n) \approx c^n = e^{-n \ln(1/c)}$. Because of this small probability, the singularity arisen from the rare regions is very weak at a classical transition, all derivatives of the free energy with respect to h are finite [16].

The effects of such rare regions become stronger if the disorder is spatially correlated, and a diverging susceptibility can be found in whole region close to the critical point. This was first pointed out by McCoy [10] in the context of a classical two-dimensional Ising model with perfectly correlated disorder in one spatial direction and uncorrelated in the other [6, 7, 8]. The anisotropic model McCoy et al. studied is actually identical to the path-integral representation of the transverse-field Ising chain with quenched randomness,[3] which is based on the fact that quenched randomness depends only on space, but not on time. It is now understood that the rare regions discussed by Griffiths give a larger effect at a quantum phase transition than a classical one, and cause divergences of some physical quantities even away from the critical point. These effects are known as Griffiths-McCoy singularities.

To explain Griffiths-McCoy singularities in the quantum regime, let us consider the quantum Ising transverse Ising ferromagnet with quenched randomness, i.e. $J_{ij} > 0$ and/or $h_i > 0$ in (1.6) are random variables [55, 82]. In the quantum paramagnetic phase, the probability of a large locally-ordered cluster with linear length scale l is exponential small in the cluster volume, $p(l) \sim e^{-c_1 l^d}$, as in the classical case. In the picture of the quantum-classical mapping, the strongly coupled cluster propagates along the imaginary time direction and forms a "rod" (Fig. 1.2). To change the spin state of the rod requires inserting a domain wall, which costs an energy $c_2 l^d$ proportional to the volume in the space dimensions, where c_2 is a surface tension. This results in an exponentially large correlation time $\xi_\tau \sim e^{c_2 l^d}$ and, equivalently, a low-energy excitation $\varepsilon \sim \xi_\tau^{-1} \sim e^{-c_2 l^d}$. Consequently the density of low-energy excitations follows a power law:

$$\rho(\varepsilon) = \int dl^d \delta(\varepsilon - e^{-c_2 l^d}) e^{-c_1 l^d} \sim \varepsilon^{-1+d/z} , \tag{1.8}$$

where we have introduced a continuously varying exponent $z = c_2 d/c_1$. Note the lowest energy in a volume $V = L^d$ is $\varepsilon_{\min} \sim L^{-z}$, so z is a sort of dynamical exponent.

[3] The equivalence of the McCoy-Wu model and the random transverse Ising model will be shown in Section 2.1.

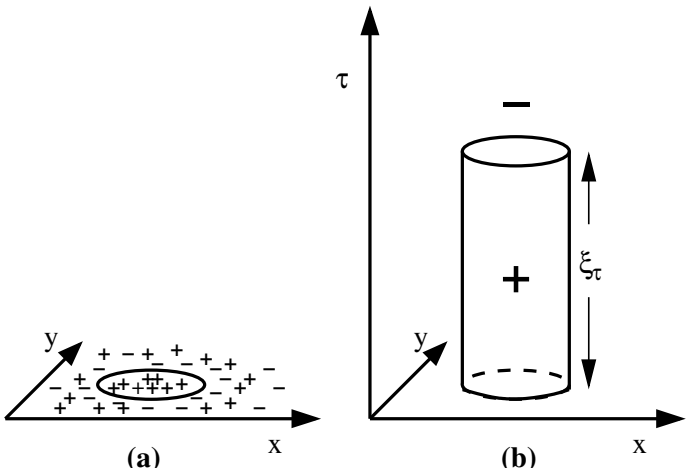

Figure 1.2: (a): a locally-ordered cluster of spatial volume $v \sim l^d$ in the paramagnetic phase. (b): In the quantum-classical mapping, this strongly coupled cluster tends to order the spins along the imaginary time direction, resulting in an exponentially large imaginary correlation time $\xi_\tau \sim e^{cl^d}$and, equivalently, a low-energy excitation $\varepsilon \sim \xi_\tau^{-1}$. (see text).

The small energy gaps with the probability distribution given in (1.8) are responsible for the large susceptibility. To see this, we consider the local static (zero frequency) susceptibility at zero temperature defined by

$$\chi_i^{\rm loc}(\omega = 0) = \int_0^\infty d\tau \langle C_i(\tau)\rangle \sim \sum_{m\neq 0} \frac{|\langle m|\, \sigma_i^z\, |0\rangle|^2}{\varepsilon_m}\ , \tag{1.9}$$

where $C_i(\tau) \equiv \langle 0|\, \sigma_i^z(\tau)\sigma_i^z(0)\, |0\rangle = \sum_m e^{-\varepsilon_m \tau}\, |\langle m|\, \sigma_i^z\, |0\rangle|^2$ is the imaginary-time auto-correlation function with $\sigma_i^z(\tau) = e^{\tau\mathcal{H}}\sigma_i^z e^{-\tau\mathcal{H}}$ being the time evolution of σ_i^z, and $\{|m\rangle\}$ refer to eigenstates with excitation energy ε_m relative to the ground state $|0\rangle$. Using the distribution of low-energy excitations given in (1.8), we then obtain a singular behavior for the disorder average of the local static susceptibility

$$[\chi^{\rm loc}(\omega = 0)]_{\rm av} \sim \int_T^\infty d\varepsilon \frac{\rho(\varepsilon)}{\varepsilon} \sim T^{-1+d/z}\ , \tag{1.10}$$

which diverges for $T \to 0$ if $z > d$ [55]. This certainly happens for $d = 1$ [37, 49, 88, 103, 50].

In higher dimensions, effects of Griffiths-McCoy singularities are expected to survive. Senthil and Sachdev analytically studied the transverse-field Ising model in higher dimensions on a percolating lattice, and found Griffiths-McCoy singularities on either side of the transition [59]. Such anomalous singularities in higher dimensions have also been confirmed numerically [55, 42, 91, 92].

1.4.2 Activated dynamic scaling

The random transverse-field Ising ferromagnetic chain was studied in great detail by Fisher [37, 49] using a strong-disorder renormalization group analysis (Ma). In addition to the Griffiths-McCoy singularities described in the previous section, Fisher pointed out that the critical behavior is controlled by an *infinite-randomness fixed point* [98], which means that the system appears more and more random on lower and lower energy scales. As a result, many physical quantities have very broad distributions, with significant difference between average and typical values, and the former are dominated by rare events. In addition, instead of a power-law relation between a characteristic the time scale and the length scale, $\xi_\tau \sim \xi^z$, at the critical point, one has an exponential relation $\xi_\tau \sim \exp(\text{const. } \xi^\psi)$ with $\psi < 1$, implying an infinite dynamical exponent $z \to \infty$. This is called *activated dynamical scaling,* and is due to the broad distribution of relaxation times. An equivalent behavior is that at the critical point energies (frequencies) scale as $\varepsilon \sim \exp(-\text{const. } \xi^\psi)$.

It is now known that ground states of a few one-dimensional quantum system, apart from the random transverse-field Ising chain, are governed by the infinite-randomness fixed point; examples include the random singlet states of the spin-1/2 antiferromagnetic chain [41] and quantum critical points separating random singlet states and the gapless Haldane phase in the spin-1 Heisenberg chains [69, 75]. Fisher also pointed out that frustration is irrelevant in the infinite-randomness limit, thus the spin-glass quantum critical points should be governed by the same infinite-randomness fixed point as the random ferromagnetic critical points [41].

An example for activated dynamical scaling in higher dimensions is the quantum bond-diluted Ising model in a transverse field defined by the Hamiltonian (1.6) with $h_i = h$ and the following probability distribution of the interactions:

$$J_{ij} = \begin{cases} 0 & \text{with probability } p \,, \\ J & \text{with probability } 1-p \,, \end{cases} \tag{1.11}$$

which is presented by Senthil and Sachdev [59]. At low dilution, $p \to 0$, there is a zero temperature ferromagnet-paramagnet transition turned by transverse field, as mentioned in Sec. 1.3. When $h = 0$, there is a percolation transition at $p = p_c$. At this percolation threshold $p = p_c$, the system remains critical for a finite range transverse field $h < h_M$ [15]. In [59], the relation between a characteristic energy scale ε and a characteristic length scale ξ at the critical line $p = p_c$, $h < h_M$ was found to be exponential: $\varepsilon \sim (-\text{const.}\, \xi^{d_f})$, where d_f is the fractal dimension of the percolating clusters, indicating activated dynamical scaling.

The scaling scenario for an infinite-randomness fixed point in the random transverse Ising ferromagnet in two dimensions have been confirmed by recent Monte Carlo simulations [91] and numerical renormalization-group studies [105, 109]. The same qualitative behavior has also been numerically found in three dimensions [105]. Activated scaling in

the two-dimensional diluted Ising model introduced by Senthil et al. [59] was also numerically proved by a recent quantum Monte Carlo simulations [92, 116]. However, the quantum Monte Carlo studies of the spin glass in two and three dimensions concluded the conventional scaling near the critical point, implying a finite-randomness fixed point [42, 43]. The critical properties of higher dimensional XX and Heisenberg antiferromagnets are believed to be controlled by finite-randomness fixed points [105, 106] in contrast to the one-dimensional case.

1.5 Exact results of the random transverse-field Ising ferromagnetic chain

The random transverse-filed Ising chain can be solved analytically. The ground state of this model is related to the finite-temperature behavior of a two-dimensional classical Ising model with disorder perfectly correlated along one direction, which was studied by McCoy and Wu [6, 7, 8]. The McCoy-Wu model consists of a nearest neighbor Ising model on a two-dimensional lattice, on which all the vertical couplings K take the same value, while the horizonal bonds J_{ij} are differ from column to column. This is essentially equivalent to the random transverse-filed Ising chain with nonrandom transverse-fields $h_i = h$ and random bonds J_{ij} drawn independently from a distribution $\rho(J)$ (s. Chapter 2). This model was later generalize to random h_i's by Shankar and Murphy and solved by the transfer matrix approach [27]. From a strong-disorder renormalization group analysis [20, 21], Fisher worked out many properties of the quantum system at criticality and in the vicinity of the transition in greatest detail [37, 49]. This study was generalized to non-critical region far away from the critical point by Iglói et al. [115, 126]. Another theoretical tool to analyze this model is mapping to a random walk problem. Iglói et al. used this method to extend the investigations [84] into surface properties. Here we briefly summarize the conclusions and the exact results of these analytical studies in order to give an overview of our discussions in the following chapters.

The self-dual nature of the random transverse-Ising chain suggests that the system will be at criticality if the distributions of bonds and fields are identical. Following Fisher [49], we define the quantum control parameter of the model as

$$\delta = \frac{[\ln h]_{\rm av} - [\ln J]_{\rm av}}{\mathrm{var}(\ln h) + \mathrm{var}(\ln J)} \ , \tag{1.12}$$

where $[\cdots]_{\rm av}$ denotes an average over disorder and $\mathrm{var}(\cdots)$ is the variance. The parameter δ that represents the deviation from the critical point, $\delta = 0$, is chosen so that the quantum disordered phase corresponds to $\delta > 0$, and the quantum ordered phase corresponds to $\delta < 0$.

At the critical point $\delta = 0$, the dynamical exponent z is infinite. The relationship between a characteristic energy scale ε and a length scale L is exponential, given by [37, 49]

$$\varepsilon(\delta = 0) \sim \exp(-\text{const.} \times L^{\psi}) \tag{1.13}$$

with

$$\psi = \frac{1}{2}, \tag{1.14}$$

instead of the conventional power-law relationship, $\varepsilon \sim L^{-z}$. This is called activated dynamical scaling. Away from criticality, the generalized dynamical exponent $z(\delta)$, defined by $\varepsilon(\delta \neq 0) \sim L^{-z(\delta)}$, is finite and has an exact relation with the quantum control parameter δ via [88]

$$\left[\left(\frac{J^2}{h^2}\right)^{1/z}\right]_{\text{av}} = 1 \ . \tag{1.15}$$

The strength of all singularities occurring in the Griffiths-McCoy phase can be parameterized by $z(\delta)$, e.g., for the local susceptibility $\chi_{\text{loc}} \sim T^{-1+1/z(\delta)}$, for the imaginary time autocorrelations $G_{\text{loc}} = [\langle \sigma_i^z(\tau)\sigma_i^z(0)\rangle]_{\text{av}} \sim \tau^{-1/z}$, for the specific heat $C \sim T^{1/z(\delta)}$ and for the magnetization in a longitudinal field (in the z direction) $M \sim H^{1/z}$.

In the context of the renormalization-group, which we will discuss more in Chapter 4, the energy scale ε mentioned above at criticality, as well as in the Griffiths-McCoy phase, can be regarded as the energy gaps of strongly coupled spin clusters, and the length scale L the average spacing between the clusters. In addition, the magnetic moment of the strongly coupled clusters, μ, scales as

$$\mu \sim (\ln \varepsilon)^{-\phi} \tag{1.16}$$

with

$$\phi = \frac{\sqrt{5}+1}{2} \approx 1.62 \tag{1.17}$$

at the critical point, defining a new exponent ϕ [37, 49].

As mentioned in the previous section, the behavior of infinite randomness at low-energy scale also results in broad distribution of some physical quantities [37, 49]; e.g. the spin correlation function $C_{ij} \equiv \left\langle \sigma_i^z \sigma_j^z \right\rangle$. As a result of the large fluctuations, the average and typical correlations behave quite differently: at criticality, the average correlation function $C_{\text{av}} \equiv [C_{ij}]_{\text{av}}$, which is dominated by rare pairs of spins having a correlation of order one, decays with a power of the distance $|i-j|$ as

$$C_{\text{av}}(\delta = 0) \sim |i-j|^{-\eta} \tag{1.18}$$

with

$$\eta = 2(1 - \phi\psi) = \frac{3-\sqrt{5}}{2} \approx 0.38 \ , \tag{1.19}$$

whereas the typical correlation function falls off as a stretched exponential [27, 37, 49]

$$C_{\rm typ}(\delta=0) \equiv \exp[\ln C_{ij}]_{\rm av} \sim \exp(-\text{const.} \times |i-j|^{\psi}) \; . \tag{1.20}$$

In the quantum disordered phase near the critical point, the average correlation function decays exponentially for long distances

$$C_{\rm av}(\delta>0) \sim \exp(-|i-j|/\xi) \; , \tag{1.21}$$

giving the true correlation length ξ where

$$\xi \sim |\delta|^{-\nu} \tag{1.22}$$

with

$$\nu = 2 \, . \tag{1.23}$$

The typical correlations fall off as a more rapid exponential

$$C_{\rm typ}(\delta>0) \sim \exp(-|i-j|/\xi_{\rm typ}) \; , \tag{1.24}$$

defining the typical correlation length given by [27, 37, 49]

$$\xi_{\rm typ} \sim |\delta|^{-\nu_{\rm typ}} \tag{1.25}$$

with

$$\nu_{\rm typ} = \nu(1-\psi) = 1 \, . \tag{1.26}$$

From the above-mentioned results, we can see that we have three basic critical exponents ψ, ϕ and ν defined in (1.13), (1.16) and (1.22), from which the other critical exponents can be obtained [98]. Indeed, these three exponents can express all bulk critical exponents, including the scaling dimension of the average bulk magnetization, x_m, given exactly by

$$x_m = \beta_b/\nu = 1 - \phi\psi \approx 0.19 \; , \tag{1.27}$$

which describes the average bulk magnetization of the model with size L via

$$[m(\delta=0)]_{\rm av} \equiv [\mu/L]_{\rm av} \sim L^{-x_m} \tag{1.28}$$

at criticality, and

$$[m(\delta)]_{\rm av} \sim |\delta|^{\beta_b} \sim |\delta|^{x_m \nu} \tag{1.29}$$

in the ordered phase with a small $|\delta|$ in the thermodynamic limit.

In addition to the bulk exponents, the critical exponents associated with the surface (end-point) magnetization $m_s = \langle \sigma_1^z \rangle$ can also be exactly calculated [6, 7, 8, 49, 84, 87]. At the critical point, the average surface magnetization scales as

$$[m_s(\delta=0)]_{\rm av} \sim L^{-x_m^s} \tag{1.30}$$

with the scaling dimension

$$x_m^s = \frac{1}{2}\,. \tag{1.31}$$

Thus, the scaling behavior of the end-to-end correlation for a critical chain of length L is given by

$$C_{1L} \equiv [\langle \sigma_1^z \sigma_L^z \rangle]_{\rm av} \sim L^{-2x_m^s}\ . \tag{1.32}$$

In the quantum ordered phase near the critical point, the average surface magnetization asymptotically vanished as

$$[m_s(\delta < 0)]_{\rm av} \sim (-\delta)^{\beta_s} \tag{1.33}$$

with

$$\beta_s = 1, \tag{1.34}$$

which satisfies the scaling relation

$$x_m^s = \beta_s/\nu\ . \tag{1.35}$$

With these detailed analytical results, the critical and off-critical properties of the transverse-field Ising chain with quenched disorder seem clear. In the renormalization-group language, this type of critical behavior is controlled by an infinite-randomness fixed point. However, we should note that for some types of disorder distributions, the critical exponents may become non-universal, suggesting the presence of a line of infinite-randomness fixed points. One of such disorder distributions is strongly broad disorder, which we will discuss in Chapter 6.

Chapter 2

Continuous-Time Cluster Algorithm for Quantum Monte Carlo Simulations

Monte Carlo (MC) simulation is a powerful tool for studying thermodynamic properties of many-body systems. Different schemes have been developed to extend the MC method into quantum statistical mechanics. The mapping to a classical model based on path integral formulation of quantum systems, which we discussed in Chapter 1, is one of techniques. In this chapter we describe a new quantum MC method based on cluster updates in continuous time, which was introduced by Rieger and Kawashima [99, 101]. We will focus on the transverse Ising model defined by

$$\mathcal{H} = -\sum_{<i,j>} J_{ij}\sigma_i^z\sigma_j^z - \sum_i h_i\sigma^x \ , \tag{2.1}$$

here the $\{\sigma_i^\alpha\}$ are Pauli matrices, and the indices i and j run over the sites of a d-dimensional lattice with side length L. The nearest neighbor ferromagnetic interactions J_{ij} and transverse field h_i are either uniform ($J_{ij} = J$, $h_i = h$) or random. In this chapter we always assume periodic boundary conditions.

2.1 Quantum-classical mapping of the transverse Ising model

As mentioned previously, using the Feynman path-integral approach, we can map the quantum Hamiltonian described by (2.1) onto a classical Hamiltonian for the Ising model with an additional temporal dimension of size β. In this section we briefly outline the derivation [17, 65]. We first divide the time interval $[0,\ \beta]$ over which the system evolves into many infinitesimal subintervals $\delta\tau$ for which the density matrix can be calculated. Formally we write the density operator, or the time-evolution operator in the context of path-integral, as $e^{-\beta\mathcal{H}} = [e^{-\delta\tau\mathcal{H}}]^{L_\tau}$ with $L_\tau\delta\tau = \beta$ for a large integer L_τ. The Hamiltonian in (2.1) is

consisted of two parts that do not commute: $\mathcal{H}_1 = -\sum J_{ij}\sigma_i^x\sigma_j^x$ and $\mathcal{H}_2 = -\sum h_i\sigma_i^z$. Using the fact that

$$e^{-\delta\tau\mathcal{H}_1}e^{-\delta\tau\mathcal{H}_2} = e^{-\delta\tau(\mathcal{H}_1+\mathcal{H}_2)}(1+\mathcal{O}(\delta\tau^2\,|[\mathcal{H}_1,\mathcal{H}_2]|))\ , \tag{2.2}$$

we can neglect the commutator between $\mathcal{H}_1$ and $\mathcal{H}_2$ in the limit $\delta\tau \to 0$ and make the approximation

$$e^{-\delta\tau\mathcal{H}} \approx e^{-\delta\tau\mathcal{H}_1}e^{-\delta\tau\mathcal{H}_2}. \tag{2.3}$$

This approximation in the limit of large L_τ has been proved mathematically rigorous by Trotter [4] and, is referred to as the Trotter formula

$$e^{-\beta(\mathcal{H}_1+\mathcal{H}_2)} = \lim_{L_\tau\to\infty}[e^{-(\beta/L_\tau)\mathcal{H}_1}e^{-(\beta/L_\tau)\mathcal{H}_2}]^{L_\tau}. \tag{2.4}$$

We employ this approximation and then insert a complete set of intermediate states defined as $|\{S(\tau)\}\rangle \equiv |S_1(\tau), S_2(\tau), \cdots, S_N(\tau)\rangle$, where $|S_i(\tau)\rangle$ is the eigenstate of the spin operator σ_i^z at time τ, into the expression for the partition function $Z = \mathrm{Tr}e^{-\beta\mathcal{H}}$. This yields

$$Z = \lim_{\delta\tau\to 0}\mathrm{Tr}\prod_\tau e^{\delta\tau\sum_{\langle ij\rangle}J_{ij}S_i(\tau)S_j(\tau)}\,\langle S(\tau)|\,e^{\delta\tau\sum_i h_i\sigma_i^x}\,|S(\tau+\delta\tau)\rangle\ , \tag{2.5}$$

where $S_i = \pm 1$ are eigenvalues of σ_i^z and $\tau = 1, 2, \cdots, L_\tau$ labels the time slices. Here we impose periodic boundary conditions in the imaginary time direction. Using the operator identity

$$e^{a\sigma^x} = \cosh a + \sigma^x \sinh a\ , \tag{2.6}$$

and the fact that $\sigma_i^x\,|S_i\rangle = |-S_i\rangle$, one can evaluate the transfer matrix

$$\langle S_i(\tau)|\,e^{\delta\tau h_i\sigma_i^x}\,|S_i(\tau+\delta\tau)\rangle = e\left[\frac{1}{2}\sinh 2\delta\tau h_i\right]^{\frac{1}{2}}e^{-(\frac{1}{2}\tanh\delta\tau h_i)S_i(\tau)S_i(\tau+\delta\tau)}\ , \tag{2.7}$$

which leaves

$$Z = \lim_{\delta\tau\to 0}C_{\delta\tau}\sum_{\{S_i(\tau)\}}e^{-\mathcal{S}_{\mathrm{cl}}} \tag{2.8}$$

with $C_{\delta\tau} = \prod_i\prod_\tau\left[\frac{1}{2}\sinh(2(\delta\tau)h_i)\right]^{\frac{1}{2}}$ and an effective classical action, $\mathcal{S}_{\mathrm{cl}}$, given by

$$\mathcal{S}_{\mathrm{cl}} \equiv \beta_{\mathrm{cl}}\mathcal{H}_{\mathrm{cl}} = -\sum_{<ij>,\tau}K_{ij}S_i(\tau)S_j(\tau) - \sum_{i,\tau}K_i'S_i(\tau)S_i(\tau+\delta\tau)\ , \tag{2.9}$$

where

$$K_{ij} = \delta\tau J_{ij} \tag{2.10}$$

and

$$K_i' = -\frac{1}{2}\ln\tanh\delta\tau h_i \tag{2.11}$$

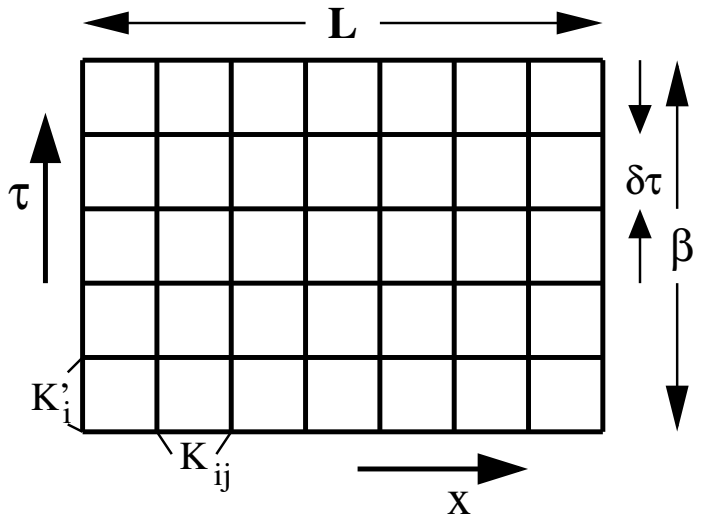

Figure 2.1: The equivalent classical model of a d-dimensional quantum transverse-field Ising model is an anisotropic $(d+1)$-dimensional Ising model with an added imaginary time dimension of length β, which corresponds to the inverse temperature of the quantum system. This mapping is exact only in the limit $\delta\tau \to 0$, i.e. the number of imaginary time slices $L_\tau \to \infty$. In this limit, the couplings between two spins in the time direction K_i' diverges, while the couplings in the space K_{ij} dimension goes to zero.

play the role of interactions between the adjacent classical Ising spins $S_i(\tau) = \pm 1$ in the spatial and temporal dimension respectively on a $(d+1)$-dimensional lattice of size $N = L^d \times L_\tau$ (Fig. 2.1). The temperature $T = \beta^{-1}$ of the quantum system is not the same as the effective temperature $\beta_{\rm cl}^{-1}$ of the corresponding classical model. Instead β represents the size of the imaginary time dimension, and is set to zero by taking $L_\tau \to \infty$.

Note the corresponding classical model is very anisotropic: In the limit $\delta\tau \to 0$, the strength of interaction in the temporal direction, K_i', diverges logarithmically whereas the strength in spatial direction, K_{ij}, goes to zero. For a pure system, such anisotropy does not alter the critical behavior [66]. In fact, the dynamical exponent z is equal to one, thus space and time are equivalent in pure systems. For a random model, J_{ij}'s only depend on the d spatial coordinates, so we have a $(d+1)$-dimensional Ising model with perfectly correlated disorder along the time direction, which is closely related to the anisotropic McCoy-Wu model [6, 7, 8]. This anisotropy leads to $z \neq 1$. The analysis of numerical data then has to be done using anisotropic finite-size scaling [32, 42, 43, 91].

2.2 The continuous-imaginary-time cluster algorithm

2.2.1 Motivation

The quantum-classical mapping discussed in Sec. 2.1 makes it possible to study the quantum phase transitions in the transverse Ising model by classical Monte Carlo simulations. Before performing the Monte Carlo simulation, we should note some drawbacks of using conventional simulation methods.

It is well known that the simulation algorithms employing local update procedures, e.g. the Metropolis method, suffer from "critical slowing down" near a continuous phase transition. This means the algorithm exhibits a long autocorrelation time between measurements of physical quantities near the transition and becomes inefficient. A possible way to overcome this difficulty is to employ large-scale updates, which decorrelate a configuration much quickly. The Swendsen-Wang (SW) cluster algorithm [28] and the Wolff single cluster algorithm [33] are examples for such nonlocal update method for reducing critical slowing down. In recently years, several types of cluster algorithms, e.g. loop algorithms, have been developed for various purposes [38, 47].

Most quantum Monte Carlo simulations are done on a lattice with discrete imaginary time. i.e. on a $L^d \times L_\tau$ lattice having Ising spin on each site. One expects the critical behavior is independent of the time spacing $\delta\tau$ and takes e.g. $\delta\tau = 1$ for convenience [42, 43, 91]. However, this artificial time discretization will cause systematic error of order $(\delta\tau)^2$ due to (2.2). To eliminate this systematic error, we should take $\delta\tau = 0$ and work with continuous time. Recently, such continuous time algorithms have been discussed and applied to quantum Monte Carlo simulations in the pioneer work by Beard et al. [60] and Proko'ef et al [61].

A new Monte Carlo method was presented by Rieger and Kawashima, which combines the SW cluster update algorithm and the continuous time algorithm [99, 101]. Both two problems mentioned above can be overcome in this method.

2.2.2 Description of the algorithm

The SW cluster algorithm was invented by Swendsen and Wang for the case of the Potts model [28], and has been generalized for other systems. The discrete-time SW cluster-building rule for our anisotropic Ising model is straightforward (Fig. 2.2(a)): Following Swendsen and Wang, bonds between nearest-neighbor sites i and j with the same spin value are assigned with the probability $p_{ij} = 1 - e^{-2K_{ij}} = 2\delta\tau J_{ij} + \mathcal{O}(\delta\tau^2)$, which is designed to satisfy detailed balance. The same rule is used for connecting neighbor sites τ and $\tau + 1$ in the time direction. The connection probability in the time direction at a particular site i of space is then $p'_i = 1 - e^{-2K'_i} = 1 - \delta\tau h_i + \mathcal{O}(\delta\tau^2)$. No bonds are

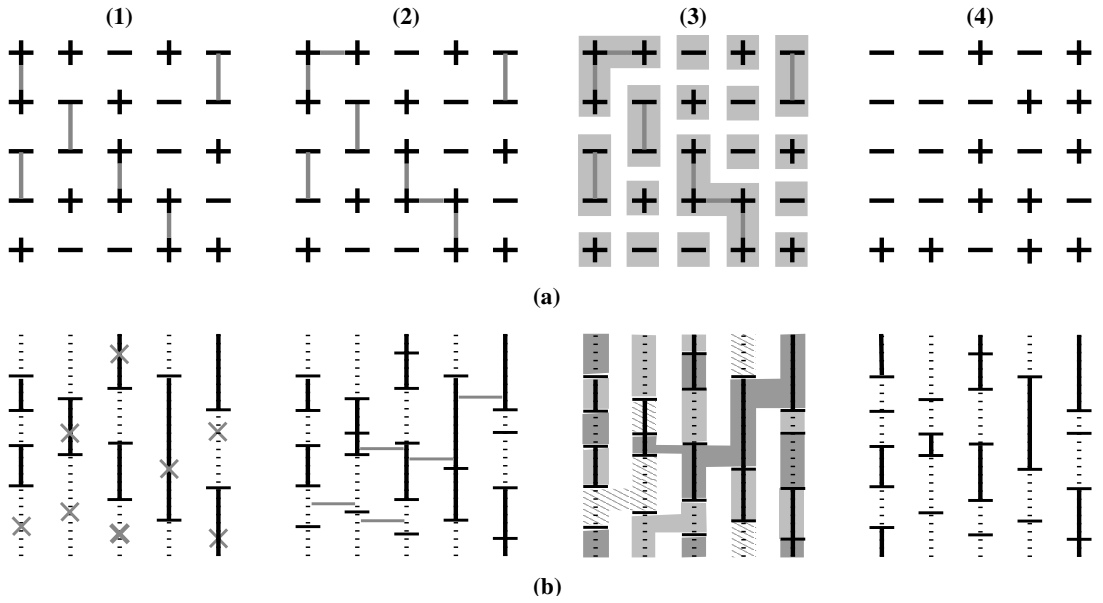

Figure 2.2: **(a):** Schematic view of the Swendsen-Wang cluster algorithm for a discrete-time model: (1) connect spins along the time direction; (2) connect spins along the space direction; (3) form clusters; (4) flip spins after assigning spin value to each cluster. **(b):** The continuous-time cluster algorithm (full/broken lines correspond to segments with spin up/down): (1) insert new cuts along time direction according to a Poisson process; (2) connect segments with probabilities given in (2.15); (3) form clusters of segments; (4) change spin values of segments after assigning randomly spin values to each cluster; remove the redundant cuts within a segment before starting a new cycle.

included between sites with different spin states. This gives a configuration of bonds that form clusters of spins, with all spins in each cluster having the same value.

To take this algorithm to the continuous-time limit $\delta\tau \to 0$, we first construct *segments* formed by spins with the same value along the imaginary time direction. In this continuum limit, one spin is no more sited on a lattice point, but evolves over a time interval of length t, corresponding to a segment of length t. The ends of such segments are called *cuts* in the following, and are determined by the points of time at which this spin changes its value. We use $I_i([t_1, t_2])$ to denote a segment located at site i of space with two cuts at t_1 and t_2 in the imaginary-time axis. The SW cluster rule in the imaginary time direction enables this construction of segments: the probability for setting $t/\delta\tau$ successive bonds between spins along the time direction at a particular site i is given by

$$p_i'(t) \equiv p_i'^{t/\delta\tau} = (1 - \delta\tau h_i)^{t/\delta\tau} \ . \tag{2.12}$$

In the limit $\delta\tau \to 0$, this is the probability for a segment of length t, and we obtain

$$p_i'(t) \underset{\delta\tau\to 0}{\longrightarrow} e^{-h_i t} \ . \tag{2.13}$$

Thus generating cuts is a Poisson process with decay time h_i^{-1} along the imaginary time direction.

The next procedure is to connect the segments on neighboring sites. Supposing we have two neighboring segments on sites i and j , say $I_i([t_1, t_2])$ and $I_j([t_3, t_4])$, with the same spin state and a time-overlap $\tilde{t}$ (i.e. $\tilde{t}$ is the length of the time interval $[t_1, t_2] \cap [t_3, t_4]$), the probability $p_{ij}(\tilde{t})$ that the two segments are connected is the probability for connecting any pair of the lattice points in the time interval of length $\tilde{t}$ in the limit $\delta\tau \to 0$. Thus the probability for not connecting the two segments is given by

$$(1 - p_{ij})^{\tilde{t}/\delta\tau} = (1 - 2\delta\tau J_{ij})^{\tilde{t}/\delta\tau} \underset{\delta\tau\to 0}{\longrightarrow} e^{-2J_{ij}\tilde{t}} . \tag{2.14}$$

Hence

$$p_{ij}\left(\tilde{t}\right) = 1 - e^{-2J_{ij}\tilde{t}} . \tag{2.15}$$

Having connected all segments, we identify clusters of connected segments, and assign spin value $+1$ or -1 to each cluster with equal probability. All segments in a cluster then change their spin states collectively into the assigned value. The basic steps of this algorithm is shown in Fig. 2.2(b).

We close this subsection by pointing out some advantages of implementing the continuous-time cluster algorithm: (1) Critical slowing down is reduced by nonlocal moves; (2) The systematic error caused by time discretization is eliminated, therfore, the original quantum Hamiltonian can be represented exactly; (3) Efficient storage: The segments can be stored in a linked list with a capacity of order $\beta L^d h^{\max}$ during the implementation of the continuous-time algorithm, while in a discrete-time algorithm fixed arrays are needed to store spin values, the number of which is $\beta L^d/\delta\tau$ and diverges in the limit $\delta\tau \to 0$.

Chapter 3

Monte Carlo Simulations of the Transverse Ising Model

In this chapter we will present the results of our numerical study of the random transverse-field Ising model (2.1) by using the continuous-time cluster algorithm described in the previous chapter. We used periodic boundary conditions in both the space and imaginary time directions, and turned through the transition by varying the transverse field. Since the effective classical model, i.e. the Ising model, for the pure quantum system in one and two dimensions had been intensively studied, and there are extensive analytical and numerical results for the critical properties available, we used these pure systems as a benchmark to test reliability of our code. For quenched random systems, we used the following rectangular distribution:

$$\pi(J) = \begin{cases} 1, & \text{for } 0 < J < 1, \\ 0, & \text{otherwise,} \end{cases}$$

$$\rho(h) = \begin{cases} h_0^{-1}, & \text{for } 0 < h < h_0, \\ 0, & \text{otherwise.} \end{cases} \tag{3.1}$$

The transition is therefore turned through by varying a single parameter h_0. Before presenting the results, we will discuss how to obtain critical exponents by using finite size scaling on an anisotropic system that we have to deal with.

3.1 Measurements and anisotropic finite size scaling

In our numerical calculations by using the continuous-time cluster algorithm, the imaginary time has become a continuous variable. The measurement of observables in this continuous

time version is straightforward: for example, the local magnetization m_i at site i is given by

$$m_i = \beta^{-1} \int_0^\beta d\tau \, \langle S_i(\tau) \rangle \ , \tag{3.2}$$

where $\langle \cdots \rangle$ denotes the Monte Carlo average for a single sample. This quantity can be obtained from the difference between the total length of all segments with spin states $+1$ and those with spin states -1, divided by β; From m_i, we can calculate the local static susceptibility given by

$$\chi_i^{\rm loc} = \int_0^\beta d\tau \, \langle \sigma_i^z(\tau) \sigma_i^z(0) \rangle = \beta \left\langle m_i^2 \right\rangle \ ; \tag{3.3}$$

A further quantity of interest is the correlation function in the space directions. The correlation function of a distance r along one space direction is given by

$$C_i(r) = \beta^{-1} \int_0^\beta d\tau \, \langle S_i(\tau) S_{i+r}(\tau) \rangle \ , \tag{3.4}$$

i.e. one adds or subtracts the overlapping length of all segments at sites i and $i + r$ depending on whether the overlapping parts of the segments are in the same or opposite spin states.

The thermodynamic limit of the quantum model corresponds to the spatial dimensions L of the effective classical model going to infinity, while the zero temperature limit of the quantum system corresponds to the limit of the imaginary time dimension β going to infinity. To extrapolate to the thermodynamic limit and the $T \to 0$ limit of the quantum system, we then have to use finite size scaling techniques for an anisotropic system. Unlike isotropic models where the scaling is done equally for all dimensions, the correlation lengths in the space and imaginary-time directions in our anisotropic model may diverge with different exponents:

$$\xi \sim |\delta|^{-\nu} \tag{3.5}$$

$$\xi_\tau \sim |\delta|^{-\nu_\tau} \tag{3.6}$$

where $|\delta|$ is the distance from the critical point. The ratio $z = \nu_\tau / \nu$ of these exponents is the dynamic exponent [32]. Under these circumstances, a thermodynamic quantity O is expected to have the finite size scaling form:

$$[O]_{\rm av} = L^{-x_O} \widetilde{O} \left(\frac{L}{\xi}, \frac{\beta}{\xi_\tau} \right) \ . \tag{3.7}$$

where $[\cdots]_{\rm av}$ denotes an average over disorder, $\widetilde{O}$ is a scaling function of two independent scaling variables, and x_O is the scaling dimension of the quantity O. For example, for the

magnetization per site, $m = (N\beta)^{-1} \sum_{i=1}^{N} \int_0^\beta d\tau \, \langle S_i(\tau) \rangle$ (where $N = L^d$ is the number of the sites), one expects

$$[m]_{\rm av} = L^{-\beta_b/\nu} \widetilde{m} \left(\frac{L}{\xi}, \frac{\beta}{\xi_\tau} \right) \ , \tag{3.8}$$

defining $x_m = \beta_b/\nu$.

Assuming that the dynamical scaling relating the time and space correlation lengths is conventional near the critical point: $\xi_\tau \sim \xi^z$ with a finite z, the scaling form (3.7) can be written as

$$[O]_{\rm av} = L^{-x_O} \widetilde{O} \left(\delta L^{1/\nu}, \beta/L^z \right) \ . \tag{3.9}$$

For activated dynamical scaling, the dynamical exponent z is infinite and the logarithm of the correlation time ξ_τ scales with a power of the correlation length: $\ln \xi_\tau \sim \xi^\psi$. This suggests that the second scaling variable should be $\ln \beta/L^\psi$, thus

$$[O]_{\rm av} = L^{-x_O} \widetilde{O} \left(\delta L^{1/\nu}, \ln \beta/L^\psi \right) \ . \tag{3.10}$$

Following [42, 43, 91], we computed a dimensionless quantities, such as the Binder cumulant [22], with fewer adjustable parameters for a scaling fit to estimate the critical point and the critical exponents. The disorder averaged Binder cumulant is given by

$$g \equiv \frac{1}{2} \left[3 - \frac{\langle m^4 \rangle}{\langle m^2 \rangle^2} \right]_{\rm av} \ . \tag{3.11}$$

In the thermodynamic limit $L \to \infty$, g has the property [42, 43, 93] that it tends towards zero in the disordered phase since the distributions of m tend towards a Gaussian form centered around $m = 0$, and tends to 1 in the ordered phase since the distributions tend to delta functions with peaks at $+1$ and -1. For finite sizes, the dimensionless quantity g obeys the finite-size scaling form (3.9) or (3.10) with $x_g = 0$. If we fix L and the maximal strength of the transverse field h_0, which serves as the control parameter triggering the phase transition, we find g has a maximum at some value of β, and tends to zero for $\beta \to 0$ as well as for $\beta \to \infty$. This can be explained as follows [42, 43, 93]: For small β, instead of a $(d+1)$-dimensional system we have effectively a classical d-dimensional system which is in its disordered phase since the critical point of the d-dimensional system is expected to be lower than that of $(d+1)$-system, thus $g \to 0$ in the limit $\beta/L \to 0$ as argued above; On the other hand, in the limit $\beta/L \to \infty$, the system is effectively a one-dimensional chain with infinite length along the imaginary time direction, which is also in the disordered phase since the correlation length is finite, so g tends to zero. Furthermore, the maximum of g increases with increasing L in the ordered phase and increases with increasing L in the disordered phase. At the critical point h_c, this maximum should be independent of size L since the first argument of the scaling function of g vanishes, and g depends only on the scaled shape β/L^z for conventional oder $\ln \beta/L^\psi$ for activated scaling.

The properties of the Binder cumulant described above provide us an efficiency method to locate the critical point h_c and determine the dynamical exponent z, which might be infinite at the critical point.

3.2 Pure systems in one and two dimensions

We tested our code first for the pure systems. The effective classical model of the one-dimensional pure quantum system ($d = 1$, $J_{ij} = 1$ and $h_i = h$) is the well-known two-dimensional Ising model [13]. The position of the critical point $h_0 = 1$ and the relation between time and space via $\xi_\tau \sim \xi$ with $z = 1$ can easily be checked by the variation of the Binder cumulant g with the inverse temperature β. Fig. 3.1 shows the data of g at the critical point $h_c = 1$, where the maxima are independent of the system size L, and its scaling plot with the scaling-variable β/L, yielding $z = 1$. With $z = 1$ and fixed aspect ratio β/L, the finite size scaling form given in (3.9) only involves the first argument $\delta L^{1/\nu}$, where $\delta = h - h_c$. We checked the finite size scaling of the cumulant, $g = \tilde{g}(\delta L^{1/\nu})$, and the magnetization $m = L^{-\beta_b/\nu}\tilde{m}(\delta L^{1/\nu})$, as shown in Fig. 3.2 and Fig. 3.3. The critical exponents $\nu = 1$ and $\beta_b = 1/8$ have been reproduced.

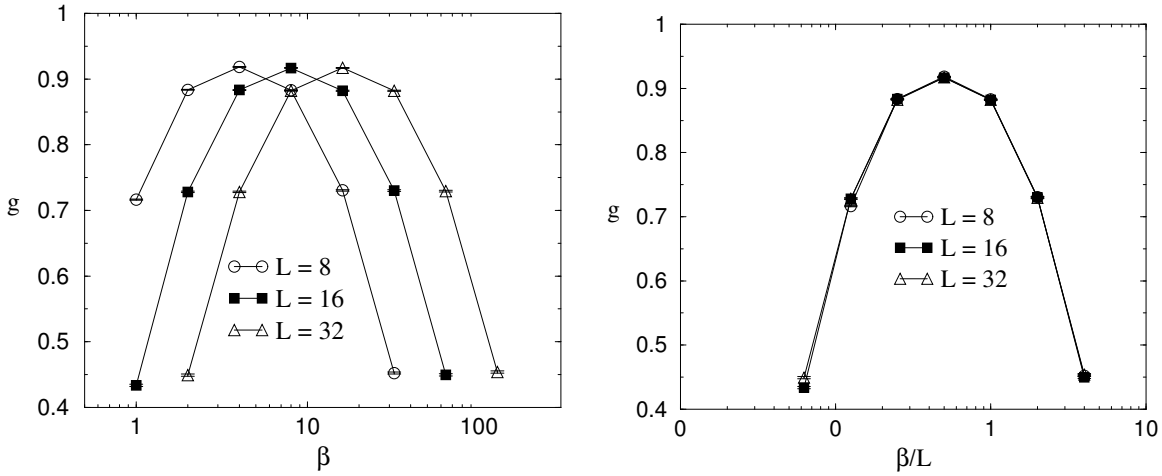

Figure 3.1: **Left:** Variation of the cumulant g with the length in the imaginary time direction β for various system sizes L for the $1d$ pure system. The maxima are independent of L, verifying $h_c = 1$. **Right:** Scaling of the data of g. The excellent collapse verifies that the dynamical exponent is unity.

As the first non-trivial application we considered the pure system in two dimensions with $J_{ij} = 1$ and $h_i = h$. The critical exponents associated with the ground state phase transition of this quantum system are the same as the exponents of the thermal phase transition in the equivalent classical 3-dimensional Ising model. First we located the critical point by varying the Binder cumulant g with the strength of field h for various system sizes L up to $L = 64$ with constant aspect ratio $\beta = 4L$ (here $z = 1$), at which g reaches its maximum. The position of intersection point shown in Fig. 3.4 gives $h_c = 3.044(2)$. From the finite size scaling for g and m we obtain the correlation length exponent $\nu = 0.624(3)$ and the scaling dimension of the magnetization $x_m = \beta_b/\nu = 0.505(1)$ (Fig. 3.5 and Fig. 3.6). Our estimates agree quite well with the series expansion results [12] and a resent numerical study by using the density matrix renormalization-group method [122].

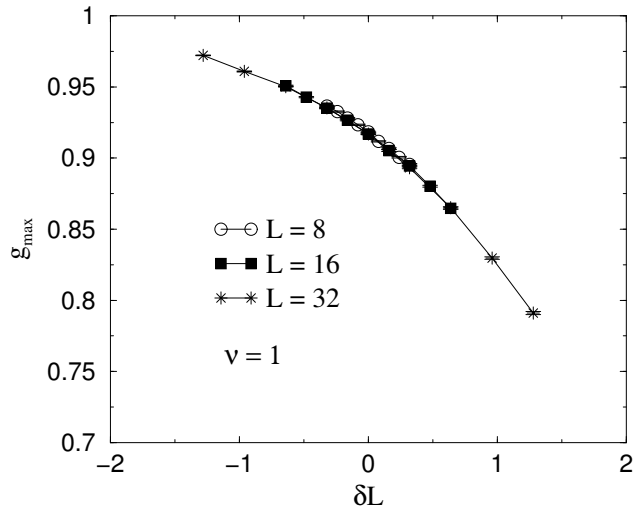

Figure 3.2: A scaling plot of g near the transition for the $1d$ pure system. Here the system sizes L and the inverse temperature β are chosen at the maximum of g, at which we have fixed aspect ratio $\beta/L = 1/2$. The fit gives $\nu = 1$

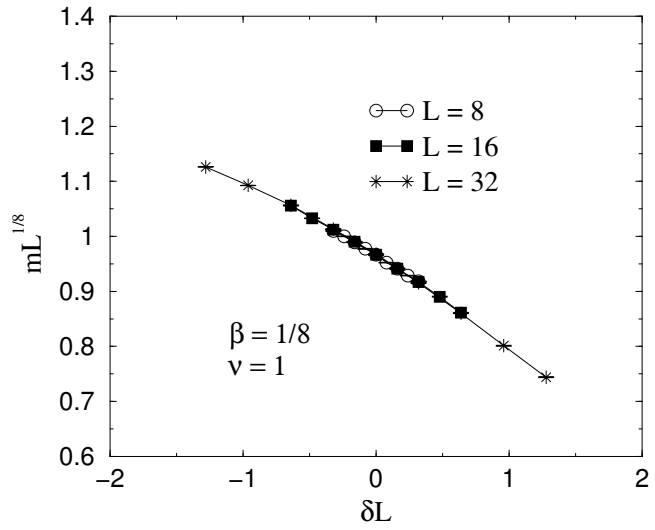

Figure 3.3: Finite-size scaling for the magnetization m of the $1d$ system. The fit is according to the exact values $\beta_b = 1/8$ and $\nu = 1$.

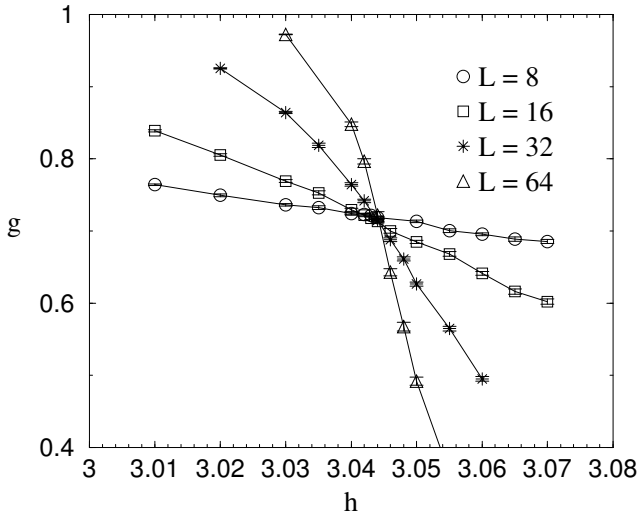

Figure 3.4: Variation of the dimensionless cumulant g with the quantum control parameter h for various system sizes with fixed aspect ratio $\beta = 4L$**.** We find the intersection at $h_c \approx 3.044$ for the $2d$ pure model.

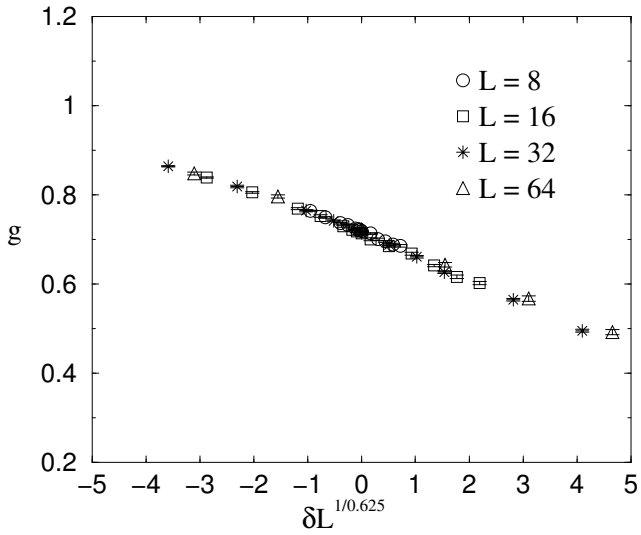

Figure 3.5: A scaling plot of the data in Fig. 3.5. From the best data collapse we estimate $\nu \approx 0.625$**.**

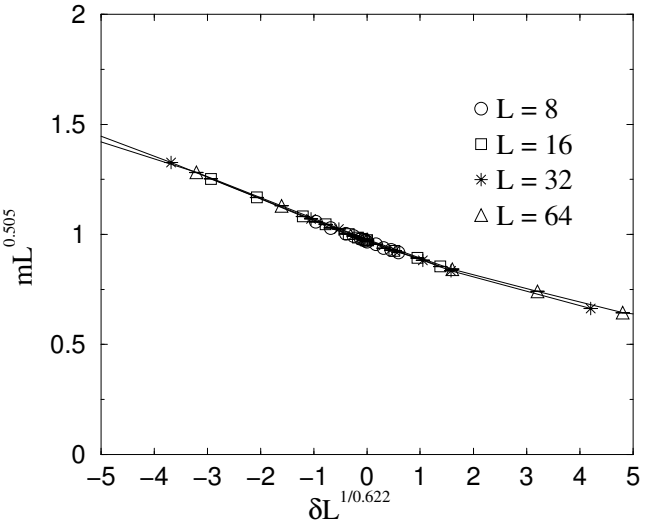

Figure 3.6: A finite-size scaling plot of the magnetization m for the $2d$ pure system with the scaling variables $mL^{\beta_b/\nu}$ and $\delta L^{1/\nu}$, yielding $\beta_b/\nu \approx 0.505$ and $\nu \approx 0.622$. The estimated correlation length exponent ν is quite near the result obtained from the scaling of g.

3.3 Random systems in one and two dimensions

3.3.1 The one-dimensional case

Now we turn to the random systems, which are the main objects in our studies. We start with one-dimensional case. The system is at its critical point when the field- and bond distributions are identical since the self-dual nature of the model. Following [49], we parameterize the deviation from criticality by

$$\delta = \frac{[\ln h]_{\rm av} - [\ln J]_{\rm av}}{\mathrm{var}(\ln h) + \mathrm{var}(\ln J)} \,. \tag{3.12}$$

For the distribution in (3.1), we have

$$\delta = \frac{1}{2} \ln h_0 \,. \tag{3.13}$$

We studied sizes up to $L = 64$ and took 2000 samples for each size and temperature. We found that no more 100 Monte Carlo sweeps were required for equilibration. After the sweeps for equilibration, we used 200-300 sweeps for measurements, which were performed every 5 sweeps. The simulations were performed mainly on Alpha-cluster and partially on Cray T3E.

First of all we discuss our results of the average Binder cumulant defined in (3.11). We computed g as a function of the inverse temperature β for system sizes ranged from 8 to

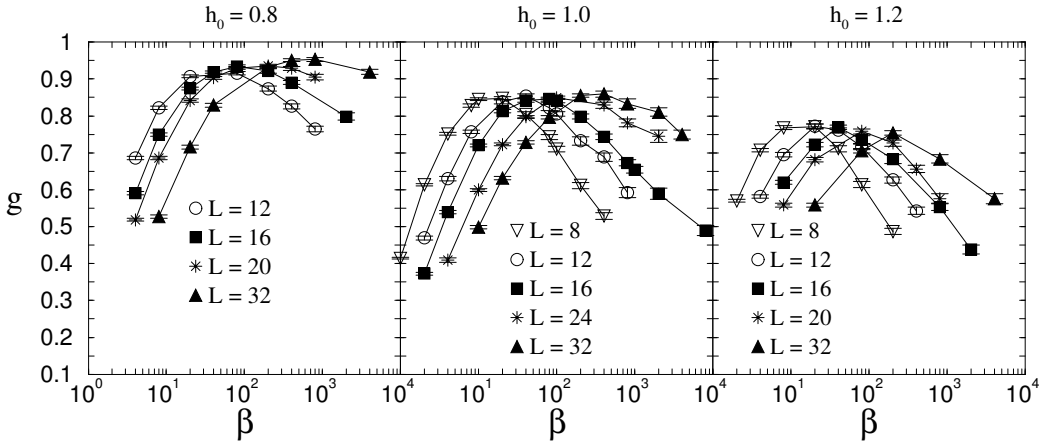

Figure 3.7: The average Binder cumulant g as a function of the inverse temperature β for three different control parameters h_0. The maximum value of g is independent of L for $h_0 = 1$, where the critical point is located. In the ordered phase, $h_0 < h_c$, the maximum increases with increasing L, while in the disordered phase, it decreases with L.

32 and various values of h_0. For such calculations, the inverse temperature, i.e. the size of the imaginary time dimension, was required up to 8000 for $L = 32$. As shown in Fig. 3.7, using the behavior of g vs β, one can readily locate the critical point h_c, since the peak height is independent of the system size L only at h_c. In our case, $h_c = 1$. Furthermore, we can confirm the behavior of activated dynamical scaling at the critical point $\delta = 0$ by using the scaling form

$$g(\delta = 0) = \tilde{g}(\ln \beta / L^{\psi}) \ , \tag{3.14}$$

instead of the conventional scaling form $g(\delta = 0) = \tilde{g}(\beta / L^{z})$. A corresponding scaling plot is shown in Fig. 3.8. The data collapse quite good with the prediction $\psi = 1/2$.

Next we consider the correlation function in the space direction. For each system size ranged from 12 to 64, we computed the correlation function

$$C(r) = \frac{2}{L} \sum_{i=1}^{L/2} C_i(r) = \frac{2}{L\beta} \sum_{i=1}^{L/2} \int_0^{\beta} d\tau \, \langle S_i(\tau) S_{i+r}(\tau) \rangle \tag{3.15}$$

for $r = 1 \ldots L/2$, and took β such that the Binder cumulant is closed to the peak. We are interested in the average correlations $C_{\rm av}(r) = [C(r)]_{\rm av}$ and the typical correlations $C_{\rm typ}(r)$. Here we define the typical correlation function to be the median. One could also define typical to be the exponential of the average of the log as in (1.20), this definition is, however, not suitable for Monte Carlo simulations where statistical errors could make the estimated value of a very small $C(r)$ go negative. Nevertheless, both definitions should have the same critical behavior.

One of the main features of the critical behavior controlled by an infinite-randomness fixed point is a very broad distribution of the correlation function. This leads to different behavior

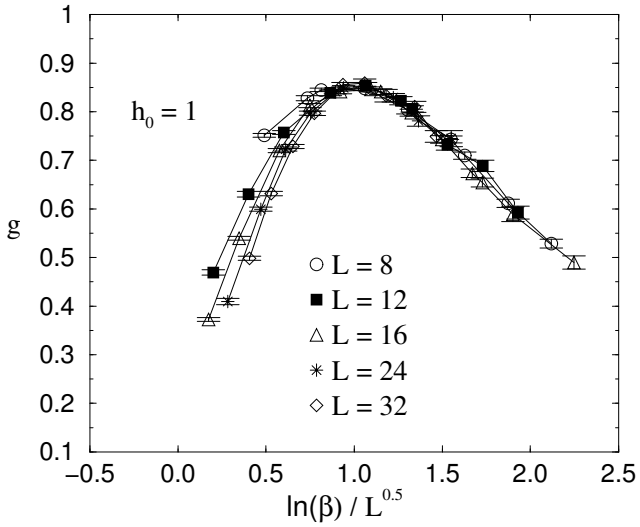

Figure 3.8: A scaling plot of g at the critical point $h_0 = 1$. The scaling variable is $\ln \beta / L^{0.5}$, yielding $\psi = 0.5$ and $z \to \infty$, as predicated by Fisher [37, 49]. Scaling works quite well for this range of sizes in the large β limit.

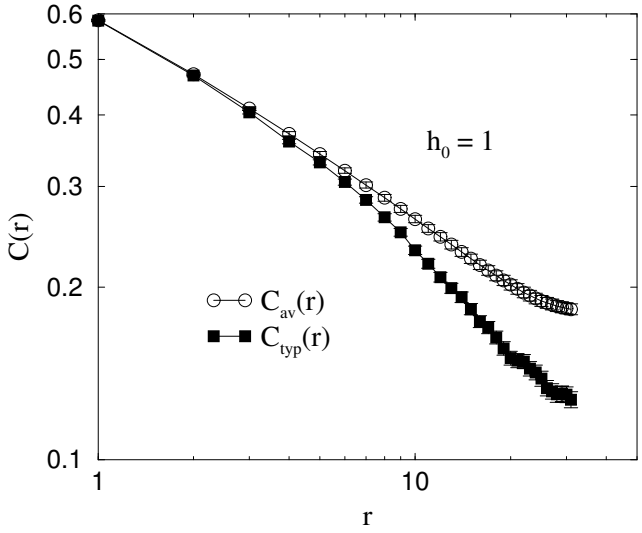

Figure 3.9: The average and typical correlations for spins separated by $r = 1 \ldots 32$ in a chain of size $L = 64$ at the critical point. As expected, the average decays with a power law (except for the part near $r = 32$ where the influence of periodic boundary conditions appears), while the typical value decays faster than a power because of the downward curvature in the range $r = 1 \ldots 20$.

of the average and typical correlations at the critical point, as shown in Fig. 3.9: the average decays as a power law, while the typical falls off faster than a power, as shown by the downward curvature. The date of the average correlation function for the larger sizes fall on

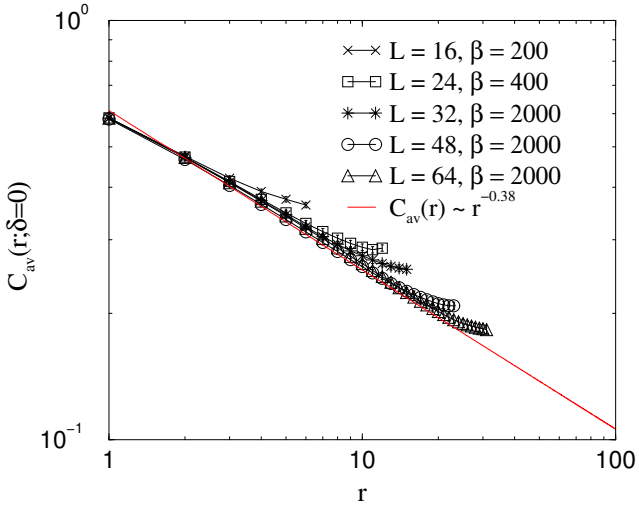

Figure 3.10: A log-log plot of the average correlation function against the spatial distance r at the critical point. The data for larger system sizes tend to the straight line, which has slope of -0.38, in agreement with the prediction in (1.19).

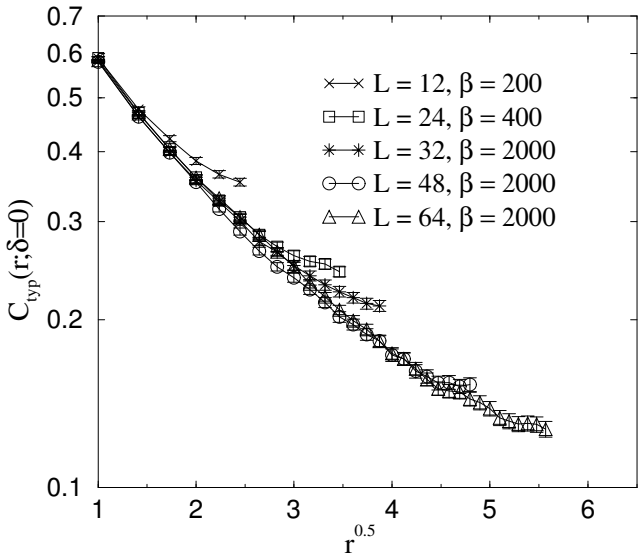

Figure 3.11: A plot of the typical correlation function for several system sizes against $r^{0.5}$ at the critical point. The tendency to a straight line for larger sizes supports a stretched exponential decay, $C_{\text{typ}}(r) \sim \exp(-\text{const.}r^{0.5})$, as expected.

a straight line with a slope of -0.38 in a log-log plot (Fig. 3.10), which is in good agreement with Fisher's prediction in (1.19). For the typical correlations, one expects a stretched exponential, $C_{\text{typ}}(r) \sim \exp(-\text{const.}\, r^{\psi})$ with $\psi = 1/2$. This can be seen in Fig. 3.11, in which the typical correlation function is plotted against $r^{1/2}$ using a logarithmic scale on the y-axis, and the data fall on a straight line.

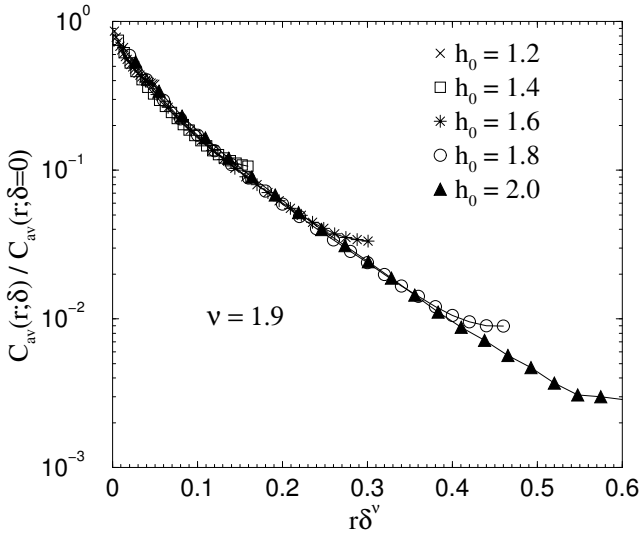

Figure 3.12: A scaling plot of the average correlation function in the disordered phase according to (3.16). The best fit gives $\nu = 1.9$, which agrees fairly well with the prediction $\nu = 2$.

We now discuss our results for the disordered phase. To obtain the correlation length exponent ν defined in (1.22), we followed [53] and used the scaling equation

$$\frac{C_{\rm av}(r;\delta>0)}{C_{\rm av}(r;\delta=0)} = \tilde{C}_{\rm av}(r/\xi) = \tilde{C}_{\rm av}(r\delta^{\nu}) \ , \tag{3.16}$$

where $\tilde{C}_{\rm av}$ is a universal scaling function of its one variable. The scaling plot for system size $L = 48$ is shown in Fig. 3.12, and gives the best fit for $\nu \approx 1.9$, fairly close to the exact value $\nu = 2$.

To estimate the dynamical exponent z, which characterizes the Griffiths-McCoy singularities, we look at the results of the local susceptibility $\chi^{\rm loc}$ calculated by (3.3). As given in (1.9), the local susceptibility is proportional to the inverse of the energy gap, so we expect that the distribution of $\chi^{\rm loc}$ will be similar to that of $1/\varepsilon$. We calculated the accumulated distribution of $\ln \chi^{\rm loc}$ for system sizes $L = 8$, 16 and 32 at the critical point, and chose the size in the imaginary time, i.e. the inverse temperature β, large enough for each L to reduce the β-dependence. As shown in Fig. 3.13(a), the distribution gets broader with increasing system size L, which indicates that $z \to \infty$ at criticality as expected. According to (1.13), the logarithm of the energy scale should vary as the square root of the length scale. This suggests that the appropriate scaling variable should be $\ln \chi^{\log}/\sqrt{L}$, as shown in Fig. 3.13(b). In the disordered phase, on the other hand, the probability distribution of energy gaps follows a power low, $\rho(\varepsilon) \sim \varepsilon^{-1+1/z}$, as discussed in Subsec. 1.4.1. The corresponding expression for the accumulated probability distributions of $\ln \varepsilon$ is

$$\ln \left[P_{\rm acc}(\ln \varepsilon) \right] = \frac{1}{z} \ln \varepsilon + {\rm const} \ , \tag{3.17}$$

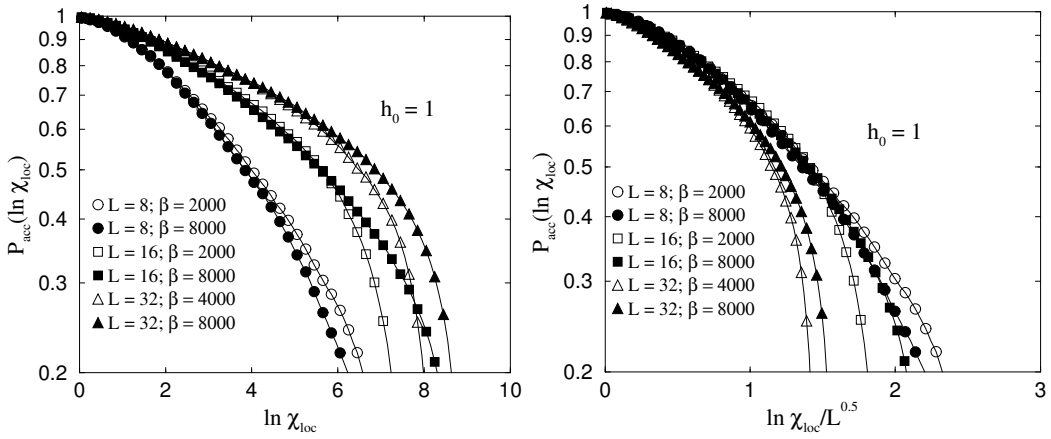

(a) (b)

Figure 3.13: (a): The accumulated distribution of the logarithm of the local susceptibility for different system sizes L at the critical point. One sees that the distribution gets broader and broader as L increases, implying an infinite dynamical exponent $z \to \infty$. (b): A scaling plot of the data in (a), assuming that the scaling variable is $\ln \chi^{\rm loc}/L^{1/2}$. One expects that the data will collapse better if the size in the imaginary time direction, i.e. the inverse temperature β, is chosen larger.

so the accumulated probability distributions of $\ln \chi^{\rm loc}$ is

$$\ln \left[P_{\rm acc}(\ln \chi^{\rm loc}) \right] = -\frac{1}{z} \ln \chi^{\rm loc} + \text{const} \ . \tag{3.18}$$

Thus, we can estimate the dynamical exponent z in the Griffiths-McCoy phase from the slopes of the expression (3.18), as shown in Fig. 3.14 for $h_0 = 2$. Repeating this calculation for other values of $h_0 > 1$, we estimated $1/z$ as a function of the deviation from criticality δ (Fig. 3.15). The results of $z(\delta)$ differ slightly from the exact values given by (1.15), or equivalently the solution of the equation for the uniform distribution [88]:

$$z \ln(1 - z^{-2}) = -\ln h_0 \quad (= -2\delta) \ . \tag{3.19}$$

This deviation may be due to the small size range we have investigated. Nevertheless, the data are compatible with the general picture: the dynamical exponent $z(\delta)$ decreases monotonically with increasing distance from the critical point, at which $z(\delta = 0) = \infty$. For $\delta \to \infty$, the dynamical exponent tends to 1. This infinite transverse field limit is the end of the Griffiths-McCoy phase in which the rare regions with strong correlations leads to singularities.

To conclude, we have been able to confirm the analytical predictions of the random transverse-field Ising chain by using continuous-time cluster algorithm. There have been some quantum Monte Carlo simulations performed on the same model, however, worked with discrete

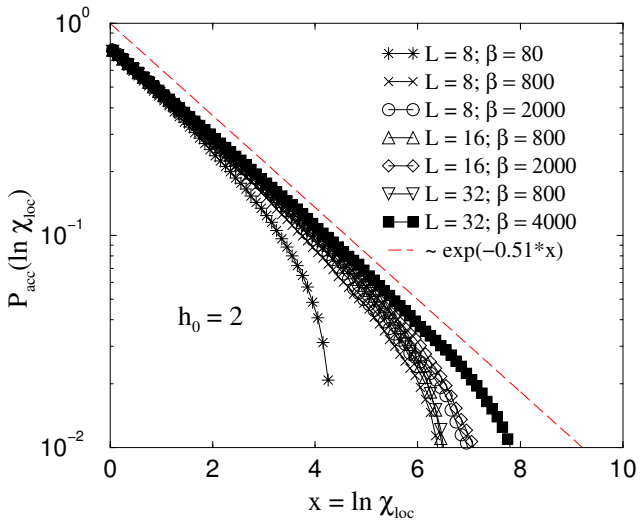

Figure 3.14: The accumulated probability distribution of the local susceptibility in the disordered phase $h_0 = 2$. The dynamical exponent $z(h_0)$ is extracted from the slope of the straight line described by the asymptotic form given in (3.18). As we can see, the data for a fixed system size show dependence on β, the size of the imaginary time dimension, if β is still smaller than the long ranged temporal correlation length. Therefore, the slope should be taken from large enough β at which no significant β-dependence appears. For $h_0 = 2$, we obtain $1/z \approx 0.51$.

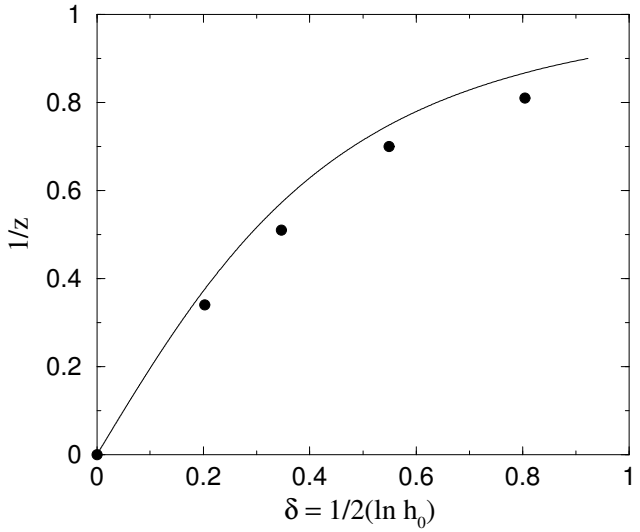

Figure 3.15: Results for $1/z$ as a function of the distance from the critical point. The data were obtained from analyzing the accumulated probability distribution of $\ln \chi^{\mathrm{loc}}$ as shown in Fig. 3.14. The limit $1/z = 0$ at the critical point $\delta = 0$ is a result from Fig. 3.13(b), as well as Fig. 3.8. The solid line gives the exact values according to (3.19).

imaginary time, which does not represent the quantum Hamiltonian exactly [44, 91]. The results we obtained do show better agreement with the analytical values, in compare to [44] in which conventional scaling was found from simulations of rather small size range, and [91] in which the exponent for decay of the average correlation at criticality was not found accurately. Other more detailed numerical studies of this model were performed by using a Jordan-Wigner transformation to map onto a problem of free fermions [53], and by applying the mapping to a random-walk problem [84]. However, these methods can only work in one dimension. In the next subsection, we will describe the results of our simulations in two dimensions.

3.3.2 The two-dimensional case

In this section we discuss the results of our simulations on the two-dimensional model with random transverse fields and bonds taken from the distributions in (3.1). The range of the linear system sizes we studied is between $L = 8$ and $L = 24$. We used up to 150 Monte Carlo sweeps for equilibration and 100-200 sweeps for measurements, which were carried out every 5 sweeps. Since a large amount of CPU time was required, the simulations for larger systems were performed on the parallel computer Cray T3E. We set up a farm topology to run a disorder realization on one single processor, so no communication between processors was needed. The question we concentrated on was whether the scaling near the quantum critical point is conventional or activated as for one dimension.

We followed the simulations we did for the one-dimensional model. First, the critical point was determined by using the special feature of the average Binder cumulant g of the variation with the inverse temperature β, cf. Fig. 3.7. We found the critical point to be located at $h_0 \approx 7.5$, where the maximal value of g is independent of L. A simple method to investigate the scaling behavior was suggested in [91]: if the critical point were to have conventional rather than activated dynamical scaling, one would expect that the data will collapse if g is plotted against $\beta/\beta_{\max}$, where $\beta_{\max}$ is the value of β at the maximum. We see in Fig. 3.16 that this does not happen. Rather the curves become broader with increasing L. This suggests that the conventional scaling variable β/L^z, corresponding to the scaling $\beta_{\max} \sim L^z$, is not appropriate, instead the scaling variable $\ln\beta/\ln\beta_{\max} \sim \ln\beta/L^\psi$ should be used. A corresponding scaling plot is shown in Fig. 3.17. From the best collapse of the scaled data, we obtain $\psi \approx 0.6$.

According the finite-size scaling form

$$g = \tilde{g}(\delta L^{1/\nu}, \ln\beta/L^\psi) \ , \tag{3.20}$$

one can determine the correlation length exponent ν by scaling the data for a fixed value of the ratio $\ln\beta/L^\psi$ once the critical exponent ψ is determined. The deviation from the critical point may be parameterized by

$$\delta = \ln h_0 - \ln h_c \ .$$

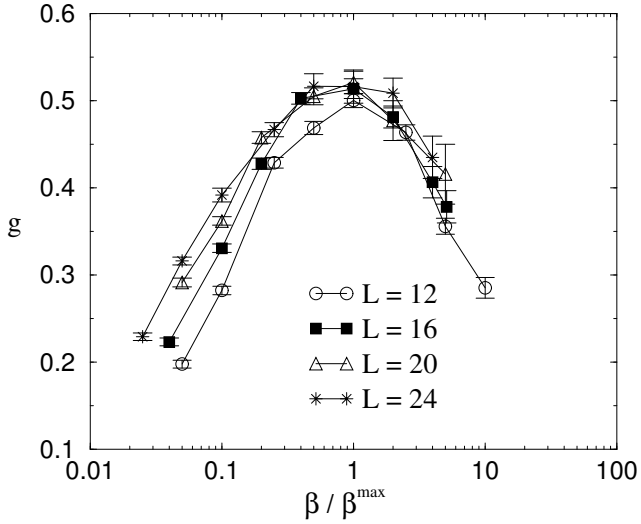

Figure 3.16: A plot of the average Binder cumulant at the estimated critical point $h_0 = 7.5$ for two dimensions. The x-axis is $\beta/\beta_{\max}$, where $\beta_{\max}$ is the value of β at the maximum of g. The curves do not collapse but rather get broader with increasing system sizes, indicating activated dynamical scaling, $z \to \infty$. The data were obtained by averaging over 400 samples for $L = 16$ with $\beta = 2000$, 250 samples for $L = 24$ with $\beta = 1600,\ 3200$, and at least 1000 samples for others.

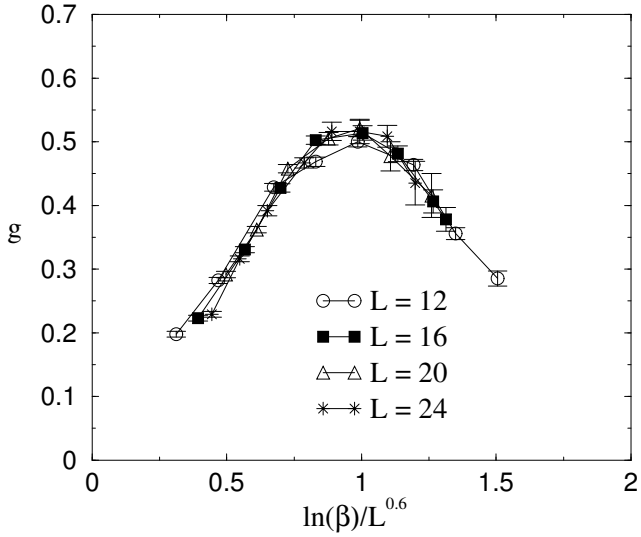

Figure 3.17: The same data as in Fig. 3.16, but with the scaling variable $\ln \beta/L^{\psi}$. The critical exponent $\psi = 0.6$ is chosen for the best collapse of the data onto a single curve. Note that the maximum in g is actually very near $\ln \beta = L^{\psi} = L^{0.6}$.

We fixed the ratio to be $\ln \beta/L^{0.6} = 1$ and scaled the values of g for system sizes L =12, 16 and 20 with various h_0 near the critical point. This is shown in Fig. 3.19, and yields

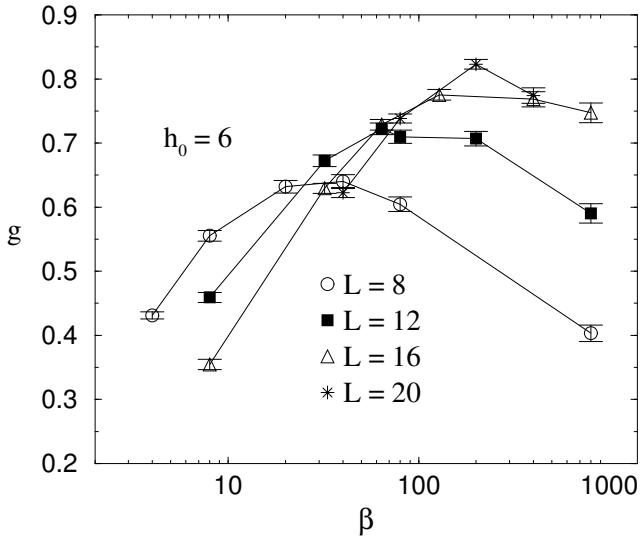

Figure 3.18: The average Binder cumulant g as a function of the inverse temperature β at $h_0 = 6$ for various system sizes L. The maxima of g increase with L, indicating that the system is in the ordered phase.

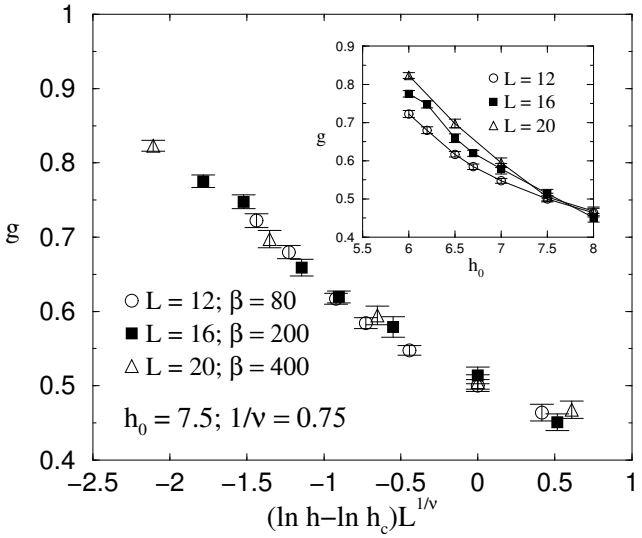

Figure 3.19: A scaling plot of the average Binder cumulant g according to (3.20), with a fixed ratio $\ln \beta / L^{0.6}$, roughly corresponding to $\beta = 80$ for $L = 12$, $\beta = 200$ for $L = 16$ and $\beta = 400$ for $L = 20$. The data collapse onto a single curve when the maximal strength of field is scaled as $\delta L^{1/\nu}$. The best collapse gives the correlation length exponent $1/\nu \approx 0.75$, corresponding to $\nu \approx 1.33$. The inset shows the unscaled data.

$\nu \approx 1.33$.

Now we turn to the spatial correlation function. We computed the correlation function given in (3.15) along the $x-$direction in the space dimension, and did this for each row of

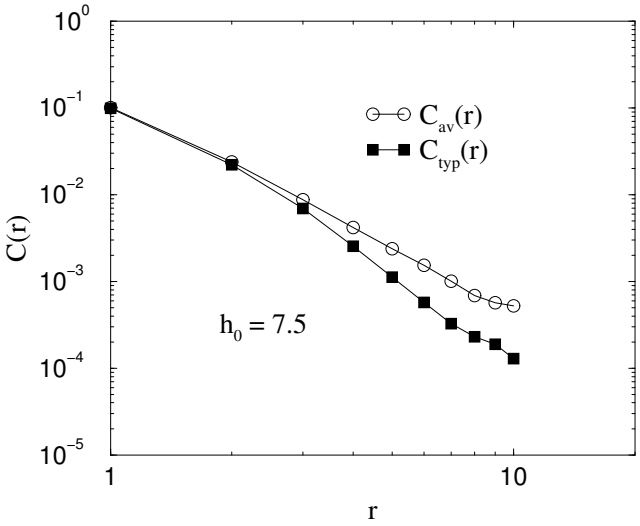

Figure 3.20: A log-log plot of the average and typical correlations at the critical point. In the similar way to $1d$ (Fig. 3.9), the average decays with a power law, while the typical shows a downward curvature, implying a stretched exponential form.

the 2-dimensional spatial lattice, i.e. we calculated

$$C(r) = \frac{2}{LL\beta} \sum_{j=1}^{L} \sum_{i=1}^{L/2} \int_0^\beta d\tau \, \langle S_i(\tau) S_{i+r}(\tau) \rangle \tag{3.21}$$

for a single sample with linear system size L, where the indices i and j run over the sites along the x- and y-direction, respectively. For each value of L, we took β such that the average Binder cumulant g is close to the peak. To probe the rare regions which dominate the average, we took at least 1000 samples. First, we compare the behavior of the average and typical correlations at the critical point. Fig. 3.20 shows that the average correlation falls off with a power law $C_{\rm av}(r; \delta = 0) \sim r^{-\eta}$, while the typical value decays faster than a power law, consistent with a stretched exponential behavior of the form $C_{\rm typ}(r; \delta = 0) \sim \exp(-\text{const. } r^{\psi_c})$. From the scaling plots shown in Fig. 3.21 for the average correlation function and Fig. 3.22 for the typical correlation function, we obtained $\eta \approx 2.3$ and $\psi_c \approx 0.58$. Our results are consistent well with the analytical prediction that the critical exponent ψ should be identical to ψ_c, provided that the fixed point has infinitely strong randomness[98].

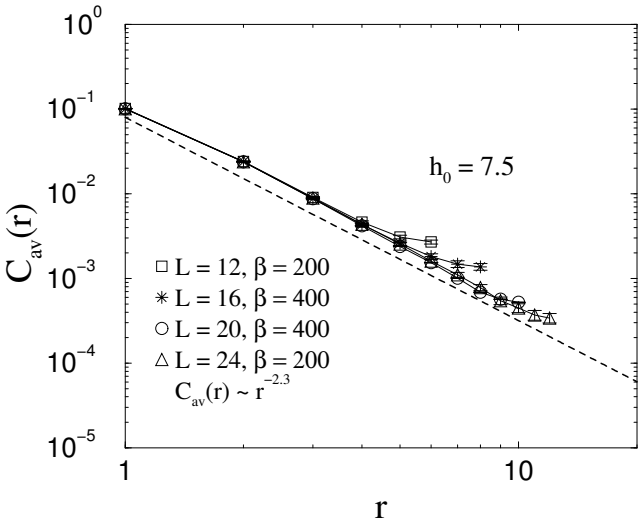

Figure 3.21: The average correlation function decays with a power law, $C_{\rm av} \sim r^{-\eta}$. The dashed line is a fit to the data for $L = 24$ with $2 \leq r \leq 8$ and has slope of -2.3.

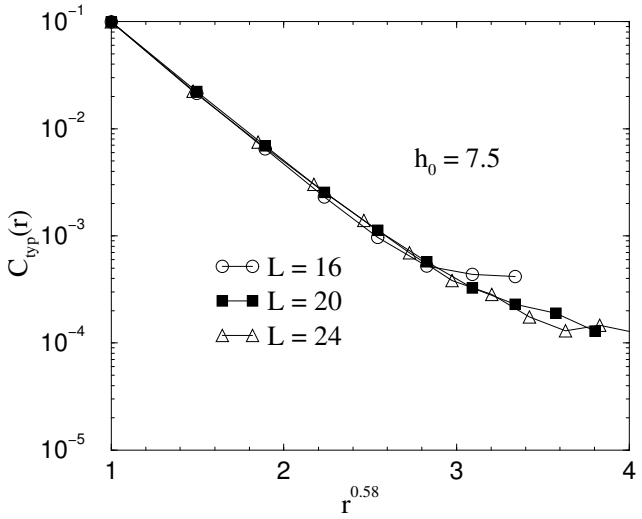

Figure 3.22: The typical correlation at the critical point falls off as the stretched exponential, $C_{\rm typ}(r) \sim (-\text{const. } r^{\psi})$. The obtained value of ψ (≈ 0.58) is consistent with that determined by scaling data for the average Binder cumulant g (Fig. 3.17).

A problem we encountered in our simulations is of the unexpected behavior of the distribution of the local susceptibility. One expects that the distribution should behave in the same way like the inverse energy gap, and get broader with increasing system size L at the critical point if it is controlled by an infinite-randomness fixed point, i.e. the dynamical exponent is infinite $z = \infty$. From the results of the average Binder cumulant and the spatial correlation function, we conclude that the critical behavior is governed by such an infinite-randomness fixed point. By contrast, the data shown in Fig. 3.23 for accumulated

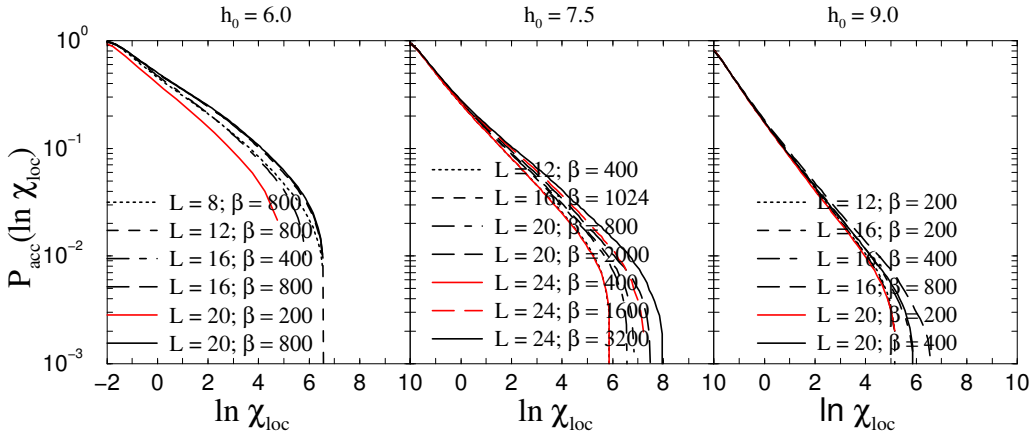

Figure 3.23: The accumulated probability distributions of the logarithmic local susceptibility in the ordered phase ($h_0 = 6$), at the critical point ($h_0 = 7.5$) and in the disordered phase ($h_0 = 9$). All of the data show no significant dependence on system sizes.

probability distributions of the logarithm of the local susceptibility have no significant dependence on system sizes at the estimated critical point $h_0 = 7.5$ as it should be, nor in the ordered phase ($h_0 = 6$) and in the disordered phase ($h_0 = 9$). One might speculate that the critical point is located below $h_0 = 6$. However, the average Binder cumulant at $h_0 = 6$ shows the behavior in the ordered phase since the maximum of g recognizably increases with L, as we can see in Fig. 3.18. One possible reason for this inconsistency may be that the values of the inverse temperature β we used for calculating $\chi^{\rm loc}$ were not large enough, so the forms of the distributions of $\ln \chi^{\rm loc}$ do not show correct dependence on L.

In summary, we have found that the critical behavior of the random transverse-field Ising model in two dimensions is indeed controlled by an infinite-randomness fixed point, i.e. $z = \infty$ at the critical point, as in one dimension. The evidence for this is provided by the activated scaling for the average Binder cumulant at the critical point, and the broad distribution of spatial correlations, with average and typical values being quite different. We have been able to estimate the critical exponents relating to the energy scale $\ln \varepsilon \sim L^{\psi}$, the correlation length $\xi \sim |\delta|^{-\nu}$ and the average spatial correlation function $C_{\rm av}(r) \sim r^{-\eta}$. These critical exponents are compatible with the results of our renormalization-group study, which will be described in Chapter 5, and other numerical work [105, 128, 91], though the difficulties in studying large system sizes and taking enough samples in quantum Monte Carlo simulations may lead to some discrepancies (Table 3.1). The distribution of the logarithm of the local susceptibility, $\ln \chi^{\rm loc}$, should provide the estimations of the dynamical exponent z in the disordered Griffiths-McCoy phase, as we have seen for the one-dimensional case. Unfortunately, for the range of sizes in imaginary time ($\beta < 3200$) we used, such estimations are difficult. Therefore, we did not study Griffiths-McCoy singularities for two-dimensional in our Monte Carlo simulations. Alternatively, one can obtain z from the distribution of the energy gap, which is expected to behave similarly as the

Table 3.1: Critical exponents of the random transverse-field Ising model in two dimensions obtained from quantum Monte Carlo simulations. The simulations in [91] were performed by using the Wolff [33] cluster algorithm with *discrete* imaginary time, which did not simulate the exact quantum Hamiltonian but a three-dimensional Ising model that is expected to be in the same universality. The results from both simulations indicate activated dynamical scaling.

	ψ	ν	η	$\psi_c = \psi$
this work	0.6	1.33	2.3	0.58
Ref. [91]	0.42	0.75	1.95	0.33

distribution of $-\ln \chi^{\mathrm{loc}}$. We conducted this investigation by performing renormalization-group simulations, which will be discussed in Chapter 5.

Chapter 4

The Ma-Dasgupta-Hu Renormalization-Group Method

4.1 Overview

A theoretical tool to analyze the low-temperature properties of quantum systems with strong disorder was introduced by Ma, Dasgupta Hu (MDH) [20, 21] for random Heisenberg antiferromagnetic chains and extended by Fisher [37, 41, 49] and others [69, 71, 75]. The strategy of this renormalization-group (RG) technique is to decrease the number of degrees of freedom and reduce the energy scale by performing successive decimation transformation in which the terms involved the highest energy in the Hamiltonian are replaced by effective terms with lower energy generated by perturbation theory. Such an approach works for systems that appear more and more disordered at ever lower energy scales, because strong disorder implies that some particular terms in the effective Hamiltonian dominate over all others, and treating the other terms perturbatively is then legitimate. There does exist one class of systems where the width of the distributions of the *logarithmic* random variables grow rapidly as the energy scale is lowered in running of RG, thus the RG yields asymptotically exact results; important examples include one-dimensional random transverse-field Ising model [37, 49] and random antiferromagnetic spin chains [41]. For these systems, the RG flow for the quantum critical point is towards a so-called *infinite-randomness fixed point* [98]. At an infinite-randomness fixed point the physical properties of system are determined by *rare events,* which occur very unlikely, but dominate the average behavior. As a result, typical and average values of some physical quantities are quite different. Furthermore, activated dynamic scaling appears at an infinite-randomness fixed point. The asymptotically exact RG analysis has also been extended into the Griffiths-McCoy phases [115, 126]. These phases are governed by lines of fixed points ending at the infinite-randomness fixed point. Along such a line, the dynamical exponent z varies continuously and diverges near the critical point.

To conclude, two of the most important special properties of the quantum phase transition with quenched disorder - activated dynamic scaling and Griffiths-McCoy singularities - can be studied within the framework of the MDH RG approach. To prepare for the discussions of our numerical implementations given in the following chapters, we will describe the RG scheme, along with highlighting its analytical results for one-dimensional transverse Ising model, XX- and Heisenberg chains in this chapter.

4.2 The MDH RG for transverse-field Ising chains

The first problem we consider is the one-dimensional random transverse-field Ising ferromagnet defined by

$$\mathcal{H} = -\sum_{<i,j>} J_{ij}\sigma_i^z\sigma_j^z - \sum_i h_i\sigma_i^x \ , \tag{4.1}$$

with ferromagnetic interactions $J_{ij} > 0$ and transverse fields $h_i > 0$ being independent random variables taken from distributions $\pi(J)$ and $\rho(h)$, respectively. The RG approach and its consequences for the low-energy properties of this model have been analyzed in greatest detail by Fisher [37, 49], and generalized by Iglói [115, 126]. A full analysis is quite technical and lengthy, and here we will be satisfied with a brief review of the essential features and results obtained in [37, 49, 115, 126] that we are interested in.

4.2.1 The renormalization-group scheme in one dimension

The renormalization-group procedure is as follows: Find the strongest coupling $\Omega \equiv \max\{J_{ij},\, h_i\}$ in the system. If the strongest coupling is a field, $\Omega = h_i$, then the associated local field term has a ground state $|{\rightarrow}\rangle_i = \left(|{\uparrow}\rangle_i + |{\downarrow}\rangle_i\right)/\sqrt{2}$, and excited state $|{\leftarrow}\rangle_i = \left(|{\uparrow}\rangle_i - |{\downarrow}\rangle_i\right)/\sqrt{2}$ separated by an energy gap $2h_i$. We focus on the three-spin Hamiltonian involving the spin σ_i and its two neighboring spins:

$$\mathcal{H}' = \mathcal{H}_0' + \mathcal{H}_I' \ , \tag{4.2}$$

where

$$\mathcal{H}_0' = -h_i\sigma_i^x \ , \tag{4.3}$$

$$\mathcal{H}_I' = -J_{i-1,i}\sigma_{i-1}^z\sigma_i^z - J_{i,i+1}\sigma_i^z\sigma_{i+1}^z \ . \tag{4.4}$$

If the probability distributions for transverse field $\rho(h;\Omega)$ and for the bond $\pi(J;\Omega)$ at energy scale Ω are broad, $J_{i-1,i}$ and $J_{i,i+1}$ are typically much smaller than h_i. $\mathcal{H}_I'$ can then be treated by second-order perturbation theory. This yields an effective Hamiltonian

$$\widetilde{\mathcal{H}'} = -\widetilde{J}_{i-1,i+1}\widetilde{\sigma}_{i-1}^z\widetilde{\sigma}_{i+1}^z \tag{4.5}$$

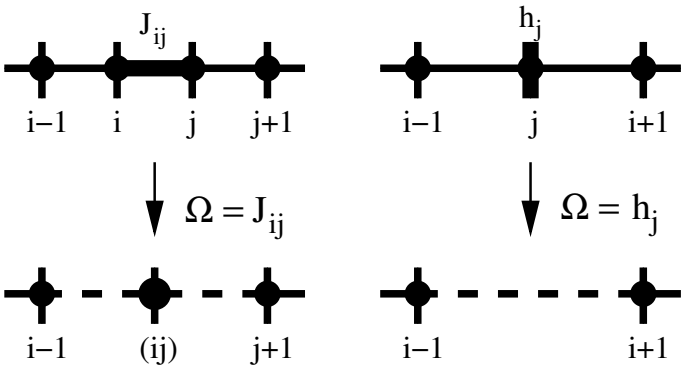

Figure 4.1: Schematic picture of the renormalization procedure for random transverse-field Ising chain. **left:** a cluster aggregation process; **right:** a cluster annihilation process.

with the effective bond

$$\widetilde{J}_{i-1,i+1} \approx \frac{J_{i-1,i}J_{i,i+1}}{h_i} \ . \tag{4.6}$$

If instead the largest coupling is a bond, $\Omega = J_{ij}$, then the neighboring transverse fields h_i and h_j can be treated as a perturbation of second order to the involved term $-J_{ij}\sigma_i^z\sigma_j^z$, which has two degenerate ground states $|\uparrow\rangle_i|\uparrow\rangle_j$ and $|\downarrow\rangle_i|\downarrow\rangle_j$ separated from the two excited states by a gap $2J_{ij}$. Doing this in second-order perturbation theory, the two spins on sites i and j are replaced by a single spin (cluster) with an effective transverse field

$$\widetilde{h}_{(ij)} \approx \frac{h_i h_j}{J_{ij}} \ , \tag{4.7}$$

and an effective magnetic moment

$$\widetilde{\mu}_{(ij)} = \mu_i + \mu_j \ . \tag{4.8}$$

The bond of the new spin cluster with the neighbors remain unchanged to leading order. We iterate this procedure with the energy scale $\Omega = \{\widetilde{h}_i, \widetilde{J}_i\}$ of the effective Hamiltonian being gradually lowered till on the order of the energy at which we wish to study the system.

Each step of RG described above eliminates one cluster: when the strongest coupling is a field, the corresponding cluster is annihilated, while when it is a bond, the two clusters on its both sides are rigidly locked together as a larger cluster, as depicted in Fig. 4.1. We use the terminology introduced in [98, 105] and call the former an annihilation process, the latter an aggregation process. In the disordered phase, the fields tend to dominate the bonds at low energy, so the annihilation process occurs more frequently than the aggregation process at small Ω and no large clusters can be formed. In the ordered phase, in contrast, the aggregation process dominates and this causes large clusters, eventually an infinite cluster, to form. The quantum critical point separating these phases is thus a novel type of percolation transition at which the annihilation and aggregation processes balance at all energy scales.

The condition for validity of the RG is that the distributions of the bonds and fields be broad so that the errors made by the second-order perturbation approximation used in deriving (4.6) and (4.7) is permissible. Since the RG recursion relations have the multiplicative form and the effective bonds $\{\widetilde{J}_{ij}\}$ and fields $\{\widetilde{h}_i\}$ remain independent under renormalization, the distributions of the logarithmic couplings, $\ln \widetilde{J}$ and $\ln \widetilde{h}$, do indeed broaden with decreasing Ω. This suggests that the cutoff coupling chosen to be decimated will typically have magnitude much larger than its perturbations. The perturbative decimation approximation thus becomes better and better under renormalization.

4.2.2 Renormalization-group flows in one dimension

A complete understanding of the critical behavior requires an analysis of the effects of iterating the basic RG procedure on the distributions of couplings $\rho(h;\Omega)$ and $\pi(J;\Omega)$. From the form of the recursion relations (4.6) and (4.7), it is clear that it is more convenient to work in terms of the logarithmic variables: $\zeta_{ij} \equiv \ln(\Omega/J_{ij})$ and $\beta_i \equiv \ln(\Omega/h_i)$. Thus, the transforms (4.6)and (4.7) become

$$\widetilde{\zeta}_{i-1,i+1} \approx \zeta_{i-1,i} + \zeta_{i,i+1}$$

and

$$\widetilde{\beta}_{(ij)} \approx \beta_i + \beta_j \ .$$

Also define logarithmic energy scales $\Gamma \equiv \ln(\Omega_0/\Omega)$, where Ω_0 is the energy scale of the initial Hamiltonian. We denote the total number of clusters (or bonds) at scale Γ by $N(\Gamma)$, the total number of log-fields of strength β at this scale by $N_f(\beta;\Gamma)$, and similarly the total number of bonds of strength ζ by $N_b(\zeta;\Gamma)$. Then, the normalized probability distribution for bonds and transverse fields denoted by $P(\zeta;\Gamma)$ and $R(\beta;\Gamma)$ respectively can be expressed as

$$P(\zeta;\Gamma) = \frac{N_b(\zeta;\Gamma)}{N(\Gamma)} \ , \qquad R(\beta;\Gamma) = \frac{N_f(\beta;\Gamma)}{N(\Gamma)} \ . \tag{4.9}$$

As Γ is increased by $d\Gamma$, all log-fields with $0 < \beta_i < d\Gamma$ and log-bonds with $0 < \zeta_{ij} < d\Gamma$ are removed. Since each decimation reduces the number of cluster by 1, we have

$$N(\Gamma + d\Gamma) = N(\Gamma) - d\Gamma \left[N_f(0;\Gamma) + N_b(0;\Gamma)\right] . \tag{4.10}$$

The transformation (4.6), in which the cluster with $\beta = 0$ is decimated, will eliminate two bonds and generate a new one. This leads to [49, 118]:

$$\begin{aligned} N_b(\zeta;\Gamma + d\Gamma) &= N_b(\zeta - d\zeta;\Gamma) + d\Gamma \int d\zeta_1 d\zeta_2 N_f(0;\Gamma) P(\zeta_1;\Gamma) P(\zeta_2;\Gamma) \\ &\quad \times \left[\delta(\zeta - \zeta_1 - \zeta_2) - \delta(\zeta - \zeta_1) - \delta(\zeta - \zeta_2)\right] \ . \end{aligned} \tag{4.11}$$

the first term in the square brackets arises from a new bond generated when the cluster with $\beta = 0$ is decimated, while the next two terms represent the elimination of the two neighboring bonds of the decimated cluster. A similar result is obtained for $N_f(\beta;\Gamma)$ from the transformation (4.7). From (4.9)-(4.11), we obtain the RG flow equations for the distributions $P(\zeta;\Gamma)$ and $R(\beta;\Gamma)$:

$$\begin{aligned}\frac{\partial P(\zeta;\Gamma)}{\partial\Gamma} &= \frac{\partial P(\zeta;\Gamma)}{\partial\zeta} + [P(0;\Gamma) - R(0;\Gamma)]\, P(\zeta;\Gamma) \\ &\quad + R(0;\Gamma)\int d\zeta_1 d\zeta_2 P(\zeta_1;\Gamma)P(\zeta_2;\Gamma)\delta(\zeta-\zeta_1-\zeta_2); \end{aligned} \tag{4.12}$$

$$\begin{aligned}\frac{\partial R(\beta;\Gamma)}{\partial\Gamma} &= \frac{\partial R(\beta;\Gamma)}{\partial\beta} + [R(0;\Gamma) - P(0;\Gamma)]\, R(\beta;\Gamma) \\ &\quad + P(0;\Gamma)\int d\beta_1 d\beta_2 R(\beta_1;\Gamma)R(\beta_2;\Gamma)\delta(\beta-\beta_1-\beta_2)\ . \end{aligned} \tag{4.13}$$

4.2.2.1 The RG flows in the vicinity of the critical point

A detailed analysis the RG flows was performed in [49] leading to the following conclusions: For not very singular initial distributions,[1] the RG flows of the log-coupling distributions (4.12) and (4.13) are characterized by a family of solutions in the form:

$$P(\zeta;\Gamma) = P(0;\Gamma)e^{-P(0;\Gamma)\zeta}\ . \tag{4.14}$$

and

$$R(\beta;\Gamma) = R(0;\Gamma)e^{-R(0;\Gamma)\beta} \tag{4.15}$$

At the critical fixed point where $R = P$ due to duality between h's and J's, it can be shown that the RG solutions are attracted to an unique fixed-point distribution:

$$P(0;\Gamma) = R(0;\Gamma) = 1/\Gamma\ . \tag{4.16}$$

We see that the widths of the two fixed point distributions on the logarithmic scale grow linearly with Γ, i.e. they grow without limit as $\Omega \to 0$. This is the indication that the RG flows go to an infinite-randomness fixed point and the approximate RG is exact in this limit.

To establish the connection between the length scale and the energy scale, we need to know the average spacing between the clusters at a characteristic energy scale Γ. From (4.9) and

[1] The system with highly singular distributions of the couplings J_{ij} and h_i have different critical behavior than the generic case discussed in this section. We will discuss the effects of such singular initial distributions in Chapter 6.

(4.11), we obtain the evolution of the number density n_Γ of the remaining clusters (or equivalently bonds) at energy scale Γ

$$\frac{dn_\Gamma}{d\Gamma} = -n_\Gamma[R(0;\Gamma) + P(0;\Gamma)] \ .$$

Using the fixed-point distribution (4.16), we have $n_\Gamma \sim 1/L \sim 1/\Gamma^2$. This gives the relationship between the length scale and the energy scale at criticality:

$$\Gamma = \ln\left(\frac{\Omega_0}{\Omega}\right) \sim L^\psi \ , \tag{4.17}$$

with $\psi = 1/2$. This is very different from conventional power-law scaling, $\Omega \sim L^{-z}$, and yields an infinite dynamical exponent $z \to \infty$. In addition to the energy scale, one keeps track of the average magnetic moments μ of the clusters (4.8). This yields an exponent $\phi = \frac{1+\sqrt{5}}{2}$, which controls the scaling of the magnetic moments: $\mu \sim \Gamma^\phi$.

Fisher also carried out a detailed analysis of the flow equations slightly away from the critical point, introducing the quantum control parameter

$$\delta = \frac{[\ln h]_{\rm av} - [\ln J]_{\rm av}}{\mathrm{var}(\ln h) + \mathrm{var}(\ln J)} \ . \tag{4.18}$$

At the energy scale of order $\Gamma_\delta \sim 1/|\delta|$, the RG flows is roughly the same as at the critical point. From the length scaling $l \sim \Gamma^2$, it can then be found another exponent $\nu = 2$ relating to correlation length via $\xi \sim |\delta|^{-\nu}$.

The three critical exponents ψ, ϕ and ν introduced above, which are related to the strongly coupled clusters and their geometric properties, can fully characterize the unusual scaling properties governed by an infinite-randomness fixed point [98], as we have seen in Sec. 1.5. The strongly coupled clusters for site or bond *dilution* are simply the connected clusters. Hence the critical exponents defined above are directly related to the classical percolation exponents [59]: Let $\delta = p - p_c$ be the distance from the percolation threshold, $\nu_{\rm perc}$ the exponent for the typical cluster size, $D_{\rm perc}$ the fractal dimension of the percolating cluster, $\beta_{\rm perc}$ the exponent for the probability to belong to the percolating cluster. Then one has for the critical exponents:

$$\nu = \nu_{\rm perc} \ , \quad \psi = D_{\rm perc} \ , \quad \phi = (d - \beta_{\rm perc}/\nu_{\rm perc})/D_{\rm perc} \ .$$

4.2.2.2 The RG flows in the Griffiths-McCoy regions

We now turn to a discussion of the ordered and disordered phases further away from the transition. In the disordered phase ($\delta > 0$), it is more likely that a cluster of spins gets decimated. When that happens, a weaker bond between the neighboring clusters of the

decimated cluster is generated. Therefore, the width of the bond distribution grows faster than the field distribution. In the ordered phase, the situation is reversed: Almost all the decimations are of bonds. Thus, larger and larger clusters are joined together as the energy scale is decreased. In this case, the field distribution gets broader and broader under renormalization, while the width of the bond distribution saturates.

It has been turned out that the validity of the RG method is not only limited in the vicinity of the criticality but also extents over the whole Griffiths-McCoy region [115, 126]. The solutions of the RG flows, (4.14) and (4.15), in terms of the original variables J, h, and Ω:

$$\pi(J,\Omega) = \pi(\Omega,\Omega)(\Omega/J)^{1-\pi(\Omega,\Omega)} \tag{4.19}$$

$$\rho(h,\Omega) = \rho(\Omega,\Omega)(\Omega/h)^{1-\rho(\Omega,\Omega)} \tag{4.20}$$

are parameterized by $z = z(\delta)$ via $\Omega(\rho(\Omega,\Omega) - \pi(\Omega,\Omega)) = 1/z$.

In the paramagnetic phase $\delta > 0$, the rare strongly coupled clusters dominate the susceptibility. The density of such clusters at scale $\Omega \to 0$ has the asymptotic behavior $n_\Omega \sim \Omega^{1/z(\delta)}$, so that z relates length and energy scales and can be identified as the dynamical exponent, which characterizes the Griffiths-McCoy effect [115]. Iglói et. al. showed that the parameter z is invariant along the RG trajectory and is given by the solution of the equation:

$$\left[\left(\frac{J}{h}\right)^{1/z}\right]_{\text{av}} = 1 \ , \tag{4.21}$$

which is indeed the exact $z(\delta)$-relation reported in [88].

The asymptotically exact properties of the RG method thus maintain in the whole Griffiths-McCoy phase, and the dynamical exponent $z(\delta)$ calculated by the RG method is exact.

4.3 The MDH RG for XX- and Heisenberg chains

In this section we summarize the analytical results of random antiferromagnetic quantum spin chains obtained by using the MDH RG approach [20, 21, 41, 56]. We consider the Hamiltonian

$$\mathcal{H} = \sum_{<i,j>} J_{ij}^x S_i^x S_j^x + J_{ij}^y S_i^y S_j^y + J_{ij}^z S_i^z S_j^z \tag{4.22}$$

where S_i^α are the spin operators and $J_{ij}^\alpha > 0$ are random positive interactions between nearest neighboring spins. In this section and later in our numerical implementation we will only focus on isotropic case, i.e. the XXX-model with $J_{ij}^x = J_{ij}^y = J_{ij}^z \equiv J_{ij}$ and the XX-model with $J_{ij}^x = J_{ij}^y \equiv J_{ij}$, $J_{ij}^z = 0$. We will begin with the MDH RG scheme in the following section.

4.3.1 The renormalization-group procedure

Consider an antiferromagnetic nearest-neighbor Heisenberg spin-S chain in which the largest coupling is J_{23}. The part of the Hamiltonian involving J_{23} is

$$\mathcal{H}_0' = J_{23}\mathbf{S}_2 \cdot \mathbf{S}_3 \ , \tag{4.23}$$

which is weakly coupled to the neighbors via

$$\mathcal{H}_I' = J_{12}\mathbf{S}_1 \cdot \mathbf{S}_2 + J_{34}\mathbf{S}_3 \cdot \mathbf{S}_4 \ . \tag{4.24}$$

In the degenerate ground state of $\mathcal{H}_0'$ the spins $\mathbf{S}_3$ and $\mathbf{S}_4$ form a singlet. Following [20, 21, 41, 71], We treat $\mathcal{H}_I'$ as a perturbation to $\mathcal{H}_0'$. Since the first-order contribution is zero, we have to do in a second-order perturbation theory to calculate the energy shift:

$$\Delta^{(2)} \equiv \sum_e \frac{\langle g|\, \mathcal{H}_I' \,|e\rangle \, \langle e|\, \mathcal{H}_I' \,|g\rangle}{E_0 - E_e} \ , \tag{4.25}$$

where $|g\rangle$ is a ground state of $\mathcal{H}_0'$ with energy E_0, and the sum is over all excited state $|e\rangle$ with energy E_e. To get an effective coupling between $\mathbf{S}_1$ and $\mathbf{S}_4$, we are only interested in the terms proportional to $J_{12}J_{34}$. The result of the calculation can be expressed in terms of an effective Hamiltonian resulting from the projection onto the singlet state formed by $\mathbf{S}_2$ and $\mathbf{S}_3$:

$$\widetilde{\mathcal{H}'} = \text{const} - \sum_\alpha \frac{2J_{12}J_{34}}{J_{23}} \langle 0|\, S_2^\alpha S_3^\alpha \,|0\rangle \, S_1^\alpha S_4^\alpha \ , \tag{4.26}$$

where $|0\rangle$ denotes the singlet formed by $\mathbf{S}_2$ and $\mathbf{S}_3$. Using

$$\langle 0|\, S_2^\alpha S_3^\beta \,|0\rangle = \frac{1}{3}\delta^{\alpha\beta} \langle 0|\, \mathbf{S}_2 \cdot \mathbf{S}_3 \,|0\rangle = -\frac{1}{3}\delta^{\alpha\beta} S(S+1) \ , \tag{4.27}$$

we obtain

$$\widetilde{\mathcal{H}'} = \text{const} + \frac{2J_{12}J_{34}S(S+1)}{3J_{23}} \mathbf{S}_1 \cdot \mathbf{S}_4 \ . \tag{4.28}$$

Thus, this RG transformation generates an effective bond between the spins $\mathbf{S}_1$ and $\mathbf{S}_4$ with the strength

$$\widetilde{J}_{14} \approx \frac{2}{3} S(S+1) \frac{J_{12}J_{34}}{J_{23}} \ , \tag{4.29}$$

while removing the strongest coupling J_{23}, and also the pair of strongly coupled spins $\mathbf{S}_2$ and $\mathbf{S}_3$.

For the Heisenberg spin-1/2 chain, the effective coupling (4.29) is given by

$$\widetilde{J}_{14} \approx \frac{J_{12}J_{34}}{2J_{23}} \ , \tag{4.30}$$

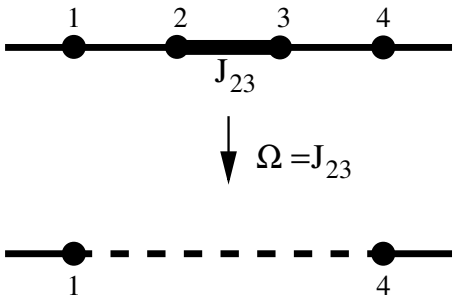

Figure 4.2: Schematic picture of MDH renormalization procedure for the XXX- (XX-) chain.

which is weaker than the decimated bond J_{23}. The corresponding renormalized coupling in the spin-1 chains is

$$\widetilde{J}_{14} \approx \frac{4J_{12}J_{34}}{3J_{23}} \ . \tag{4.31}$$

Consequently, when the couplings J_{12} and J_{34} are not small enough, the renormalized coupling $\widetilde{J}_{14}$ may be larger than the eliminated J_{23}, so that the RG method works only for broad initial randomness. The derivation of the renormalized coupling for the XX spin-1/2 chain is similar to the Heisenberg chain described above. The recursion relation becomes [41]

$$\widetilde{J}_{14} \approx \frac{J_{12}J_{34}}{J_{23}} \tag{4.32}$$

when the strong bond J_{23} is decimated.

Repeating the RG procedure with decreasing energy scale, Ω, set by the strongest coupling in the chain, conserves the form of the Hamiltonian in the original model, but changes the distribution of couplings $P(J;\Omega)$, which can be studied analytically for spin-1/2 and spin-1 chains, as we will discuss in the nest section.

4.3.2 The analytical results

The analysis of the strong-disorder RG shows that the isotropic random XX spin-1/2 chain with $J^x_{ij} = J^y_{ij} \equiv J_{ij}$, $J^z_{ij} = 0$ and the random Heisenberg (XXX) spin-1/2 chain with $J^x_{ij} = J^y_{ij} = J^z_{ij} \equiv J_{ij}$ behave in essentially the same way and will be in the *random singlet (RS) phase* [21, 41], in which all spins are paired and form singlets. The form of the recursion relation (4.32) for the XX spin-1/2 chain is indeed similar to those for the transverse-field Ising chain discussed in the previous section. In addition, the factor 2 occurring in the recursion equations (4.30) for the Heisenberg spin-1/2 chain is irrelevant at the critical fixed-point [41, 56, 58]. Therfore, the fixed-point distributions for the XX-, XXX-chain with spin-1/2 and transverse-field Ising chain are expected in the same form. For generic initial disorder distributions (non-extremely singular), the probability

distributions of the couplings flow towards a fixed-point form [41]:

$$\pi^*(J;\Omega) \approx \frac{1}{z\Omega}\left(\frac{J}{\Omega}\right)^{-1+1/z} \tag{4.33}$$

with the dynamical exponent z given by

$$z \approx \ln\left(\frac{\Omega_0}{\Omega}\right) \equiv \Gamma \ , \tag{4.34}$$

where Ω_0 denotes the initial energy scale. The dynamical exponent z, which is used to relate the length scale, L, and energy scale, Ω, via $\Omega \sim L^{-z}$, tends to infinity at the fixed point (an infinite-randomness fixed point), suggesting an activated dynamical scaling:

$$\Gamma \sim L^{\psi} \ . \tag{4.35}$$

From the evolution of the fraction of spins n_Γ which are left at a given energy scale Γ, one obtains the exponent $\psi = 1/2$ in (4.35). The fixed-point solutions in (4.33) imply that the distribution of bonds becomes broader and broader even on the logarithmic scale. This dramatic broadening of the bond distributions under renormalization is the key feature that the RG approach becomes asymptotically accurate in the low-energy limit.

The phase in the antiferromagnetic spin-1/2 chains characterized by the universal bond distributions given in (4.33) is referred to as the random singlet phase [41]. In a RS phase each spin forms a singlet with another spin which may be located far away. We can induce a phase transition by introducing dimerization or anisotropy in the bonds. Here we consider the case with dimerization, and assume the distribution functions for even bonds and odd bonds are $\pi_e(J^e;\Omega_0)$ and $\pi_o(J^o;\Omega_0)$, respectively. We define a dimensionless parameter δ to characterize the strength of the dimerization:

$$\delta_{\rm dim} = \frac{[\ln J^e]_{\rm av} - [\ln J^o]_{\rm av}}{\mathrm{var}(\ln J^e) + \mathrm{var}(\ln J^o)} \ . \tag{4.36}$$

Without dimerization, $\delta_{\rm dim} = 0$, the fixed-point distribution of bonds correspond to (4.33):

$$\pi_e(J^e;\Omega) = \pi_o(J^o;\Omega) = \pi^*(J;\Omega) \ . \tag{4.37}$$

With dimerization $\delta \neq 0$, the system is driven to a so-called *random dimer (RD) phase* [56]. Assuming that, e.g. even bonds are stronger than odd bonds on average, the even bonds are correspondingly more likely to be decimated. Since the decimation of an even bond leaves a weaker renormalized odd bond behind, the width of the odd bond distribution grows faster than the even bond distribution. As a result, the separation in energy scale between even and odd bonds becomes more and more pronounced until almost all singlet pairs are formed over even bonds. The area having singlets on odd bonds (in this case) forms local "wrong region".

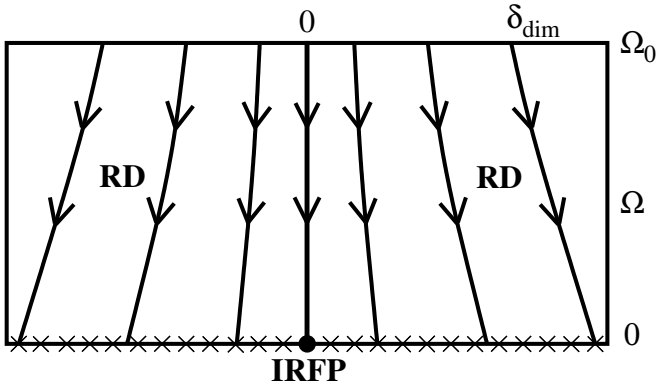

Figure 4.3: Schematic RG phase diagram of the random dimerized spin-1/2 chain as a function of the quantum control parameter $\delta_{\rm dim}$ and the energy scale Ω. Along the RG trajectories the dynamical exponent $z(\delta_{\rm dim})$ is constant. The non-dimerized model with $\delta_{\rm dim} = 0$ is attracted by an infinite-randomness fixed point with $1/z = 0$. The randomness grows with decreasing energy scale Ω. From [127].

The RD phase is an example of Griffiths-McCoy phase. The non-universal dynamical exponent z, which characterizes the singular behavior of some physical quantities, such as the susceptibility $\chi \sim T^{1/z(\delta)-1}$ and the specific heat $C \sim T^{1/z(\delta)}$, stays invariant under renormalization [115, 126], and can be calculated by RG method, in particular for the XX-chain, z is given by the solution of the equation

$$\left[\left(\frac{J^e}{J^o}\right)^{1/z(\delta)}\right]_{av} = 1 \; . \tag{4.38}$$

The schematic RG-diagram of the random dimerized chain is sketched in Fig. 4.3.

Now, we turn to the Heisenberg spin-1 chain. According to Haldane's conjecture [23], the spectrum of the pure Heisenberg chain with spin-1 is gapped (Haldane gap), in contrast to the pure Heisenberg spin-1/2 chain. The Haldane gap is stable against weak randomness [56, 83]. When randomness is strong, the Haldane gap can be destroyed, and the system undergoes a phase transition from the Haldane phase to the random singlet phase. This is concluded by Hyman et. al [69] and Monthus et. al [86] using extended RG procedures, which are designed to cure the problem that in the MDH RG method renormalized couplings may be larger than decimated couplings because of the coefficient $3/4$ in (4.31). The basic idea of these modified RG methods is to map the original spin-1 chain to an effective model with entirely spin-1/2 degrees of freedom coupled by either ferromagnetic or antiferromagnetic bonds (in [86] a variant of the effective model was introduced), which is argued to describe the low-energy properties of the original system. This effective model can be analyzed using the extension of the RG.

The analysis of the RG procedure shows that the infinite-randomness fixed point that controls the random singlet phase will be attractive if the initial distribution is strongly random

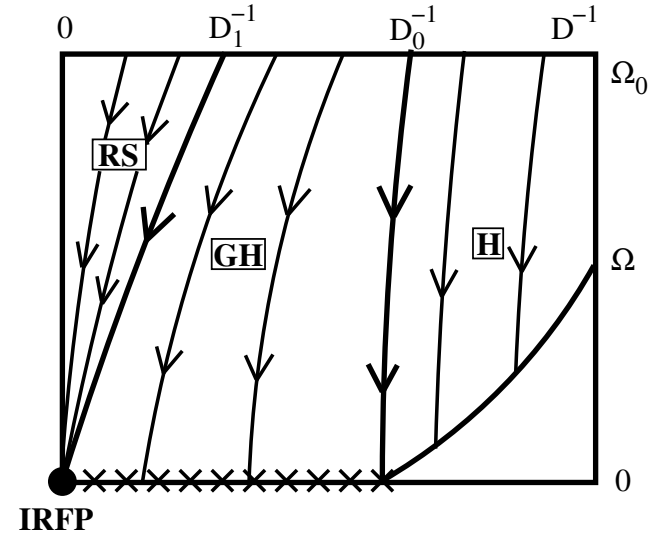

Figure 4.4: Schematic RG phase diagram of the random AF spin-1 chain, as a function of the disorder strength D and the energy scale Ω. For weak disorder, $D < D_0$, there is a Haldane (H) gap in the spectrum. For intermediated disorder, $D_0 < D < D_1$ the system is in the gapless Haldane (GH) phase with a varying dynamical exponent $z(D)$. For strong enough disorder, $D > D_1$ the system is in the random singlet phase (RS) and scales into the infinite-randomness fixed point. From [127].

[69, 86, 108]. For the initial disorder distribution in a power-law form:

$$\pi(J) = \frac{1}{D} J^{-1+1/D} \tag{4.39}$$

with D representing the strength of randomness, the distribution will flow toward the infinite-randomness fixed-point form and the system will be in the random singlet phase with an infinite dynamical exponent, providing the strength of disorder exceeds a critical value D_1; For weak randomness, say $D < D_0$, the system stays in the Haldane phase where the spectrum has a gap; With an intermediate range of disorder, $D_0 < D < D_1$, the Haldane gap will be filled and the system will be in the so-called gapless Haldane (GH) phase where the dynamical exponent $z = z(D) > 1$ is a monotonously increasing function of the disorder. The GH phase is similar to the dimerized phases of the spin-1/2 chains and is an example of the Griffiths-McCoy phase. Fig. 4.4 shows a schematic RG phase diagram of the random Heisenberg spin-1 chain.

The $S = 1$ Heisenberg chain is closely related to the antiferromagnetic $S = 1/2$ Heisenberg ladder [54]. In Chapter 7 we will extend the RG-study to spin ladders with strong disorder.

Chapter 5

Numerical Renormalization-Group Study of Random Transverse Ising Models

The Ma-Dasgupta-Hu (MDH) renormalization-group (RG) method designed for strongly disordered quantum systems can be used analytically to study the critical and off-critical properties in one dimension, as we have seen in the previous chapter. To perform the RG in higher dimensions $d > 1$, we have to rely on numerical simulations. In this chapter we will discuss our numerical study of random transverse-field Ising models (4.1) using the MDH RG approach and present the results. In our simulations we imposed periodic boundary conditions, and used the following rectangular forms

$$\pi(J) = \begin{cases} 1, & \text{for } 0 < J < 1 \\ 0, & \text{otherwise} \end{cases} \tag{5.1}$$

and

$$\rho(h) = \begin{cases} h_0^{-1}, & \text{for } 0 < h < h_0 \\ 0, & \text{otherwise} \end{cases} , \tag{5.2}$$

for initial bond and field distributions. The maximal strength of the transverse fields serves as the control parameter to drive the phase transition. The distributions of disorder is regular, so that the results mentioned in the previous chapter can be checked in one dimension. The RG study for a highly singular initial disorder distribution will be discussed in the next chapter.

5.1 The numerical RG scheme in higher dimensions

The numerical implementation of the RG scheme for one-dimensional case described in Sec. 4.2.1 is straightforward. One generates a spin chain with transverse fields and bonds

following independent probability distributions, and then successively eliminates one spin via the annihilation or aggregation process along with renormalizations of the transverse fields and reconnections of the bonds.

The RG scheme can be extended to higher dimensions $d > 1$: we start each simulation by generating a $d-$dimensional lattice with spins on lattice points and bonds between nearby pairs of spins, according to independent probability distributions for transverse fields and bonds. Because of the multiplicative structure of the transforms (4.6) and (4.7), it is convenient to work with the logarithmic variables defined by $\theta_i \equiv \ln h_i$ and $\kappa_{ij} \equiv \ln J_{ij}$. In each RG step we pick up the strongest log-coupling, which is either a log-field θ_k or a log-bond κ_{ij}; its strength sets the logarithmic energy scale of this RG step. If the largest log-coupling is the log-field on spin σ_k, we execute an annihilation process to remove the spin σ_k, and generate effective bonds between neighboring spins of σ_k by using second order perturbation theory, as discussed in Sec. 4.2.1. For each pair (i, j), the renormalized bond are given by

$$\widetilde{J}_{ij} \approx J_{ij} + \frac{J_{ik}J_{kj}}{h_k} \approx \max\left(J_{ij}, \frac{J_{ik}J_{kj}}{h_k}\right) , \tag{5.3}$$

where we compare the new effective bonds of the form $J_{ik}J_{kj}/h_k$ with the bonds that were already present, and only keep the stronger one, as suggested in [105]. This is satisfied in the strong-randomness limit where one of the two bonds is generally much stronger than the other. Using this approximation, calculating the logarithm of bonds becomes simpler. The transform in terms of log-couplings now become

$$\widetilde{\kappa}_{ij} = \max\left(\kappa_{ij}, \kappa_{ik} + \kappa_{kj} - \theta_k\right) . \tag{5.4}$$

If instead the largest log-coupling is the log-bond connecting the spins on sites i and j, it follows an aggregation process in which we put the two spins i and j into a cluster and assign the cluster a renormalized log-field given by

$$\widetilde{\theta}_{(ij)} = \theta_i + \theta_j - \kappa_{ij} , \tag{5.5}$$

and a renormalized moment

$$\widetilde{\mu}_{(ij)} = \mu_i + \mu_j .$$

The renormalized log-bonds connecting with each remaining neighbor spin k of spin i and j are

$$\widetilde{\kappa}_{(ij)k} \approx \max(\kappa_{ik}, \kappa_{jk}) .$$

As shown in Fig. 5.1, the RG for $d > 1$ does not preserve the spatial structure of the lattice but instead generates a random graph with clusters being vertices and bonds being edges. The major complication for performing RG in $d > 1$ is that a large number of weak bonds, which may be up to $N(N-1)/2$ for N remaining spins, are generated under renormalization, so computer memory capacity may be exceeded in running the RG for

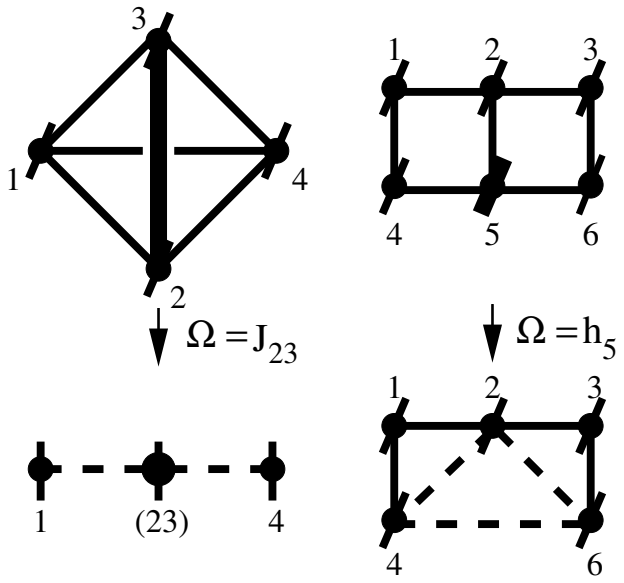

Figure 5.1: Renormalization-group decimations for two-dimensional lattice. **left:** an aggregation process; **right:** an annihilation process. The dashed lines represent renormalized bonds.

large lattices. It has pointed out in [105] that we could get over this problem by discarding weak bonds below some minimum strength $J_{\min}$ chosen as small as possible or decreased steadily as $\Omega \to 0$. Doing this, we might, however, lose some information from the low-energy part of the bond distribution.

An improved way to discard the weak bonds was introduced in [128], which gives a criterion for discarding bonds without making any errors. We consider a triangle formed by three clusters on vertices and three bonds on edges at a given step of the RG. If the three log-fields and the three log-bonds associated with this triangle are $\{\theta_1, \theta_2, \theta_3\}$, $\{\kappa_{12}, \kappa_{23}, \kappa_{13}\}$ respectively, and one of the log-bond, say κ_{12}, satisfies the inequality

$$\kappa_{12} < \min\left(\kappa_{23},\ \kappa_{13},\ \kappa_{23} + \kappa_{13} - \theta_3\right)\ , \tag{5.6}$$

the log-bond κ_{12} can be discarded without affecting the final result of the RG.

The arguments for using (5.6) as the condition for discarding a bond are given as follows: Let us focus on the part of the lattice that involves the log-bond κ_{12} as shown in Fig. 5.2 without loss of generality, and assume that κ_{12} satisfies the condition (5.6) only within the triangle formed by the vertices 1, 2, and 3, but not within the triangle formed by 1, 2 and 4, i.e. $\kappa_{12} \geq \max\left(\kappa_{24},\ \kappa_{14},\ \kappa_{24} + \kappa_{14} - \theta_4\right)$. There are some decimation processes that will involve κ_{12} if κ_{12} is not discarded:

1. The log-field θ_3 is the one to be decimated, then a renormalized log-field $\widetilde{\kappa}_{12} = \kappa_{13} + \kappa_{23} - \theta_3$ is generated. Since κ_{12} obeys the inequality (5.6), we have $\widetilde{\kappa_{12}} > \kappa_{12}$. During the RG, we always use the transform (5.4) to keep the stronger bond, and in

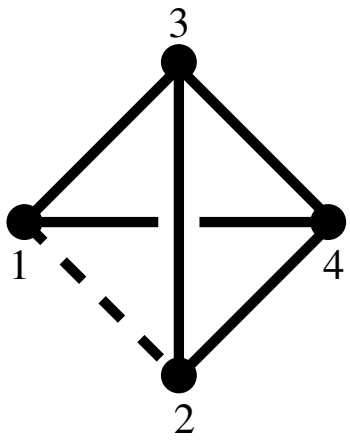

Figure 5.2: The log-bond κ_{12} satisfies the inequality (5.6), and can be discarded without affecting the final result of the RG.

this case, it is $\widetilde{\kappa}_{12}$ to be kept. Thus discarding κ_{12} does not affect the result of the decimation process.

2. The log-field θ_1 is the strongest coupling that is going to be decimated. A new log-bond connecting 2 and 3 with a strength $\widetilde{\kappa}_{23} = \kappa_{12} + \kappa_{13} - \theta_1$, which involves the discarded log-bond κ_{12}, is generated. $\widetilde{\kappa}_{23}$ should be compared with the bond κ_{23}, which was already present, and only the stronger one will be kept. Since $\theta_1 > \kappa_{13}$, we have $\kappa_{23} - \widetilde{\kappa}_{23} > \kappa_{23} - \kappa_{12} > 0$, where the last inequality is valid because of the condition for discarding κ_{12}. Thus, κ_{23} will be kept, and the discarded log-bond κ_{12} does not play any role in this decimation process. The same argument can be used for the case that θ_2 is to be decimated.

3. If the log-bond κ_{13} (or κ_{23}) is the strongest bond that is to be decimated, then a log-bond $\widetilde{\kappa}_{12} = \kappa_{13}$ $(= \kappa_{23})$ between 1 and 2 will be generated. This new bond is larger than κ_{12}, so discarding κ_{12} before the decimation process is legitimate.

4. If the log-bond κ_{24} is to be decimated, then the clusters on sites 2 and 4 join together. This will leave a renormalized log-field $\widetilde{\theta}_2 \equiv \widetilde{\theta}_{(24)} < \theta_2$ and two new bonds $\widetilde{\kappa_{12}} = \max(\kappa_{12}, \kappa_{14}) = \kappa_{12}$, $\widetilde{\kappa}_{23} = \max(\kappa_{23}, \kappa_{34}) \geq \kappa_{23}$. The remaining triangle consisting of $\left\{\theta_1, \widetilde{\theta}_2, \theta_3\right\}$ and $\{\kappa_{12}, \widetilde{\kappa}_{23}, \kappa_{13}\}$ will collapse if one of the fields or bonds is decimated. Using the arguments 1-3, we can see that discarding κ_{12} does not affect the process. Similarly, the decimation process occurring due to the strongest log-bond κ_{34} results in a triangle formed by $\left\{\theta_1, \theta_2, \widetilde{\theta}_3\right\}$ and $\{\kappa_{12}, \widetilde{\kappa}_{23}, \kappa_{13}\}$ with $\widetilde{\theta}_3 \equiv \theta_{(34)} = \theta_3 + \theta_4 - \kappa_{34} < \theta_3$ and $\widetilde{\kappa}_{23} = \max(\kappa_{23}, \kappa_{24}) \geq \kappa_{23}$. Again, the arguments given above can be applied to this case.

In all above-mentioned cases, which do not lose the generality, discarding a bond with a strength that satisfies the inequality (5.6) does not affect the result of the RG. In our numerical implementation, apart from solving the memory problem, we could reduce the

CPU time the simulation needed for a large system, such as a system of size 64×64, by about 10% by using the criterion given in (5.6) to discard weak bonds.

To study the critical behavior of the random transverse Ising model, the objects of interest in the RG are the surviving clusters at a given energy scale. The basic relationship between the energy scale Ω and the length scale L, which corresponds to spacing of the clusters, is $\Omega \sim L^{-z}$, defining the dynamical exponent z. At an infinite-randomness fixed point, the dynamical exponent is infinite, $z \to \infty$, and the scaling is very different: $\Gamma \equiv \ln(\Omega_0/\Omega) \sim L^{\psi}$ with $\psi < 1$, where Ω_0 sets the energy scale of the original Hamiltonian. The magnetic properties of the system are determined by the magnetic moments μ of the surviving clusters, i.e. the number of strongly correlated spins in it; at criticality $\mu \sim \Gamma^{\phi}$ with some new exponent ϕ. Moving away from the critical point by a distance $|\delta|$, the linear size $\sim \xi$ of such a cluster scales as $\xi \sim |\delta|^{-\nu}$, defining the correlation length exponent ν. The above-mentioned critical exponents ψ, ϕ and ν can fully characterized the scaling properties at an infinite-randomness fixed point, as we have pointed out in Sec. 1.5. In our numerics we run the RG for each sample until there is only one cluster remaining, and simply measure the transverse field and the moment of this cluster without keeping trace of them during the RG. From the properties of this last surviving cluster, we can determine the dynamical exponent and the basic critical exponents.

5.2 The one-dimensional model

The RG can be carried out analytically in one space dimension, therefore we can use the $1d$ case with periodic boundary conditions as a simple check for our numerical implementation. The critical point for a chain with the initial distributions given in (5.1) and (5.2) is located at $h_0 = 1$ where the distributions of bond and fields are equal. The distance δ from the critical point is conveniently given by (4.18), for this case $\delta = \frac{1}{2} \ln h_0$.

In Fig. 5.3(a) we show the probability distribution of the logarithm of the last remaining cluster field $\tilde{h}_{\infty}$, at the critical point $h_0 = 1$. The distribution gets broader on a logarithmic scale with increasing system size, indicating an infinite dynamical exponent $z = \infty$. The data scale, according to Fig. 5.3(b), like $L^{-1/2}$, where L is the system size. From this one concludes that the exponent ψ defined in (1.13), is given by $\psi = 1/2$, which is the exact analytical value.

Inspecting the number of spins in the last remaining cluster, which is proportional to the magnetic moment per cluster μ, at the critical point, we obtain the size dependence $\mu = [\mu]_{\rm av} \sim L^{\phi\psi} \sim L^{0.81}$ from Fig. 5.4, and thus $\phi \approx 1.62$, from which the scaling dimension of the bulk magnetization follows as $x_m = 1 - \phi\psi \approx 0.19$. We repeated the calculation for the average magnetization $m = [\mu/L]_{\rm av}$ away from the critical point. As shown in Fig. 5.5, we obtain a very good data collapse in terms of the scaling variables mL^{x_m} and $L^{1/\nu}\delta$ with $x_m = 0.19$ and the exact correlation length exponent $\nu = 2$.

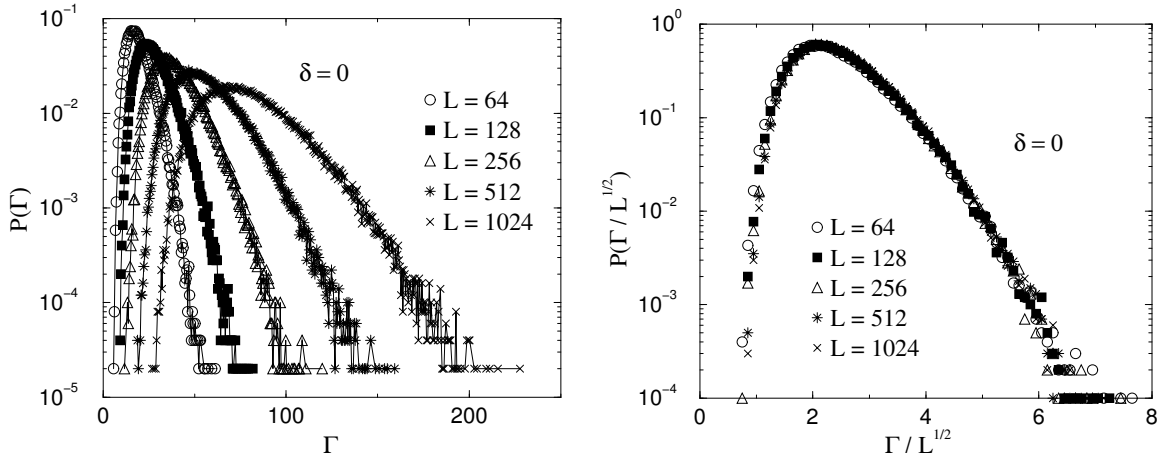

(a) (b)

Figure 5.3: (a): Distribution of the logarithmic strength of the last remaining cluster fields, $\Gamma \equiv \ln(\Omega_0/\tilde{h}_\infty)$ (Ω_0 denotes the energy scale of the original Hamiltonian). The distribution gets broader on a logarithmic scale with increasing system size, indicating a infinite dynamical exponent z. The data are obtained from $100\,000$ samples for each system size. (b): A scaling plot of the data in (a). The data collapse very well with the scaling variable $\Gamma/L^{1/2}$, in agreement with the prediction.

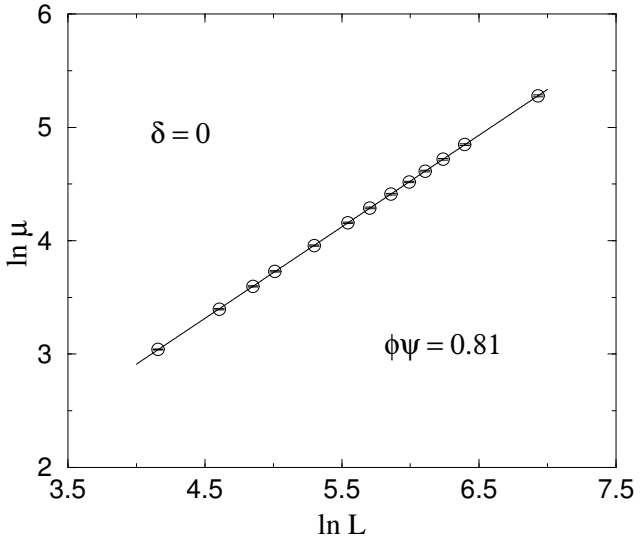

Figure 5.4: Scaling of the number of active spins (proportional to average magnetic moment, μ) in the last remaining spin cluster at the critical point. We find $\mu \sim L^{0.81}$, implying $\phi \approx 1.62$. This is consistent with the analytical prediction, $\phi = \frac{1+\sqrt{5}}{2}$. The data are an average over $100\,000$ samples.

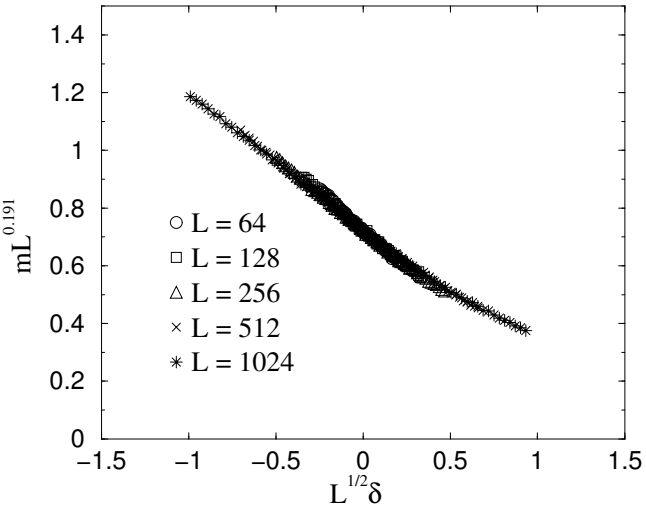

Figure 5.5: Scaling plot of the average bulk magnetization near criticality for different system sizes in terms of the scaling variables mL^{x_m} and $L^{1/\nu}\delta$, assuming $x_m = 0.191$ and $\nu = 2$.

In the disordered phase $h_0 > 1$, almost all the effective transverse fields will be much stronger than almost all the effective bonds at low energy. Thus, in the decimation procedure, it is more likely that a cluster gets decimated. The clusters surviving to low ener-

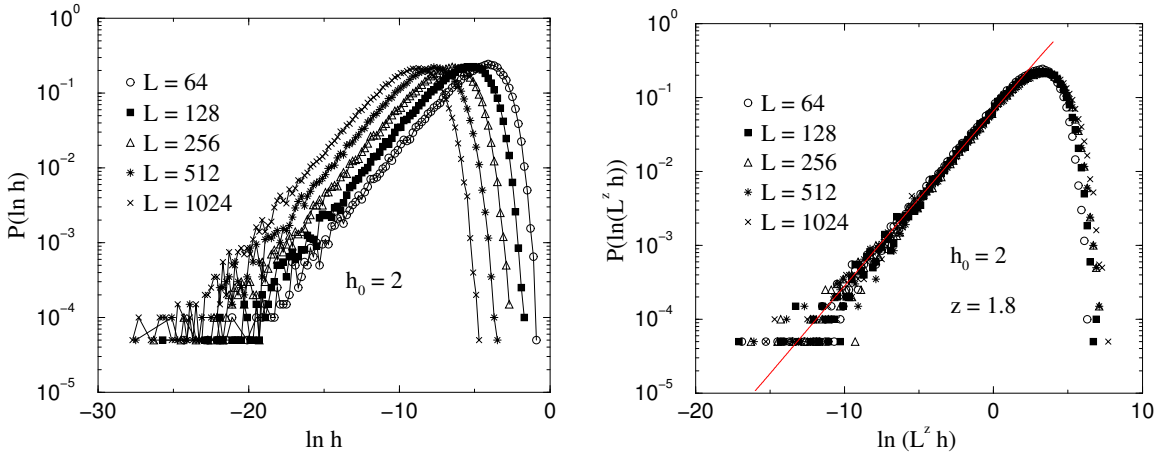

(a) (b)

Figure 5.6: (a): Distribution of logarithmic effective fields $\ln \tilde{h}_\infty$ of the last spin cluster in the disordered phase at $h_0 = 2$. The curves for different sizes look very similar but shifted horizontally related to each other. (b): Scaling plot of the data in the left figure (a). The dynamical exponent $z(h_0)$ is obtained from the the slope of the asymptotic form given in (5.7). The fit here has $z(h_0 = 2) \approx 1.8$.

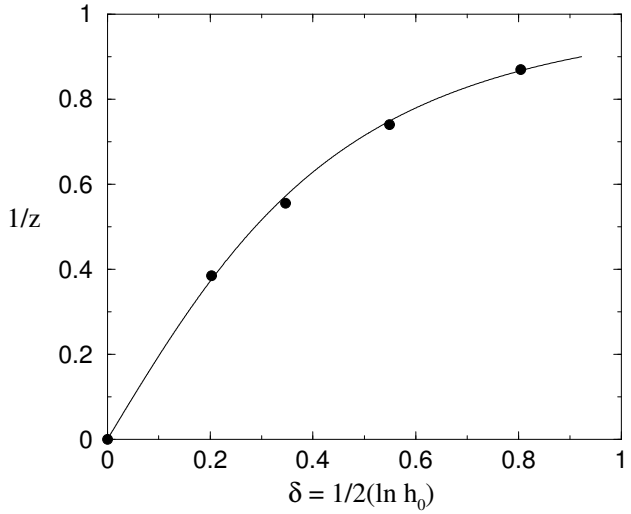

Figure 5.7: The value of $1/z(\delta)$ for $d = 1$ obtained from the probability distribution of logarithmic effective fields of the last remaining clusters in the Griffiths-McCoy region. The solid line, which fits well, is a plot of the exact $z(\delta)$-relation given in (5.8).

gies are rare large strongly coupled ferromagnetic regions that exist even in the disordered phase. The field distribution of these clusters does not broaden any more, but tends to the form [49, 115, 126]:

$$\rho(\tilde{h})\mathrm{d}\tilde{h} \approx \frac{1}{z}\left(\frac{\tilde{h}}{\Omega}\right)^{-1+1/z}\frac{\mathrm{d}\tilde{h}}{\Omega}$$

with a finite width in the limit of low energy (Fig. 5.6(a)). This gives rise to a Griffiths-McCoy phase with continuously variable dynamical exponent z that relates the scales of energy and length—the typical fields and spacing of surviving clusters—via $\Omega \sim L^{-z}$. The most convenient way to determine to determine z is via the distribution of the log-fields of the last remaining cluster, which has an asymptotic form [53]:

$$\ln[P(\ln \tilde{h}_\infty)] = \frac{1}{z}\ln \tilde{h}_\infty + \text{const}\ . \tag{5.7}$$

From the asymptotic slope of the distribution, we obtained $z(\delta)$ in the disordered Griffiths-McCoy phase (Fig. 5.6(b)). Fig. 5.7 shows the results for $1/z(\delta)$ against δ. As we can see, the data agree excellently with the exact relation [88]:

$$z\ln(1 - z^{-2}) = -2\delta\ , \tag{5.8}$$

as argued by Iglói et al. that the RG method is asymptotically exact in the low-energy limit in the whole Griffiths-McCoy phase for one-dimensional case. In the ordered phase $h_0 < 1$, the distribution of fields and bonds are related to the distribution in the disordered phase $h_0 > 1$ via duality. This can be seen in Fig. 5.8, which shows the distribution of the last remaining log-bond $\ln \tilde{J}_\infty$, and its scaling plot.

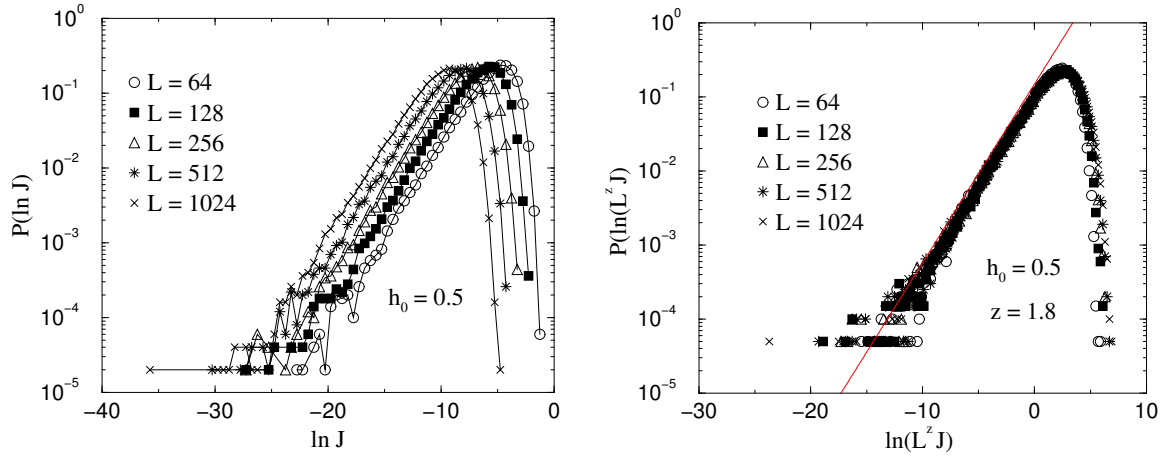

(a) (b)

Figure 5.8: Distribution of the last remaining log-bonds in the ordered phase at $h_0 = 0.5$ for $d = 1$ (a), and its scaling plot (b). One observes that the scaling behavior of bonds in the ordered phase and that of fields in the disordered phase (see Fig. 5.6) are related through duality.

Our code has been tested by verifying that it reproduced the analytical results for one dimension. The simulations were performed on SUN-workstations. The typical computation time for $100\,000$ samples with system size $L = 1024$ was about 5h.

5.3 The double chain

Before presenting our results for the two-dimensional case, we discuss an in-between model—the double chain (Fig. 5.9). The geometry of the double chain is more complicated than the single chain. Unlike the single chain, the action of the RG does not preserve the spatial structure of the double chain, so we should follow the RG scheme for higher dimensions described in Section 5.1. Furthermore, the role of the fields and bonds in the double chain can not be interchanged, therefore the position of the critical point is not known by self-duality.

We first discuss how to locate the critical point. We calculated the average magnetization, $m(L, h_0) \equiv [\mu(L, h_0)/N]_{\text{av}}$, in a finite system of size L (with $N = 2L$ spins) by counting the number of spins μ in the the last surviving cluster under renormalization, and defined a function $g_L(h_0)$ by the ratio:

$$g_L(h_0) \equiv \frac{m(L, h_0)}{m(L/2, h_0)} \ . \tag{5.9}$$

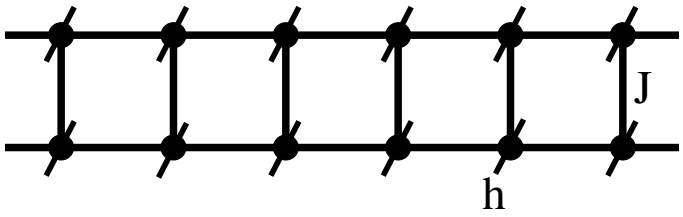

Figure 5.9: The double-chain model used in this section. The RG scheme for this geometry is the same as for two dimensions that is described in Fig. 5.1.

In the ferromagnetic phase $h_0 < h_c$, the average magnetization $m(L \to \infty, h_0)$ in the thermodynamic limit does not depend on L, consequently $\lim_{L\to\infty} g_L(h_0) = 1$. In the paramagnetic phase $h_0 > h_c$, $m(L, h_0)$ is exponentially small in L, thus the function $g_L(h_0)$ has a vanishing value in the $L \to \infty$ limit. In between at the critical point $h_0 = h_c$, where the average magnetization scales as $m(L, h_c) \sim L^{-x_m}$, we have

$$\lim_{L\to\infty} g_L(h_c) = 2^{-x_m} \ ,$$

which is independent of L. Plotting $g_L(h_c)$ vs h_0 for different system sizes L (Fig. 5.10), one can then find the critical point h_c at which all curves intersect. The value of $g_L(h_0)$ at the intersection point is 2^{-x_m}, from which we can estimate the magnetization scaling dimension, x_m. From Fig. 5.10 we obtain $h_c \approx 1.9$ and $x_m \approx 0.19$. Note the magnetization scaling dimension x_m for the double chain is found to be equal to that for the single chain.

Another simple way to locate the critical point is based on the assumption that the ratio of frequencies of the cluster annihilation/aggregation processes becomes stable at the critical

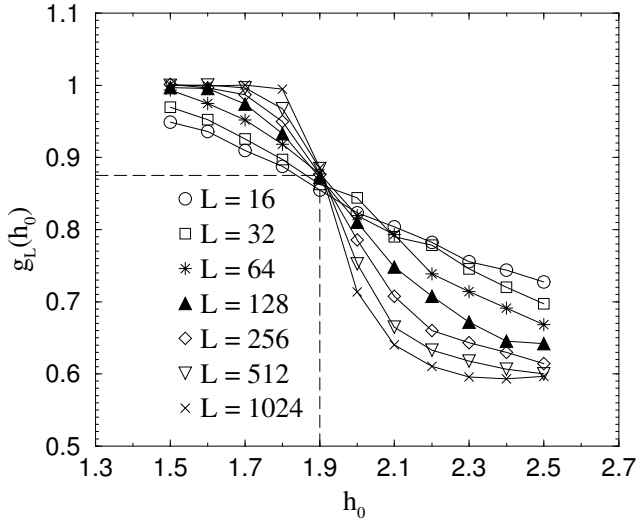

Figure 5.10: The results of ratio of the average magnetization for system sizes L and $L/2$ with $L = 8 \ldots 1024$. We find the intersection at $h_c \approx 1.9$ and the y-value equals roughly 0.875 corresponding to $x_m \approx 0.19$, as for the single chain.

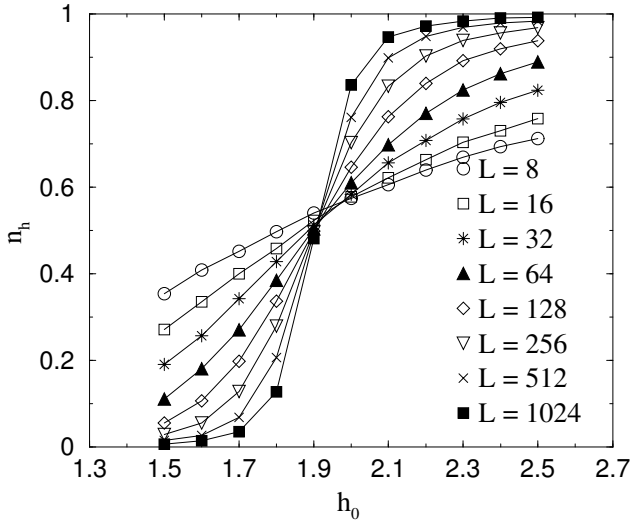

Figure 5.11: The frequency of the annihilation processes, in which a cluster is decimated, for various system sizes L at the final stage of the RG. The critical point occurs when the fields and bonds are balanced by the annihilation and aggregation of clusters, and is found to be near $h_0 = 1.9$ where the intersection is located.

point under the action of the RG [105]. An annihilation process means a decimation step in which the maximum-energy term that is decimated is a transverse field, while in an aggregation process the maximum-energy term corresponds to a bond, as we have defined in Section 4.2.1. Stability of the ratio of the number of these two types of processes is an indication of a balance between the field part of the Hamiltonian and the bond part. We used this assumption and simply counted the number of occurrences of the annihilation processes at the last stage of RG (before a single cluster remaining) for different system sizes L and h_0. We find all curves of the proportion of the annihilation processes in the total samples, n_h, indeed intersect at $h_c \approx 1.9$, as shown in Fig. 5.11. Moreover, the value of n_h at the critical point is 0.5, which means the annihilation and aggregation processes occur with the same frequency. This is obviously for the case of the single chain, where it follows from the self-duality at the critical point. However, the double chain is *not* self-dual.

Now we turn to the distributions of couplings. In the ordered phase, $h_0 < 1.9$, the bonds tend to dominate the fields under renormalization, and in low-energy Ω limit almost all the decimations cause a cluster with a weaker bond to form. As a result, the width of the field distribution grows without limit, while the width of the bond distribution saturates. In the disordered phase $h_0 > 1.9$, in contrast, the fields tend to dominate the bonds at low energies. Thus, the width of the bond distribution grows faster than the field distribution under renormalization. Fig. 5.12 (Fig. 5.13) shows the log-field and log-bond distribution in the ordered (disordered) phase, $h_0 = 1.8$ ($h_0 = 2.0$). We can see the situation described above. At the critical point, where the annihilation and aggregation of clusters compete at all energies [98, 105], the log-field and the log-bond distributions become asymptotically

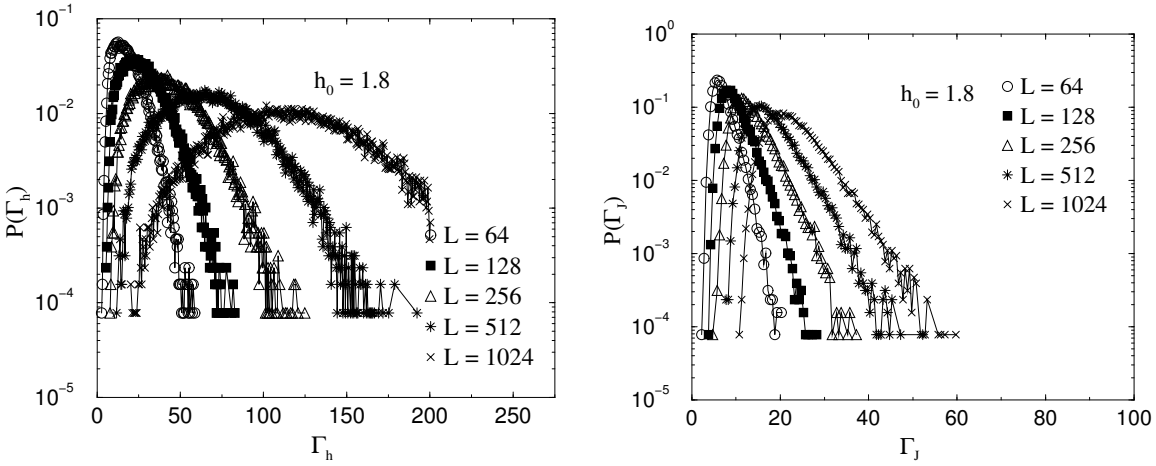

Figure 5.12: The log-field $\Gamma_h = \ln(\Omega_0/\tilde{h}_\infty)$ (left) and log-bond $\Gamma_J = \ln(\Omega_0/\tilde{J}_\infty)$ (right) distributions at the final stage of the RG in the ordered phase ($h_0 = 1.8$). The log-field distribution gets broader with increasing L, while the broadening of the log-bond distribution is not significant.

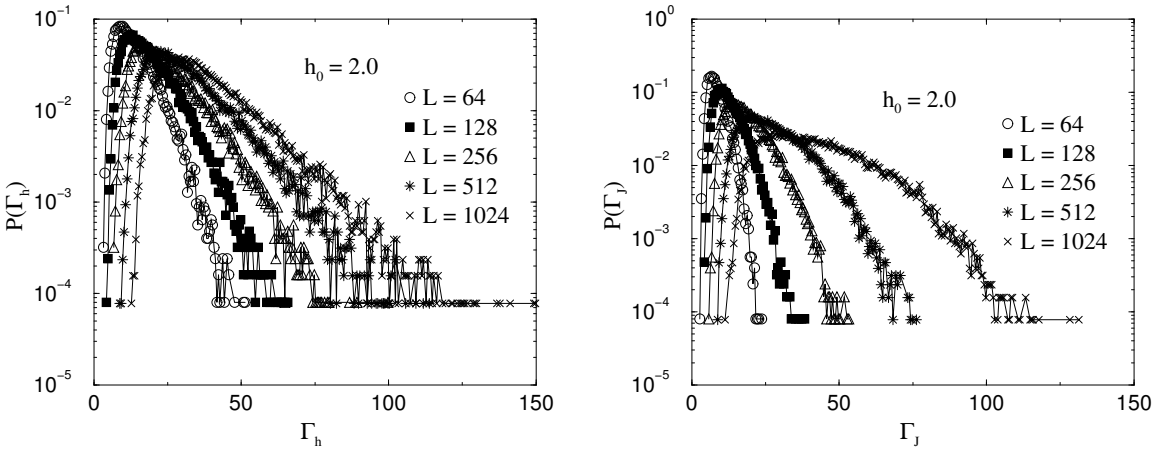

Figure 5.13: A similar plot to Fig. 5.12, but in the ordered phase $h_0 = 2$. In contrast to the disordered phase, here the broadening of the log-field Γ_h distribution (left) appears to be saturating, while the width of the log-bond Γ_J distribution grows rapidly with increasing L.

in the same form (Fig. 5.14), as in the single chain. Furthermore, the scaling of the critical distributions yields the critical exponent $\psi = 0.5$ (Fig. 5.15). From the magnetization scaling dimension $x_m = d - \psi\phi \approx 0.19$, we have for this quasi-one-dimensional ($d = 1$) double chain $\phi \approx 0.81$. The exponents ψ and ϕ are exactly the same as for the simple chain, which implies that the double chain and the simple chain may belong to the same universality class.

To determine another basic critical exponent—the correlation length critical exponent ν, we calculated the average magnetization m slightly away from the estimated exponent

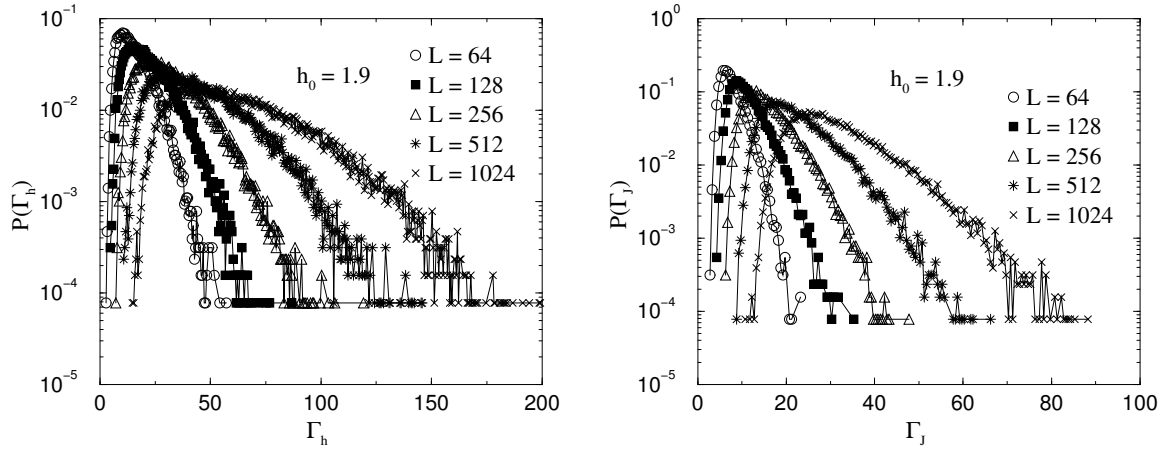

Figure 5.14: The log-field (left) and log-bond (right) distributions become asymptotically identical at the estimated critical point $h_0 = 1.9$, except for a constant multiplicative factor that reflects the short-ranged non-universal physics.

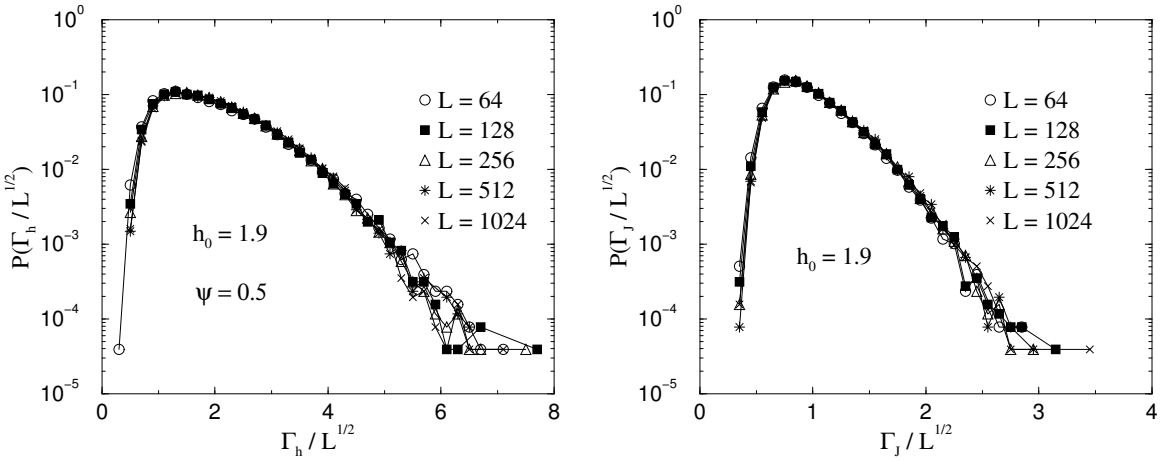

Figure 5.15: Scaling plots of the distribution of log-fields (left) and of log-bonds (right) for the double chain at the critical point $h_c = 1.9$. The data scales quite well with the same form $\Gamma_{h(J)} \sim \sqrt{L}$ as in $1d$.

$h_0 = 1.9$. From the finite-size scaling $m = L^{-x_m}\widetilde{m}(\delta L^{1/\nu})$ and $x_m \simeq 0.19$ that we obtained from $g_L(h_0)$, we have $\nu = 2$ (Fig. 5.16), which is indeed the same as the simple chain.

In the Griffiths-McCoy phase $h_0 > h_c = 1.9$, we extracted the dynamical exponent $z(h_0)$ from the distribution of the last log-fields $P(\ln \tilde{h}_\infty)$ (Fig. 5.17(a)), which corresponds to the distribution of log-gaps, $P(\ln \varepsilon)$, and obeys $\ln[P(\ln \varepsilon)] = 1/z \ \ln \varepsilon + \text{const}$. The results of the dynamical exponent as a function of h_0 is depicted in Fig. 5.17(b).

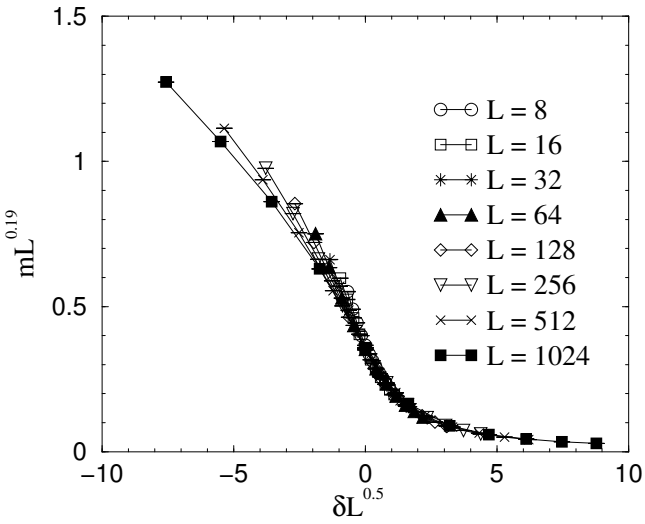

Figure 5.16: Finite-size scaling plot of the magnetization for the double chains, assuming $h_c = 1.9$, $\nu = 2$, and $x_m = \beta_b/\nu = 0.19$.

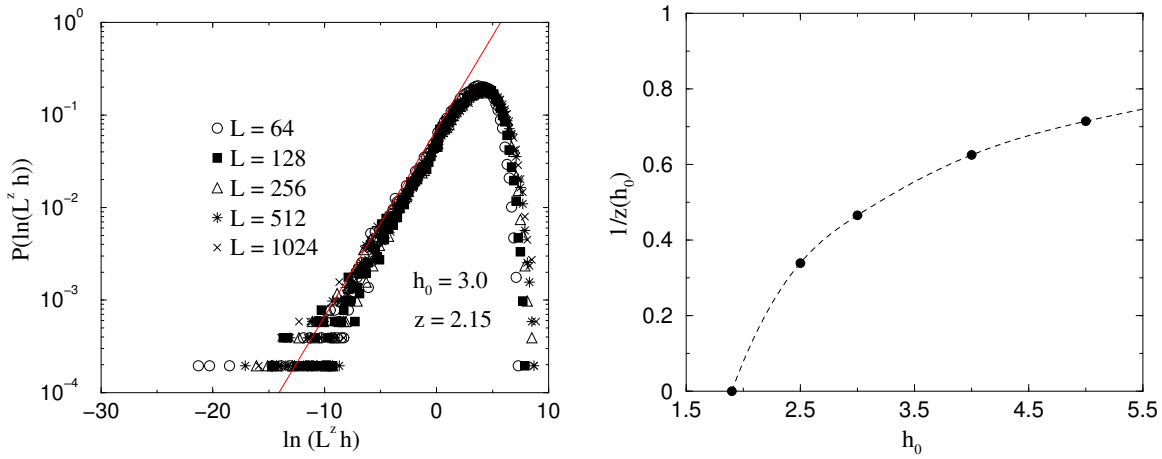

(a) (b)

Figure 5.17: (a): A scaling plot of the log-field distribution at $h_0 = 3$, assuming scaling with a finite value $z = 2.15$. The slope of the straight line corresponds to $1/z$. (b): The estimates for $1/z$ against h_0 for the double chain.

5.4 The square lattice

In this section we will present our results for the two-dimensional case with periodic boundary conditions. we simulated up to $N \equiv L \times L = 128 \times 128$ spins and run up to 10240 samples for each initial probability distribution according to (5.1) and (5.2). Under renormalization many weak bonds are generated that, for larger lattices, cannot all be stored. To solve this problem, we used the criterion (5.6) to discard the weak bonds, which has been tested by verifying that it did not alter the results obtained from simulations with all bonds being kept. A simulation on systems of size 128×128 with 2560 samples could be done within 4h with 256 processors on the Cray T3E.

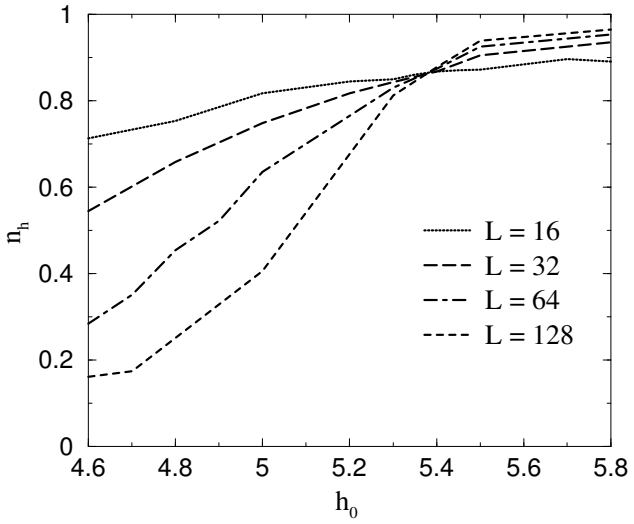

Figure 5.18: The frequency of the annihilation processes for various system sizes L at the final stage of the RG. The critical point occurs when the fields and bonds are balanced by the annihilation and aggregation of clusters. From the position of the intersection we estimate $h_c \approx 5.4$.

To locate the critical point, we followed the methods discussed in the previous section for the double chain. We can estimate the position of critical point by counting the number of occurrences of the annihilation/aggregation process as the RG runs or at the last stage of the RG. Fig. 5.18 shows the frequency of the annihilation processes at the last stage of the RG against h_0. We find the intersection near $h_0 = 5.4$, where the critical point should be located. Since we made approximation (5.3) during the action of the RG, we do not expect that the critical point—a non-universal parameter—estimated by the RG should be identical to that obtained from the Monte-Carlo simulations.

The critical point can also be determined by the finite-size behavior of the average magnetization $m(L, h_0)$. As discussed in the previous Section 5.3, in the thermodynamic limit the ratio $g_L(h_0) = m(L, h_0)/m(L/2, h_0)$ has a non-vanishing and L-independent value, corresponding to, 2^{-x_m}, at the critical point, where x_m is the magnetization scaling dimen-

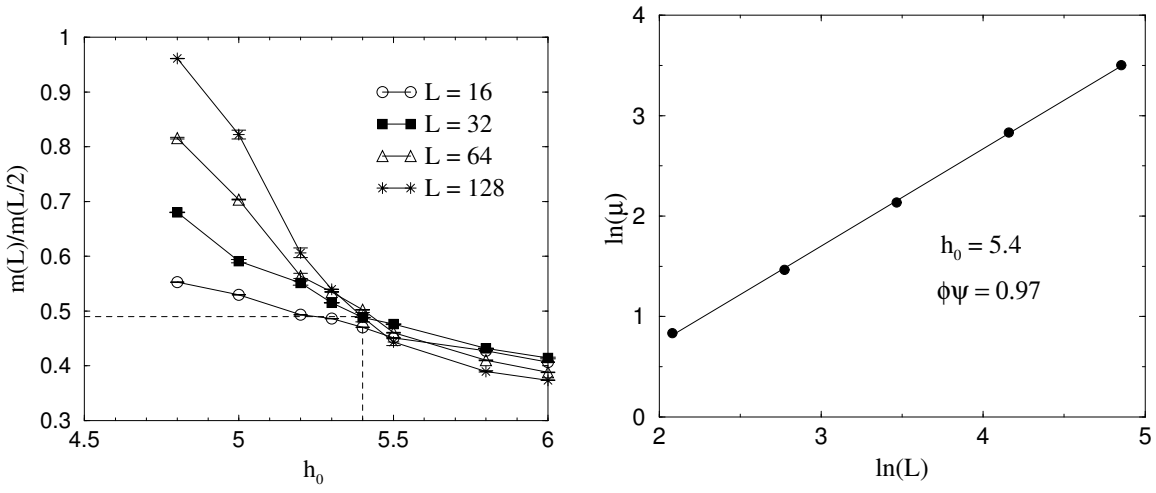

(a) (b)

Figure 5.19: (a): Finite-size estimates of the critical point for $2d$. For different pairs $(L, L/2)$, all curves of the ratio of the average magnetization $g_L(h_0) = m(L)/m(L/2)$ intersect at the critical point $h_c \approx 5.4$. The y-value of g_L at h_c equals roughly 0.49 corresponding to $x_m \approx 1.03$. (b): Average critical cluster moment as a function of L in log-log plot. The slop of the line corresponds to $\phi\psi \approx 0.97$, which is consistent with the result of $x_m = 2 - \phi\psi$.

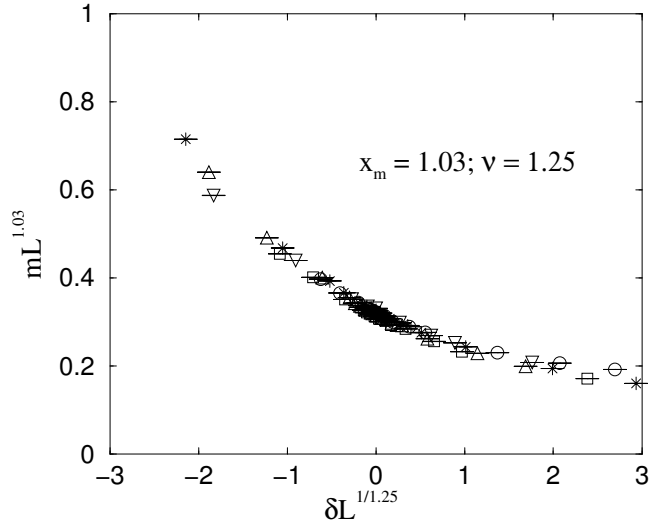

Figure 5.20: Finite-size scaling plot of the average magnetization, assuming $x_m = \beta_b/\nu = d - \psi\phi = 1.03$ and $\nu = 1.25$.

sion. From plotting our data of $g_L(h_0)$ for different system sizes L (Fig. 5.19(a)), we find the intersection—the critical point—at $h_0 = 5.4 \pm 0.1$, which agrees with the previous

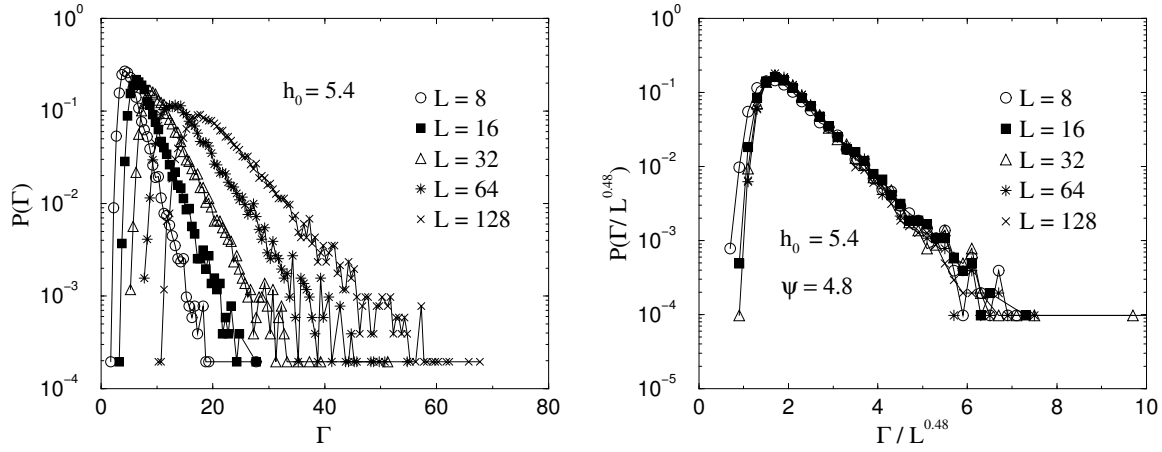

(a) (b)

Figure 5.21: (a): The log-field $\ln \tilde{h}_\infty$ distribution of the last remaining clusters at the estimated critical point $h_0 = 5.4$ for $2d$. (b): Scaling plot of the data in the left figure, assuming $\psi = 0.48$.

measurement by counting the number of annihilation processes. From the value at the intersection point, 2^{-x_m}, we conclude $x_m \approx 1.03$, yielding $\psi\phi = d - x_m \approx 0.97$. We can also fit more directly for $\psi\phi$ using the finite-size scaling of the average cluster moment—the number of spins in the last surviving cluster—at the critical point: $\mu \sim L^{\psi\phi}$, obtaining the same estimate $\psi\phi \approx 0.97$ (Fig. 5.19(b)).

From a study of the finite-size scaling of the average magnetization near the critical point, $m = L^{-x_m}\widetilde{m}(\delta L^{1/\nu})$, as shown in Fig. 5.20, we obtain for the best data collapse the exponent $\nu \approx 1.25$ related to the correlation length $\xi \sim |\delta|^{-\nu}$. This is close to the value obtained from the Monte Carlo simulations $\nu \approx 1.33$.

To estimate the exponent ψ, we consider the critical distribution of the log-energy scale set by the last surviving log-field $\ln \tilde{h}_\infty$ under renormalization. The width of the distribution $P(\Gamma) \equiv P(-\ln \tilde{h}_\infty)$ shown in Fig. 5.21(a) grows with increasing L, which indicates that it is at infinite randomness. For an infinite-randomness fixed point, the dynamical exponent is infinite, $z \to \infty$, and the log-energy distribution should be a function of the scaling variable Γ/L^ψ. From the rescaled log-field distribution (Fig. 5.21(b)), we obtain $\psi \approx 0.48$, which is close to the value for one-dimensional single and double chains, and not inconsistent with the result obtained from our Monte Carlo simulations ($\psi \approx 0.58 - 0.6$). This exponent combining with the magnetization scaling dimension $x_m = d - \psi\phi$ gives $\phi \approx 2.02$.

In the disordered phase $h_0 > 5.4$, the field distribution has finite width in the limit of low energy. As in one dimension, this gives rise to Griffiths-McCoy singularities. We observe that the log-field distribution tends to an exponential form $\sim e^{-c(\delta)\ln \tilde{h}}$. This reminds us of the power-law density of low-energy excitations, $\rho(\varepsilon) \sim \varepsilon^{-1+d/z(\delta)}$, with a conti-

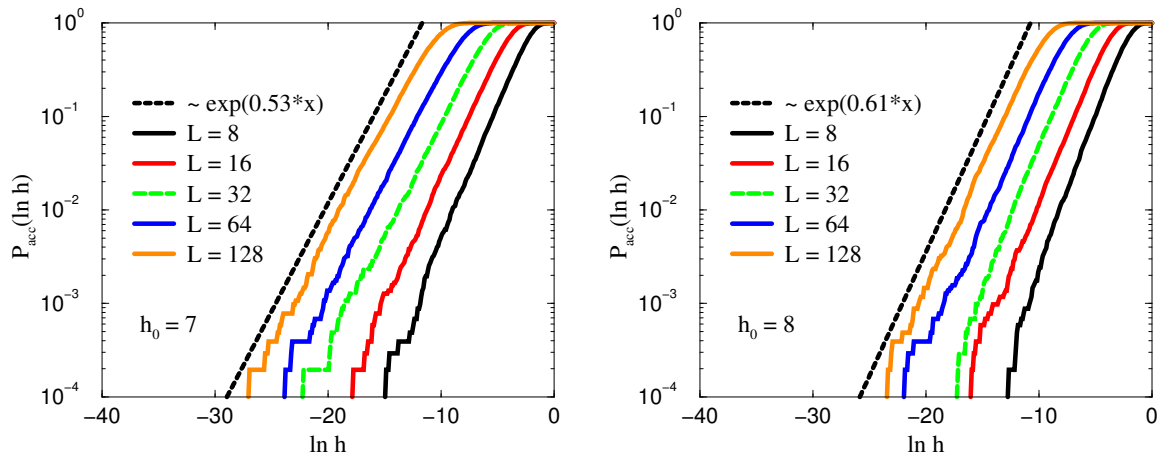

Figure 5.22: Accumulated histogram of the log-field of the last remaining cluster for $h_0 = 7$ (left) and for $h_0 = 8$ (right). We obtain the dynamical exponents $z(h_0 = 7) \approx 2/0.53 \approx 3.77$ and $z(h_0 = 8) \approx 2/0.61 \approx 3.28$ from the slopes of the long-dashed lines.

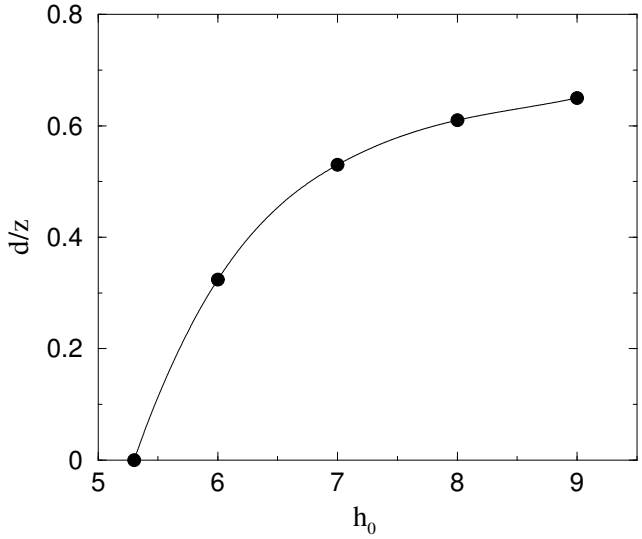

Figure 5.23: A plot of d/z for $d = 2$ versus h_0. The line is just a guide to the eye.

nously varying dynamical exponent $z(\delta)$ in the Griffiths-McCoy phase, which we have discussed in Subsec. 1.4.1. Indeed, the clusters that contribute to these fields at low energies correspond to strongly coupled ordered clusters with a small energy gap $\sim \tilde{h}$. In a spatial volume L^d, we assume that the probability of the gaps is proportional to L^d, thus $P_L(\ln \varepsilon) \sim L^d \varepsilon^{d/z}$ [55]. From the low-energy tail $\sim e^{-(d/z)\ln \tilde{h}_\infty}$ of distribution of the last remaining log-fields, we can then extract the dynamical exponent $z(\delta)$, which characterizes all the Griffiths-McCoy singularities, e.g. the singularity of the local susceptibility at $T \to 0$, $\chi^{\rm loc} \sim T^{-1+d/z(\delta)}$. As seen in Fig. 5.22, the accumulated probability distribution of $\ln \tilde{h}_\infty$ for $h_0 = 7$ ($h_0 = 8$) tends approximately to a straight line on a plot with log y-axis. We estimate $d/z(h_0)$ from the slope, yielding $z(h_0 = 7) \approx 3.77$ ($z(h_0 = 8) \approx 3.28$). In Fig. 5.23 we show our result for $d/z(h_0)$ varying continuously with h_0 from the critical point $h_0 = 5.4$ to $h_0 = 9$: at criticality $z(h_0 = 5.4)$ is infinite, and in the large h_0 limit the singularities get weaker, thus z goes towards 2 $(= d)$.

5.5 Summary and conclusions

We have studied the random transverse-field Ising model in one dimension, in the ladder geometry and in two dimensions by implementing the numerical Ma-Dasgupta-Hu RG technique. For one dimension (the single chain), which is analytically solvable, we have been able to reproduce the analytical results near the fixed point—corresponding to the quantum critical point—and in the disordered Griffiths-McCoy phase. For the double chain (a spin ladder) and two dimensions, we have found that the critical behavior is controlled by an infinite-randomness fixed point, as in one dimension. The physical properties at such an infinite-randomness fixed point are fully characterized by three basic critical exponents ψ, ϕ and ν. We estimated the corresponding critical exponents in the double chain and in two dimensions. From the estimated critical exponents, we conclude that the quasi-one-dimensional double chain belongs to the same universality class as the single chain. Our estimates of the critical exponents for the two-dimensional case are consistent with those from other numerical work, including our Monte Carlo simulations. Table 5.1 gives a summary of the results.

As mentioned earlier, the critical exponents ψ and ϕ are related to the spatial correlation function. We can understand this in the RG picture [37, 49, 87, 105]: Spins which are active (i.e. not decimated) in the same cluster at some energy scale can be regarded as fully correlated, and each pair of them has a correlation of order one since they behave coherently. These pairs of spins are rare, but dominate the average correlation function. As a result, the average correlation function is proportional to the probability of the two spins being active in the same cluster at some energy scale. From the scaling of the average cluster moment $\mu \sim L^{\phi\psi}$, one hence concludes that at criticality the average correlation function falls off as a power law, $C_{\rm av}(r) \sim r^{-\eta}$, with an exponent $\eta = 2(d - \psi\phi)$. In contrast to conventional random critical points, where both typical and average correlations

Table 5.1: A summary of the critical exponents of the random transverse-field Ising model in one and two dimensions. For $1d$, the values are exact. For $2d$, the results are obtained by numerical RG and Monte Carlo (MC) simulations. The exponent η is related to the average correlation function at the critical point via $C_{\rm typ}(r) \sim r^{-\eta}$, and the exponent ψ_c is related to the typical critical correlations via $-\ln C_{\rm typ}(r) \sim r^{\psi_c}$. From the basic critical exponents ψ, ϕ and ν, all bulk exponent can be derived. The values in brackets $(\cdots)$ are obtained from the relations $x_m = d - \psi\phi$, $\eta = 2(d - \psi\phi) = 2x_m$ and $\psi_c = \psi$. The differences in the numerical estimates by RG may be due to different disorder distributions and the truncation procedure used in the RG method.

		ψ	ϕ	ν	x_m	η	ψ_c
$1d$	Ref. [37, 49]	$\frac{1}{2}$	$\frac{1+\sqrt{5}}{2}$	2	$\frac{3-\sqrt{5}}{4}$	$\frac{3-\sqrt{5}}{2}$	$\frac{1}{2}$
$2d$	RG						
	this work	0.48	2.02	1.25	1.03	(2.06)	(0.48)
	Ref. [105]	0.42	2.5	1.07	(1.0)	(2.0)	(0.42)
	Ref. [128]	0.6	1.7	1.25	0.97	(1.94)	(0.6)
	MC						
	this work	0.6	(1.41)	1.33	(1.15)	2.3	0.58
	Ref. [91]	0.42	(2.44)	0.75	(0.975)	1.95	0.33

decay as a power of distance, at an infinite-randomness fixed point the typical critical correlations $C_{\rm typ}(r)$ contributed by spin pairs that are never active in the same cluster falls off as a stretched exponential function of distance. These correlations arise from the first order perturbative effects. When a cluster containing the spin, say σ_i, is decimated at energy scale Ω, the correlation of the spin σ_i with the active spins in the neighboring clusters is, from a perturbative calculation, of order $\tilde{J}/\Omega$, with $\tilde{J}$ the effective bonds that couples the neighboring cluster and the decimated cluster. When one of the neighboring cluster that contains the spin σ_k is decimated at a later scale $\Omega' < \Omega$, the correlation of σ_k to an active spin, say σ_j, in one of the neighboring clusters is of order $\tilde{J}'/\Omega'$. Hence correlations between two spins σ_i and σ_j that are never active in the same cluster is of order $\tilde{J}\tilde{J}'/\Omega\Omega'$. Most spins are correlated at long distances through this way. For spins with large separation r, the smallest of the multiplied perturbative factors that dominates the log-correlations will be of order $e^{-C\Gamma}$ with $\Gamma \sim r^{\psi}$. This yields $-\ln C_{\rm typ}(r) \sim r^{\psi}$.

It is believed that frustration is irrelevant in the infinite-randomness limit since the strongest couplings dominate any weaker couplings in this limit. Thus one expects that the critical points of quantum Ising spin glasses are also governed by the same infinite-randomness fixed point as ferromagnets [98, 105]. However, some recent quantum Monte-Carlo studies of the quantum spin glasses in two and three dimensions had concluded conventional scaling with a finite dynamical exponent at the critical point [42, 43]. This discrepancy may be caused by the rather small size range used there.

As a final note, the distribution functions of the bonds and fields approach a single fixed-

point form for regular initial distributions as we used here. One might think that the fixed-point form of distributions becomes non-universal for some singular initial distributions. We will discuss this topic in the next chapter.

Chapter 6

Random quantum magnets with broad disorder distribution[1]

6.1 Introduction

As indicated in Chapter 4, the critical behavior of the random transverse-field Ising chain is governed by an infinite-randomness fixed point, at which the exact critical exponents are known. Our quantum Monte Carlo simulations (Chapter 3) and numerical renormalization-group (RG) study (Chapter 5) showed that the critical behavior of the random transverse-field Ising model in two dimensions is controlled by an infinite-randomness fixed point, as in the one-dimensional case. So far we have restricted disorder distributions to the regular case. One important question concerning the critical behavior of random quantum systems is the domain of attraction of the infinite-randomness fixed point for different types of disorder distributions, including broad disorder distributions that are highly singular.

The critical properties of the one-dimensional random transverse-field Ising model can be conveniently studied through a mapping to a random walk (RW) problem [84] and a similar procedure works also for the random XX- and XY-models [106]. Using the analogy with the RW problem it is generally expected that the critical exponents of random quantum systems are universal, provided the disorder is (i) spatially homogeneous, (ii) not correlated, and (iii) not broadly distributed. Problems related to the first two conditions, i.e. the effect of inhomogeneous or correlated disorder have already been studied in [94] and [101], respectively. In both cases the critical properties for strong enough perturbations are modified: they are governed by a line of infinite-randomness fixed points, so that the critical exponents are continuously varying functions of the inhomogeneity/correlation parameters.

In this chapter we release the third type of restriction and study the effect of broad disorder distributions on the critical properties of random quantum magnets. We note that the RG

[1] From [114].

analysis done by Fisher [37, 41, 49], which we discussed in Chapter 4, excludes such type of initial disorder. We consider the random transverse-Ising model with the Hamiltonian

$$\mathcal{H} = -\sum_{<i,j>} J_{ij}\sigma_i^x\sigma_j^x - \sum_i h_i\sigma_i^z \tag{6.1}$$

and keep in mind that at the infinite-randomness fixed point it is the logarithm of the bonds J_{ij} and the transverse fields h_i which follows a smooth probability distribution [37, 49]. Therefore we use a parameterization

$$\begin{aligned} J_{ij} &= \Lambda^{\Theta_{ij}} \\ h_i &= h_0 \,. \end{aligned} \tag{6.2}$$

where the exponents Θ_{ij} are independent random variables. They are taken from a broad distribution, $\pi(\Theta)$, such that for large arguments they decrease as $\pi(\Theta) \sim |\Theta|^{-1-\alpha}$. We consider the region $\alpha > 1$, where the κth moment of the distribution exists for $\kappa < \alpha$. This type of distribution, which comes for in different domains of physics and science [67] is usually called *Lévy flight* or *Riemann walk* in the discrete version. The parameter α is the Lévy index. Throughout this chapter we use the following distribution:

$$\pi(\Theta) = \begin{cases} p\alpha(1+\Theta)^{-1-\alpha} & \text{for } \Theta > 0 \\ q\alpha(1+|\Theta|)^{-1-\alpha} & \text{for } \Theta < 0 \,, \end{cases} \tag{6.3}$$

with $p+q = 1$. We also use the discretize version (Riemann walk) of the above distribution, in which $\Theta_i = \pm 1, \pm 2, \cdots$ and the normalization α is replaced by $\zeta(1+\alpha) - 1$, where $\zeta(x)$ denotes the Weierstrass zeta function. We define the deviation from the critical point in the one-dimensional case by

$$\delta = [\ln h]_{\text{av}} - [\ln J]_{\text{av}} \;, \tag{6.4}$$

which is zero at criticality because of duality. For the distributions (6.2) and (6.3), this quantum control parameter is given by

$$\delta = \ln h_0 - (p-q)\ln\Lambda/(\alpha-1) \,.$$

In the following sections, we will investigate the one-dimensional problem analytically by using a mapping to surviving Riemann walks (Subsec. 6.2.1), and study it numerically by Ma-Dasgupta-Hu (MDH) RG approach (Subsec. 6.2.2); We will also present our results for the two-dimensional problem obtained from numerical implementation of the RG procedure (Sec. 6.3). Some details about persistence properties of Lévy flights are presented in the Appendix.

Table 6.1: Critical exponents of the random transverse-field Ising model in one dimension for normal disorder and for the Lévy distribution $(1 < \alpha < 2)$.

	ψ	ϕ	ν	x_m	x_m^s
normal	$1/2$	$\frac{1+\sqrt{5}}{2}$	2	$\frac{3-\sqrt{5}}{4}$	1/2
Lévy	$1/\alpha$		$\alpha/(\alpha-1)$		1/2

6.2 The one-dimensional problem

6.2.1 Exact results through a mapping to random walks

The critical properties of the one-dimensional random transverse-field Ising model have been successfully studied through a mapping to a RW problem [84]. The method, which has been used for inhomogeneous [94] and correlated disorder [101], is based on an exact expression of the surface magnetization of the transverse-field Ising model with L sites [24, 84]:

$$m_s(L) = \left[1 + \sum_{l=1}^{L-1} \prod_{j=1}^{l} \left(\frac{h_j}{J_j}\right)^2\right]^{-1/2} , \tag{6.5}$$

where the last spin of the chain at $l = L$ is fixed to the state $|\sigma_L^x\rangle = |\uparrow\rangle$. Before analyzing (6.5) we cite another simple relation [84, 79], in which the lowest excitation energy $\varepsilon(L)$ in a finite system with open boundary conditions is asymptotically related to the surface magnetization in (6.5):

$$\varepsilon(L) \sim m_s(L)\overline{m}_s(L)h_L \prod_{i=1}^{L-1} \frac{h_i}{J_i} , \tag{6.6}$$

provided $\varepsilon(L)$ vanishes faster than L^{-1}. Here $\overline{m}_s(L)$ denotes the finite-size surface magnetization at the other end of the chain and follows from the substitution $h_j/J_j \leftrightarrow h_{L-j}/J_{L-j}$ in (6.5).

Now we start to analyze the expression in (6.5) and look for the possible values of $m_s(L)$ using the discrete version of the distribution, $\pi(\Theta)$, fixed $h_0 = 1$ and taking the limit $\Lambda \to \infty$. It is easy to see that for this extreme distribution the products in (6.5), $\prod_{j=1}^{l}(h_j/J_j)^2$, take three different values: zero, one or infinity, and for a given sample m_s is zero, whenever any of the products is infinite, otherwise $m_s(L) = \mathcal{O}(1)$. To calculate the *average* surface magnetization one should collect the samples with $m_s(L) = \mathcal{O}(1)$. Here we use the RW-picture applied in [84] and assign to each disorder configuration a random walk, which starts at $t = 0$ at position $y = 0$ and takes at time $t = i$ a step of length Θ_i with probability $\pi(\Theta_i)$. Then for a disorder configuration with a finite surface magnetization the corresponding RW stays until $t = L$ steps at one side of its starting position,

$y(t) > 0,\ t = 1, 2, \ldots, L$, in other words the RW has surviving character. As a consequence, $[m_s(L)]_{\rm av}$ is proportional to the fraction of surviving RW-s, given by the surviving probability, $P_{\rm surv}(t)$ at $t = L$.

For a symmetric distribution, i.e. with $p = q = 1/2$ the corresponding RW-s have no drift, whereas for the asymmetric case, $p \neq q$, there is an average bias given by $\delta_{\rm w} = p - q$, so that for $\delta_{\rm w} > 0 (< 0)$ the walk is drifted towards (off) the adsorbing wall at $y = 0$. The bias of the RW is proportional to the control-parameter of the random transverse-field Ising model, δ, as defined in (6.4), thus the correspondence between random transverse-field Ising model and RW can be generally formulated as:

$$[m_s(\delta, L]_{\rm av} \sim P_{\rm surv}(\delta_{\rm w}, t)\,|_{t=L}\ , \quad \delta \sim \delta_{\rm w}\ . \tag{6.7}$$

Consequently, from the persistence properties of Lévy flights, which are summarized in the Appendix, one can deduce the singular behavior of the average surface magnetization of the random transverse-field Ising model.

We start with the finite-size behavior at the critical point, $\delta = 0$, which is given with the correspondences in (6.7) and (A.12) by

$$[m_s(0, L)]_{\rm av} \sim L^{-x^s_m}\ , \quad \text{with } {\rm x}^{\rm s}_{\rm m} = \frac{1}{2}\ . \tag{6.8}$$

Thus the anomalous scale dimension of the average surface magnetization x^s_m does not depend on the Lévy index α, and its value is the same as for the normal distribution given in Table 6.1.

In the paramagnetic phase, $\delta > 0$, the corresponding Riemann walk has an average drift towards the adsorbing site, with a surviving probability given by (A.14). Thus the related average surface magnetization of the random transverse-field Ising model has an exponentially decreasing behavior as a function of the scaling variable, $\delta L^{1-1/\alpha}$, which is analogous to that in (A.3). Consequently, the characteristic length-scale in the problem, the average correlation length, ξ, and the quantum control parameter, δ, close to the critical point are related as $\xi \sim |\delta|^{-\nu(\alpha)}$ with an α-dependent exponent:

$$\nu(\alpha) = \frac{\alpha}{\alpha - 1}\ . \tag{6.9}$$

Note that $\nu(\alpha)$ is divergent as $\alpha \to 1^+$, which is a consequence of the fact that the first moment of the Lévy distribution is also divergent in that limit. In the other limiting case, $\alpha \to 2^-$, we recover the result for the normal distribution in Table 6.1.

In the ferromagnetic phase, $\delta < 0$, the corresponding Riemann walk is drifted off the adsorbing site and, as shown in the Appendix, the surviving probability approaches a finite value in the large time limit. Consequently, the average surface magnetization of the random transverse-field Ising model is also finite in the ferromagnetic phase and for a small

$|\delta|$ it behaves, according to (A.15), as:

$$\lim_{L\to\infty}[m_s(\delta,L)]_{\rm av}\sim|\delta|^{\beta_s}\,,\quad\text{with }\beta_s=\frac{\alpha}{2(\alpha-1)}\,. \tag{6.10}$$

Thus the scaling relation, $\beta_s=x_m^s\nu$, is satisfied.

Next, we turn to the scaling behavior of the lowest excitation energy expressed in (6.6). Here we note that in a given sample the existence of a very small gap is accompanied by the presence of local order. Thus in a sample with a low-energy excitation one can find a strongly coupled domain of size l, where the coupling distribution follows a surviving walk character. With $m_s=\mathcal{O}(1)$ and $\overline{m}_s=\mathcal{O}(1)$ in (6.6), we obtain the estimate:

$$\varepsilon\sim\prod_{i=1}^{l-1}\frac{h_i}{J_i}\sim\exp\left(-l_{\rm tr}\overline{\ln(J/h)}\right)\,. \tag{6.11}$$

Here $l_{\rm tr}$ measures the size of transverse fluctuations of the corresponding surviving Lévy flight of length $t=l$ and $\overline{\ln(J/h)}$ denotes an average value. At the critical point, $\delta\sim\delta_{\rm w}=0$, the surviving region of the walk and thus the strongly coupled domain in the random transverse-field Ising model extends over the volume of the sample, $l\sim L$, and from (A.2) we have $l_{\rm tr}\sim L^{1/\alpha}$, so (6.11) can be rewritten as:

$$\ln\varepsilon(L)\sim L^{\psi}\,,\quad\text{with }\psi=1/\alpha\,,\ \delta=0\,. \tag{6.12}$$

The critical exponent ψ is a continuous function of the Lévy index which takes the value $1/2$ for the normal distribution when $\alpha\to2^-$.

In the paramagnetic phase, $\delta>0$, there are still realizations with a small energy gap, the scaling form of which in a finite system of size L, can be estimated in the following way. For a Lévy flight, the probability of a large transverse fluctuation, $l_{\rm tr}$, is given from (A.7) by $p(l_{\rm tr},L)\sim L(l_{\rm tr})^{-(1+\alpha)}$, thus its characteristic size can be estimated as $l_{\rm tr}\sim L^{1/(1+\alpha)}$ from the condition $p(l_{\rm tr},L)=O(1)$. Consequently, the lowest gap has the scaling form:

$$\ln\varepsilon(L)\sim L^{1/(1+\alpha)}\,,\quad\delta>0\,, \tag{6.13}$$

which implies a logarithmically broad gap distribution even in the Griffiths-McCoy phase. This is in contrast to the behavior with the normal distribution, where $l_{\rm tr}\sim\ln L$ [84], and the scaling form of the gap is in a power-law form: $\varepsilon(L)\sim L^{-z}$ with the dynamical exponent z being a continuous function of the quantum control parameter δ.

In the remaining part of this subsection we discuss the probability distribution of the surface magnetization. Let us remind that, at the critical point, the average surface magnetization is determined by the so-called *rare events*, which are samples having $m_s=\mathcal{O}(1)$. However, the typical samples, which are represented by non-surviving random walks, have a

vanishing surface order in the thermodynamic limit. For a large but finite system of size L, m_s is dominated by the largest product $\prod_j (h_j/J_j)$ in (6.5) so that

$$\ln m_s(L) \sim \overline{\varepsilon} \sim -l_{\rm tr} \overline{\ln\left(h/J\right)} \tag{6.14}$$

where $\overline{\varepsilon}(L)$ is the value of the gap in the dual system, i.e. where the fields and the bonds are interchanged, $h_i \leftrightarrow J_i$. Since at the critical point the system is self-dual, we have $\ln m_s(L) \sim L^{\psi}$ from (6.12). Thus, the probability distribution of $\ln m_s$ has the scaling form:

$$P_L(\ln m_s) = \frac{1}{L^{\psi}} \tilde{p}\left(\frac{\ln m_s}{L^{\psi}}\right) \ . \tag{6.15}$$

Assuming that the scaling function behaves as $\tilde{p}(y) \sim |y|^a$ for small $|y|$, then the average magnetization is given by $[m_s]_{\rm av} = 1/L^{\psi} \int dm_s \tilde{p}(\ln m_s/L^{\psi}) \sim L^{-(1+a)\psi}$ with $a = \alpha/2 - 1$. In the paramagnetic phase, $\delta > 0$, close to the critical point, according to (6.14) the typical surface magnetization behaves asymptotically as

$$[\ln m_s(L)]_{\rm av} \sim -L\delta \sim -L/\xi_{\rm typ} \ , \tag{6.16}$$

where the typical correlation length $\xi_{\rm typ}$ diverges at the critical point as:

$$\xi_{\rm typ} \sim |\delta|^{-\nu_{\rm typ}} \ , \quad \text{with } \nu_{\rm typ} = 1 \ . \tag{6.17}$$

Note that the characteristic exponent $\nu_{\rm typ}$ is independent of α, but still satisfies the scaling relation $\nu_{\rm typ} = \nu(1-\psi)$, suggested in [98].

6.2.2 Bulk magnetization: a numerical renormalization group study

The critical behavior of the bulk magnetization of the $1d$ random transverse-field Ising model is not related to the properties of a homogeneous RW, but it can be calculated from the so called average persistence properties of a Sinai walk, i.e. a random walk in a random environment [102]. Here we study x_m for Lévy-type disorder by using the MDH RG-procedure described in Sec 4.2. We start with a large finite ring of size L with random couplings and perform the decimation procedure until the last spin. The last log-field sets the log-energy scale, $\Gamma = -\log(\Omega/\Omega_0)$, which scales as $\Gamma \sim L^{\psi}$ at criticality, and the number of active spins in the last remaining cluster, associated with the typical moment of a cluster, scales as $\mu \sim L^{\phi\psi}$. Repeating the calculation for several realizations of the disorder, the critical exponents can be deduced from the appropriate scaling functions.

The log-energy distribution should be a function of the scaling variable Γ/L^{ψ} for different finite systems. As shown in Fig. 6.1, there is an excellent data collapse using our analytical result $\psi = 1/\alpha$.

Next, we analyze the distribution of the cluster moment μ, which is a function of the scaling variable $\mu/L^{\phi\psi}$, from which the magnetization scaling dimension, x_m, follows

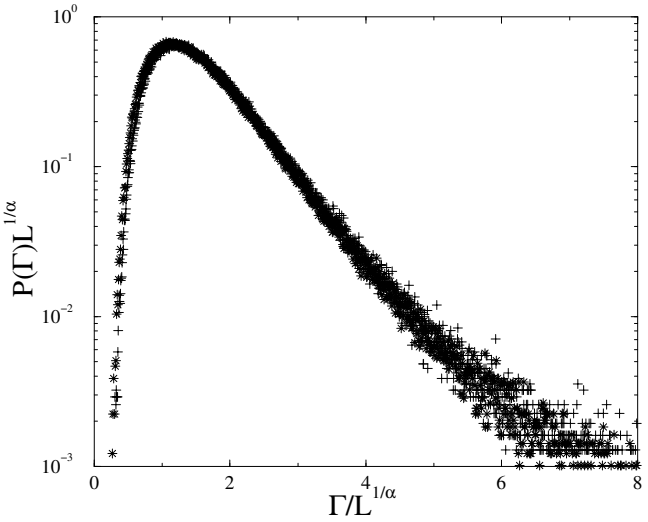

Figure 6.1: Rescaled distribution of the logarithmic energy scale, Γ, for different finite lengths, $L = 32(\diamond), 64(+)$ and $128(*)$ at $\alpha = 1.5$. The best collapse of the data is obtained by the analytical result $\psi = 1/\alpha$.

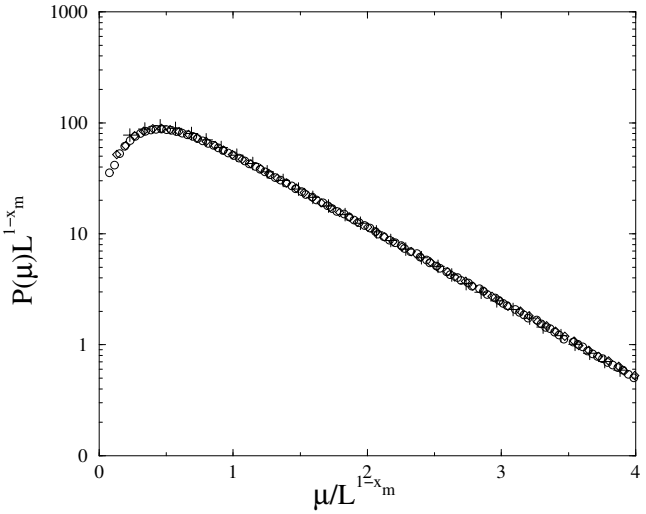

Figure 6.2: Rescaled distribution of the cluster moment for different finite lengths, $L = 32(+), 64(\diamond)$ and $128(\circ)$ at $\alpha = 1.5$. The optimal collapse of the data gives $x_m = 0.22$.

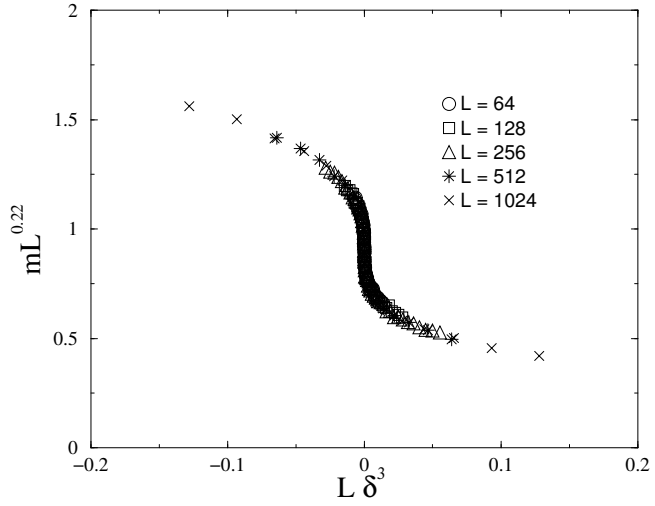

Figure 6.3: Scaling plot of the average bulk magnetization for different finite systems at $\alpha = 1.5$, assuming $x_m = 0.22$ and $\nu = 3$.

through $x_m = d - \phi\psi$. From the optimal data collapse, as presented in Fig. 6.2, we obtain $x_m = 0.22$ for $\alpha = 1.5$, which is definitely larger than that of the system with normal disorder, as given in Table 6.1. Repeating the calculation for the average magnetization, $m(\delta) = [\mu/L]_{\rm av}$, the appropriate scaling variables outside the critical point are mL^{x_m} and $L\delta^{\nu}$. As shown in Fig. 6.3 in terms of the scaled variables we obtain a very good data collapse, using x_m from Fig. 6.2 and the analytical expression in (6.9) for ν.

For a systematic study of the bulk magnetization scaling index we have determined the average critical magnetization for different finite systems and then calculated an effective exponent, $x_m(L)$, by two-point fit comparing $m(L)$ and $m(2L)$. As shown in Fig. 6.4 the effective exponents have a weak size dependence, so that one can have an accurate extrapolated value for $L \to \infty$, which clearly depends on the value of the Lévy index, $1 < \alpha < 2$. These extrapolated magnetization exponents are presented in Fig. 6.4, where for $\alpha > 2$ x_m is expected to be α independent, however the corrections to scaling are strong, especially around the cross-over value $\alpha_c = 2$. At this point we note that in parallel to the random transverse-field Ising model we have also calculated the magnetization scaling dimension of the random quantum Potts chain for $q = 3$.

As can be seen in Fig. 6.4, the extrapolated exponents of the Ising and Potts chains are very probably the same for the same value of the Lévy index α. This result completes the universality of the two models as obtained before analytically for normal disorder [58].

We close this section by a study of the average magnetization in the ferromagnetic phase, $\delta < 0$. As $L \to \infty$, the average magnetization approaches a finite limit, which behaves asymptotically as $m(\delta) \sim |\delta|^{\beta}$ near the critical point. As shown in Fig. 6.5 the results for different finite systems converge to a power-law form, in which the critical exponent β satisfies the scaling relation $\beta = x_m\nu$.

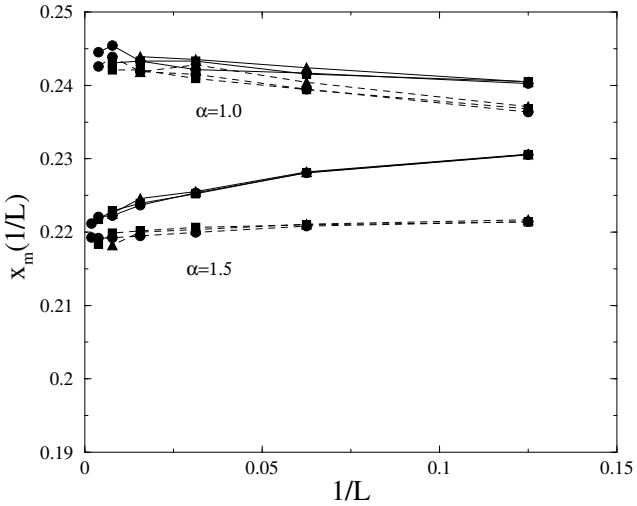

Figure 6.4: Effective magnetic exponents for $\alpha = 1.5$ and $\alpha = 1$. The full lines connecting the data for the transverse-field Ising model are guide to the eye. For a comparison the same quantities for the $q = 3$-state random quantum Potts chain are also presented, where the data points are connected by dashed lines.

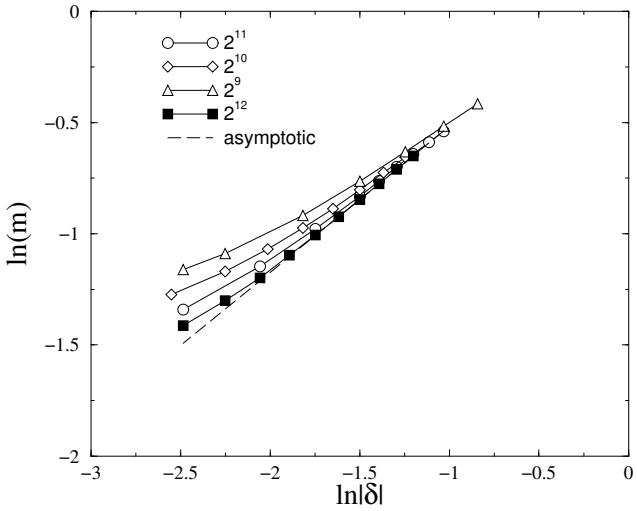

Figure 6.5: Average bulk magnetization in the ordered phase as a function of the quantum control parameter in a log-log plot ($\alpha = 1.5$). For small δ the finite size results converge to the dashed line with a slope of $\beta = 0.66$.

6.3 The two-dimensional problem

In this section we present our results for the two-dimensional case. We performed the RG-procedure following our previous study on normal disorder in two dimensions. We discarded the renormalized weak bonds according to the criterion given in (5.6). In this

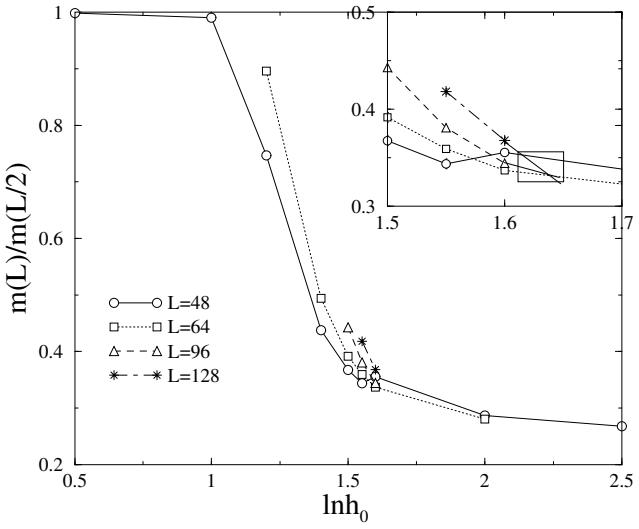

Figure 6.6: Finite-size estimates of the critical point and the magnetization scaling dimension of the $2d$ model with $\alpha = 3$.

way we could study sizes up to $N = L \times L = 128 \times 128$ and run typically $10\,000$ samples for $L \leq 64$ and some 1000 samples for $L = 96$ and $L = 128$.

To examine the dependence of the critical exponents on the Lévy index α, we had to first locate the critical points for various values of α. Following the method described in Sec. 5.3 and Sec. 5.4, we calculated the average magnetization $m(L, h_0)$ for a finite system size L at h_0, and calculated the ratio $g_L(h_0) = m(L, h_0)/m(L/2, h_0)$. At the critical point h_c, we have $g_L(h_c) = 2^{-x_m}$, which is independent of the system size L. Fig. 6.6 shows a plot of $g_L(h_0)$ as a function of h_0 for $\alpha = 3$. From the intersection of the curves, we can estimate the position of the critical point and the magnetization scaling dimension x_m. Fig. 6.7 shows the estimated magnetization scaling dimension x_m and the critical points for various values of α. As seen in this figure, x_m is decreases monotonously with $\alpha < \alpha_c$, whereas for $\alpha > \alpha_c$, x_m stays approximately constant and this value corresponds, within the error of estimates, to that of the $2d$ transverse-field Ising model with normal disorder, cf. Table 5.1. From Fig. 6.7, the cross-over value can be estimated as $\alpha_c \approx 4.5$. The magnetization scaling dimension, x_m, or more precisely $\phi\psi = 2 - x_m$, is also related to the finite-size behavior of the average cluster moment at the critical point: $[\mu_L]_{\rm av} \sim L^{\phi\psi}$, which is illustrated in Fig. 6.8 for $\alpha = 3$. From the slope of the line in a log-log plot one obtains an estimate of $\phi\psi = 0.48$, which is in agreement with the results shown in Fig. 6.7. Similar agreement is also found for other values of α.

Our final investigation concerns the scaling behavior of the distribution function of the log-energy scale, $P_L(\Gamma)$, at the critical point. As in the $1d$ problem the critical exponent, ψ, can be obtained from an optimal data collapse in terms of the scaling variable Γ/L^{ψ}. In Fig. 6.9 we present for $\alpha = 3$ the rescaled accumulated probability distribution function, where a satisfactory data collapse is obtained for $\psi = 0.8$. Similar estimates for other values of

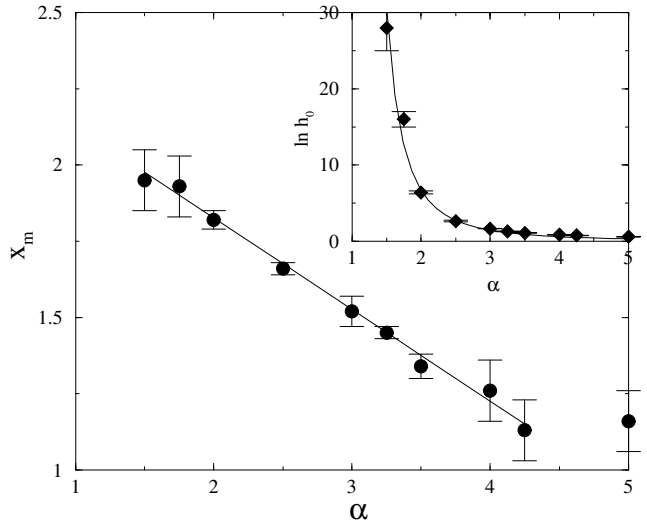

Figure 6.7: Magnetization scaling dimensions in $2d$ for different values of the Levy-index. In the inset the estimated critical points are presented. The line connecting the data points is a guide to the eye.

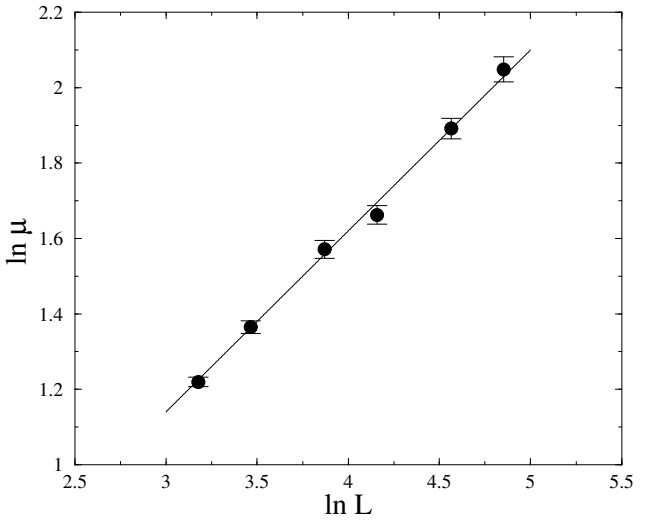

Figure 6.8: Average critical cluster moment as a function of size in a log-log plot ($\alpha = 3$). The slope of the line corresponds to $\phi\psi = 0.48$.

α are collected in Fig. 6.10. As for the x_m exponent, ψ is a monotonously decreasing function for $\alpha < \alpha_c \approx 4.5$, whereas for $\alpha > \alpha_c$ it is approximately constant and this value corresponds to that of the model with normal disorder as given in Table 5.1.

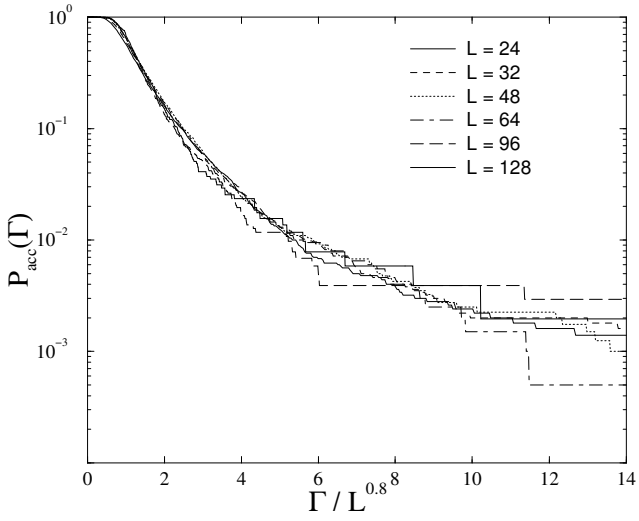

Figure 6.9: Rescaled accumulated probability distribution function of the log-energy-scale at $\alpha = 3$. Satisfactory data collapse is obtained with the exponent $\psi = 0.80$.

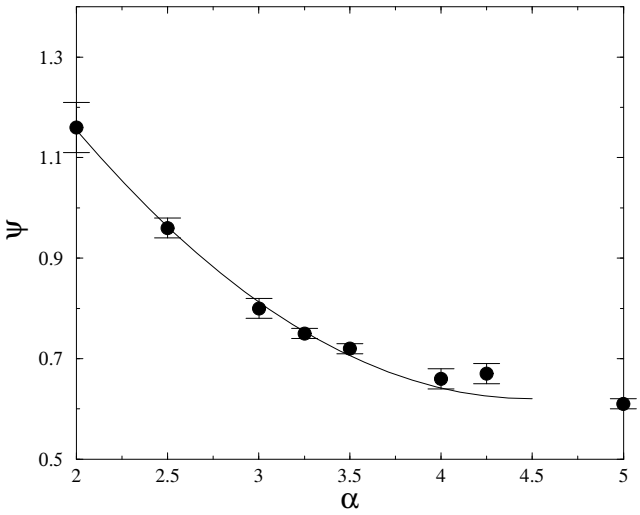

Figure 6.10: The critical exponent ψ as a function of the Lévy index for the $2d$ model. The line is a guide to the eye.

6.4 Summary

In this chapter the effect of a broad disorder distribution on the critical behavior of the random transverse-field Ising model is studied in one and two space dimensions. The broadness of the disorder distribution becomes relevant, if the Lévy index is lowered below a critical value, α_c. In the region of $1 < \alpha < \alpha_c$ the critical exponents of the infinite-randomness fixed point are continuous functions of α and for $\alpha > \alpha_c$ they are the same as in the model with normal disorder.

In $1d$ we obtained $\alpha_c = 2$, in close analogy with random walks, where the central limit theorem is valid for $\alpha > 2$. This analogy is more than a simple coincidence, since the $1d$ RW and the quantum Ising spin chain are related through an exact mapping [95], which then has the same requirement for the relevance-irrelevance conditions. In $2d$, where such type of mapping does not exist, the limiting value is found to be approximately around $\alpha_c \approx 4.5$, thus in the region of $2 < \alpha < \alpha_c$ the broadness of disorder is relevant for the random transverse-field Ising model, whereas it is irrelevant for the RW.

Outside the critical point, in the Griffiths-McCoy phase some physical quantities of random quantum Ising magnets (linear and non-linear susceptibility, autocorrelations, etc.) are still singular. In the presence of normal disorder these Griffiths-McCoy singularities are characterized by the dynamical exponent, $z(\delta)$, which is a function of the distance of the critical point. For broad distribution of the disorder, the probability of rare events is enhanced, consequently the Griffiths-McCoy singularities become stronger. In $1d$ we have shown by scaling arguments leading to (6.13) that the dynamical exponent is formally infinite in the whole Griffiths-McCoy phase.

Chapter 7

Strongly Disordered Spin Ladders[1]

7.1 Introduction

Apart from the random transverse-field Ising model, the critical points of certain random antiferromagnetic (AF) spin chains are also important examples for infinite-randomness fixed points, as we have mentioned in Chapter 4. In this chapter, we will extend our numerical renormalization-group studies to the random antiferromagnetic spin ladders.

Recently, investigations on antiferromagnetic spin ladder model have become very intensive. One of the main motivation for these investigations is due to the discovery of spin ladder materials [62]. From the theoretical point of view, two-leg ladders are analogous objects to $S = 1$ spin chains [54, 110], which has a gapped spectrum in absence of randomness, according to Haldane's conjecture [23]. Furthermore, the ground state of the spin-1 chain has a novel string-topological order measured by the string order parameter [31]:

$$O^{\alpha} = - \lim_{|i-j|\to\infty} \left\langle S_i^{\alpha} \exp\left(i\pi \sum_{l=i+1}^{j-1} S_l^{\alpha} \right) S_j^{\alpha} \right\rangle \ , \tag{7.1}$$

Ladder models with competing interactions, such as with staggered dimerization [74] and with rung and diagonal couplings [110], have been introduced and studied. In these models, depending on the relative strength of the couplings, there are also several gapped phases with different topological order, which are separated by first- or second-order phase transition lines.

Disorder effects on the gapped Haldane state of the spin-1 chain has been analyzed by using the Ma-Dasgupta-Hu (MDH) renormalization group (RG) method [69, 75]. It has been found that the degree of disorder needed to destroy the gapped Haldane phase appears

[1] From [127].

to be quite strong . Moreover, there are two different types of strongly disordered phases: When D, the strength of disorder exceeds a critical value D_c, the system is in a spin-1 random singlet phase and the singular behavior is controlled by an infinite-randomness fixed point; As D is decreased, the system undergoes a quantum phase transition to the gapless Haldane phase, where the dynamical exponent z in finite and varies continuously with D. We have discussed the analytical conclusions in Section 4.3.

Theoretical work about disordered spin ladders is mainly concentrated on the weak disorder limit. Results in this direction are obtained in the weak interchain coupling limit via the bosonization approach [83] and by the random mass Dirac fermion method [121]. In particular a remarkable stability of the phases of the pure system against disorder with XY symmetry has been observed [83].

In the experimental situation, however, the effect of disorder is usually strong. In this chapter we will consider the strongly disordered spin ladders and apply a numerical implementation of the MDH approach, which could treat the combined effect of disorder, frustration, correlations and quantum fluctuations. In particular we investigate the stability of the different topologically ordered phases and study the region of attraction of the infinite-randomness fixed point.

7.2 The models and their phase diagrams for non-random couplings

In this section we define different spin ladder models for our simulations and describe their phase diagram for non-random couplings.

We start with two spin-1/2 Heisenberg chains, labeled by $\tau = 1, 2$ and described by the Hamiltonians

$$H_\tau = \sum_{l=1}^{L} J_{l,\tau} \mathbf{S}_{l,\tau} \mathbf{S}_{l+1,\tau} \ , \tag{7.2}$$

where $\mathbf{S}_{l,\tau}$ is a spin-1/2 operator at site l and on chain τ and $J_{l,\tau} > 0$. For non-random spin chains dimerization can be introduced as

$$J_{l,\tau} = J \left[1 + \gamma(-1)^{l+n(\tau)}\right], \quad 0 \leq \gamma < 1 \ , \tag{7.3}$$

with $n(\tau) = 0, 1$, whereas for random dimerized couplings the even and odd bonds are taken from different distribution. The pure chain without dimerization ($\gamma = 0$) has a gapless spectrum, and spin-spin correlations decay as a power for large distance, which is called as quasi-long-range-order. Introducing dimerization for $\gamma > 0$ a gap opens in the spectrum [19], which is accompanied by non-vanishing dimer order, $O^{\alpha}_{\rm dim} \neq 0$. This is measured as the difference between the string order parameters in (7.1) calculated with spin-1/2 moments at even (e) and odd (o) sites:

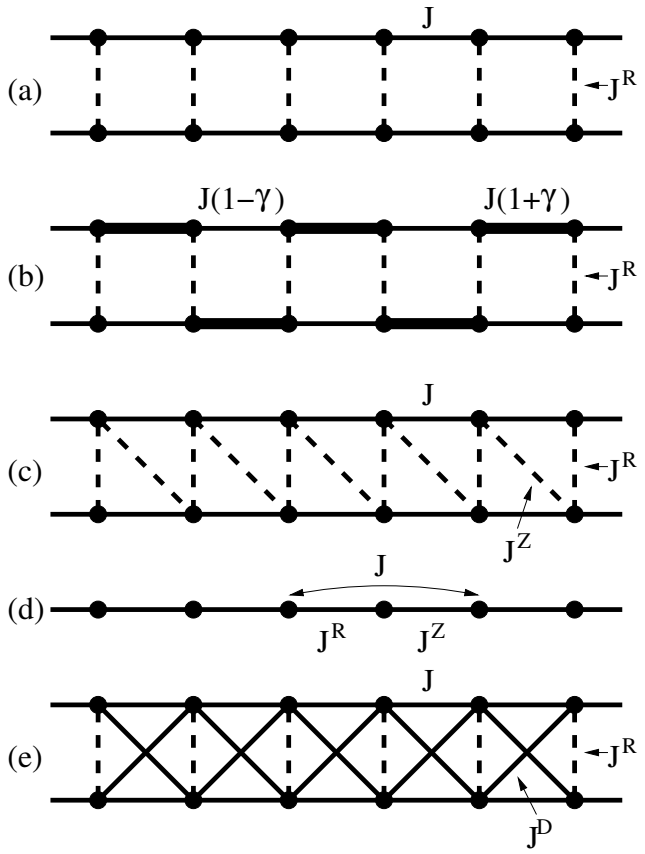

Figure 7.1: Spin-ladder models used in the chapter. The conventional two-leg ladder (a) and staggered dimerization in the chain couplings (b). The zig-zag ladder (c) and its representation as a chain with first and second neighbor couplings (d). The full ladder with rung and diagonal couplings (e).

$$O^{\alpha}_{\rm dim} = O^{\alpha}_{\rm e} - O^{\alpha}_{\rm o} \ . \tag{7.4}$$

In the following we generally consider non-dimerized chains, otherwise it is explicitly mentioned.

Now we introduce the interchain interaction

$$H_R = \sum_{l=1}^{L} J^R_l \mathbf{S}_{l,1}\mathbf{S}_{l,2} \ , \tag{7.5}$$

which describes the usual rung coupling between the ladders (see Fig. 7.1.a). The conventional ladder model is described by the Hamiltonian: $H = H_1 + H_2 + H_R$. In the pure model by switching on the AF rung couplings, $J^R_l = J^R > 0$, a Haldane-type gap opens above the ground state and the system has a non-vanishing odd string topological order,

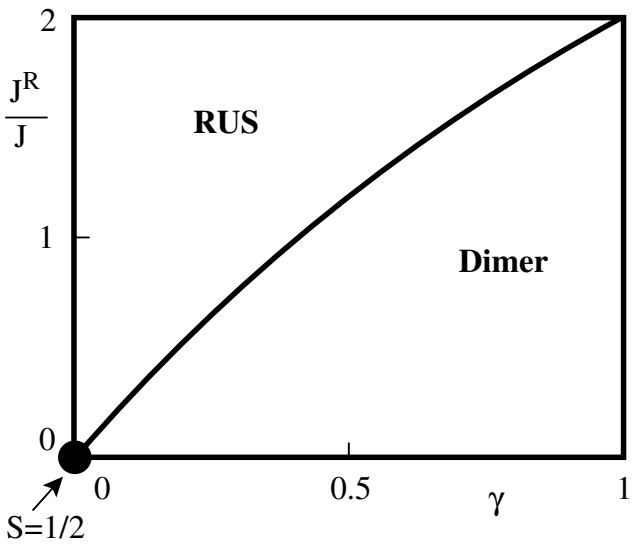

Figure 7.2: Schematic phase diagram of the two-leg AF ladder with staggered dimerization (see Fig. 7.1.b for the definition of the couplings.) At the phase boundary between the rung singlet and dimer phases the gap vanishes.

which is measured by[2] [110]:

$$O^{\alpha}_{\mathrm{odd}} = -\lim_{|i-j|\to\infty} \left\langle (S^{\alpha}_{i,1} + S^{\alpha}_{i,2}) \exp\left(i\pi \sum_{l=i+1}^{j-1} (S^{\alpha}_{l,1} + S^{\alpha}_{l,2}) \right) (S^{\alpha}_{j,1} + S^{\alpha}_{j,2}) \right\rangle . \qquad (7.6)$$

For strong AF rung couplings every spin-pair on the same rung form a singlet, therefore this phase is called the *rung singlet* (RUS) phase.

Dimerization of the chain couplings could occur in two different ways. For parallel dimerization, when equal bonds in the two chains are on the same position, i.e. in (7.3) $n(1) = n(2)$, the combined effect of rung coupling and dimerization will always result in a gapped phase. In the other possible case of staggered dimerization, i.e. with $n(1) = -n(2)$ (see Fig. 7.1.b), the two chains have an opposite dimer order, which competes with the rung coupling. As a result the phase diagram of the system (see Fig. 7.2) consists of two gapped phases, which are separated by a gapless transition line, starting in the pure, decoupled chains limit [74].

Next, we extend our model by diagonal interchain couplings, given by the Hamiltonian term:

$$H_Z = \sum_{l=1}^{L} J^Z_l \mathbf{S}_{l,2} \mathbf{S}_{l+1,1} \ . \qquad (7.7)$$

[2]The notations about "odd" and "even" string topological order are related to the positions of the composite spin-1 operators with an eigenvalue of $S^z = \pm 1$, see [110].

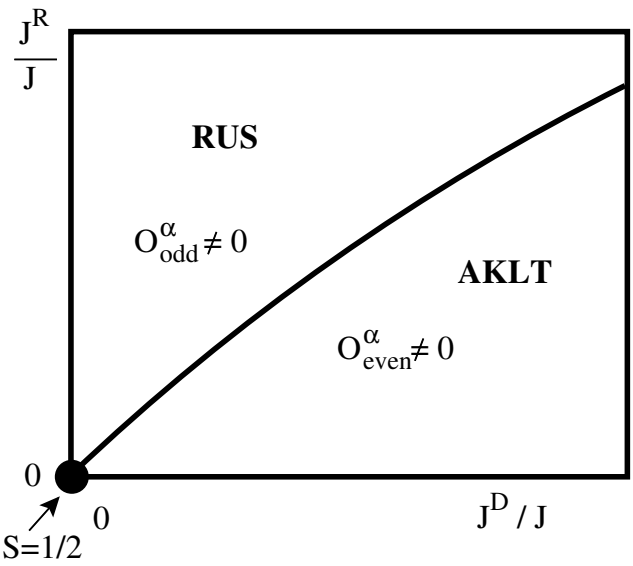

Figure 7.3: Schematic phase diagram of the full AF ladder with homogeneous rung and diagonal couplings. The transition between the two topologically distinct gapped phases is of first order, except of the limit $J_R = J_D = 0$.

The complete Hamiltonian, $H = H_1 + H_2 + H_R + H_Z$, describes a zig-zag ladder (see Fig. 7.1.c) or can be considered as a spin chain with nearest neighbor ($J_l^R,\ J_l^Z$) and next-nearest neighbor (J_l) couplings (Fig. 7.1.d). The pure model with $J_l^R = J_l^Z = J_1$ and $J_l = J_2$ has two phases: a gapless phase for $J_2/J_1 < .24$ is separated from a gapped phase by a quantum phase transition point.

Finally, we extend our model by two types of diagonal couplings, which are represented by the Hamiltonian:

$$H_D = \sum_{l=1}^{L} J_l^D (\mathbf{S}_{l,1}\mathbf{S}_{l+1,2} + \mathbf{S}_{l,2}\mathbf{S}_{l+1,1}) \ . \tag{7.8}$$

It is known that the pure AF diagonal ladder described by the Hamiltonian, $H = H_1 + H_2 + H_D$ with $J_l^D = J^D > 0$ has a gapped spectrum [110]. Its ground state has a non-vanishing even string order (see footnote on p.92), defined in analogy to (7.6):

$$O^{\alpha}_{\text{even}} = -\lim_{|i-j|\to\infty} \left\langle (S^{\alpha}_{i+1,1} + S^{\alpha}_{i,2}) \exp\left(i\pi \sum_{l=i+1}^{j-1} (S^{\alpha}_{l+1,1} + S^{\alpha}_{l,2}) \right) (S^{\alpha}_{j+1,1} + S^{\alpha}_{j,2}) \right\rangle \ . \tag{7.9}$$

In the full ladder, which contains both rung and diagonal couplings (see Fig. 7.1.e) is described by the Hamiltonian $H = H_1 + H_2 + H_R + H_D$ for non-random AF couplings there is a competition between rung and diagonal couplings, so that the ground state phase diagram of the system consists of two topologically distinct gapped phases (see Fig. 7.3). The phase transition between the two phases is of first order [110].

The main subject of our numerical study by MDH RG method is to investigate how the phase diagrams of the pure ladder models, in particular in Figs. 7.2 and 7.3, are modified due to the presence of quenched disorder.

7.3 Renormalization procedure for antiferromagnetic spin ladders

With the ladder geometry, spins are more interconnected than in a chain, which leads to a modification of the RG procedure described in Section 4.3. In this modified RG procedure, the effective couplings generated according to the perturbation theory can also be ferromagnetic. To see this, let us consider a decimation process shown in Fig. 7.4, in which the the singlet pair formed by the spins $\mathbf{S}_2$ and $\mathbf{S}_3$ is to be eliminated. Treating the terms $J_{12}\mathbf{S}_1 \cdot \mathbf{S}_2$ and $J_{24}\mathbf{S}_2 \cdot \mathbf{S}_4$ as perturbations to the singlet pair, we obtain an effective Hamiltonian involving the spins $\mathbf{S}_1$, $\mathbf{S}_2$, $\mathbf{S}_3$ and $\mathbf{S}_4$, expressed as

$$\widetilde{\mathcal{H}'} = \text{const} - \sum_{\alpha} \frac{2J_{12}J_{24}}{J_{23}} \langle 0| \, S_2^{\alpha} S_2^{\alpha} \, |0\rangle \, S_1^{\alpha} S_4^{\alpha} \ , \tag{7.10}$$

where $|0\rangle$ denotes the singlet formed by $\mathbf{S}_2$ and $\mathbf{S}_3$. The effective coupling connecting $\mathbf{S}_1$ and $\mathbf{S}_4$ then is ferromagnetic and given by

$$\widetilde{J}_{14} \approx -\frac{2}{3} S_2(S_2+1) \frac{J_{12}J_{24}}{J_{23}} \ . \tag{7.11}$$

Since the renormalized Hamiltonian now contains both antiferromagnetic and ferromagnetic couplings, an effective spin with a non-vanishing moment can be formed during the renormalization. This is different from the RG procedure for the antiferromagnetic spin chain discussed in Section 4.3, in which an effective spin forms exclusively a singlet.

With this modification, a full renormalization consists of two types of decimation rules, one for singlet formation and the other for cluster formation [111], which we will describe in the following. We consider two spins with spin values S_2 and S_3 at sites 2 and 3, respectively, connecting by a very strong coupling J_{23}. If $J_{23} < 0$ is ferromagnetic, an effective spin cluster of size $S = S_2 + S_3$ is formed, and the gap to the first excited

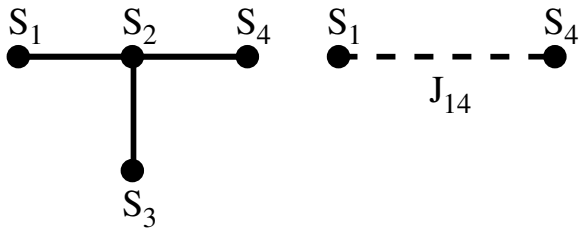

Figure 7.4: Singlet formation of spin $\mathbf{S}_2$ and spin $\mathbf{S}_3$ leads to a ferromagnetic coupling $\widetilde{J}_{14}$.

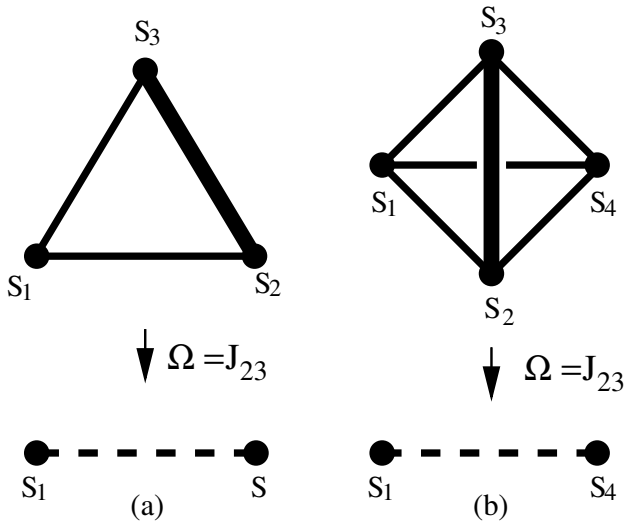

Figure 7.5: (a): a cluster formation; (b): a singlet formation. The dashed line represent renormalized couplings.

multiplet in the isolated cluster is given by $\Delta_{23} = |J_{23}|S$. If $J_{23} > 0$ is antiferromagnetic, the effective spin cluster for S_2 and S_3 has a spin size $S = |S_2 - S_3|$, and the corresponding first gap is given by $\Delta_{23} = J_{23}(S+1)$. In each step of RG, we pick up the pair of spins with the largest energy gap that sets the energy scale of the RG, then replace it with an effective spin of size $S > 0$ or remove it for the case of a singlet $S = 0$.

1. **Cluster formation**
   We first consider the case in which a cluster with a finite spin size S is formed by $\mathbf{S}_2$ and $\mathbf{S}_3$, corresponding to (a) in Fig 7.5. The ground energy of the strongly coupled two-spin Hamiltonian
   $$\mathcal{H}'_0 = J_{23}\mathbf{S}_2 \cdot \mathbf{S}_3 \tag{7.12}$$
   is degenerate. Under the action of the perturbation
   $$\mathcal{H}'_I = J_{12}\mathbf{S}_1 \cdot \mathbf{S}_2 + J_{13}\mathbf{S}_1 \cdot \mathbf{S}_3 \ , \tag{7.13}$$
   the degeneracy will be partly lifted and an effective Hamiltonian $\widetilde{\mathcal{H}'}$ induced. We calculate $\mathcal{H}'$ in first-order perturbation theory:
   $$\widetilde{\mathcal{H}'} = P_0 \mathcal{H}'_I P_0 \tag{7.14}$$
   where P_0 projects onto the eigensubspace of $\mathcal{H}'_0$. This leads to
   $$\widetilde{\mathcal{H}'} = \tilde{J}_1 \mathbf{S}_1 \cdot \mathbf{S} \tag{7.15}$$
   with an effective coupling given by
   $$\tilde{J}_1 = c_{12}J_{12} + c_{13}J_{13} \ , \tag{7.16}$$

where c_{12} and c_{13} satisfies the operator identities

$$\mathbf{S}_1 \cdot \mathbf{S}_2 = c_{12}\mathbf{S}_1 \cdot \mathbf{S} \ , \tag{7.17}$$

$$\mathbf{S}_1 \cdot \mathbf{S}_3 = c_{13}\mathbf{S}_1 \cdot \mathbf{S} \ , \tag{7.18}$$

and are given by [71, 111]

$$c_{12} = \frac{S(S+1) + S_2(S_2+1) - S_3(S_3+1)}{2S(S+1)} \ , \tag{7.19}$$

and

$$c_{13} = \frac{S(S+1) + S_3(S_3+1) - S_2(S_2+1)}{2S(S+1)} \ , \tag{7.20}$$

derived from the Wigner-Eckart theorem [26].

2. **Singlet formation**
   Now we turn to singlet formation, with $S_2 = S_3$ coupled by an antiferromagnetic coupling. Combining the calculation in (4.28)-(4.29) and (7.10)-(7.11), for the general case shown in Fig. 7.5 (b), we obtain the renormalized coupling in the form:

$$\widetilde{J}_{14} = J_{14} + \frac{2S_2(S_2+1)}{3J_{23}}(J_{12} - J_{13})(J_{43} - J_{42}) \ , \tag{7.21}$$

   which should reproduce the result in (4.29) for the chain topology if $J_{13} = J_{42} = 0$, and the result in (7.11) for a ferromagnetic renormalized coupling if $J_{12} = J_{24} = 0$.

In practice we use a finite size version of the MDH renormalization, as for the random transverse-field Ising model we discussed in chapter 5 and 6. We start with a finite ladder of L sites and with periodic boundary conditions and perform the decimation procedure until one spin pair with a first gap Δ remains in the system. Since Δ plays the role of the energy scale at length scale L, Δ and L should be related by the relation $\Delta \sim L^{-z}$, involving the dynamical exponent z. Performing the above decimation for different samples the probability distribution of Δ in the small Δ limit is described by the form

$$P_L(\ln \Delta) \sim L\Delta^{1/z} \ . \tag{7.22}$$

The infinite-randomness fixed point is signaled by a diverging z, or more precisely the distributions $P_L(\Delta)\mathrm{d}\Delta$ have strong L dependence, so that the appropriate scaling combination is

$$\ln\left(L^{\psi}P_L(\Delta)\right) \simeq f\left(L^{-\psi}\ln\Delta\right) \ , \tag{7.23}$$

which can be obtained from (7.22) by formally setting $z \simeq -\ln\Delta \sim L^{\psi}$.

7.4 Results

In the following subsections, we will present the results from our numerical RG-study on the ladder models defined in Sec. 7.2 with disorder. The couplings of models are random variables taken from the distribution in a power-law form:

$$P_{\mathrm{pow}}(J) = \frac{1}{D} J^{-1+1/D} \tag{7.24}$$

with a parameter D representing the strength of randomness. For the case $D = 1$, the distribution is uniform. In our numerics, we used several $100\,000$ realizations for each model and ran up to linear system size $L = 512$. From the distribution of the gap at the last step of the RG iteration we calculated the dynamical exponent, z.

7.4.1 Random conventional ladders

We start with the conventional ladders in Fig. 7.1(a) where the couplings along the chains ($J_l^\tau,\ \tau = 1, 2$) and the couplings along the rungs (J_l^R) are taken from the same random distribution. In Fig. 7.6 we show the probability distribution of the gaps at the last step of the RG iteration calculated with the disorder parameter $D = 1$. As seen in the figure, the small energy tail of the distribution follows the functional form given by (7.22). The dynamical exponent z given by the asymptotic slope of the distributions is finite and has only a very weak size dependence.

Repeating the calculation for other values of D we obtain a set of D-dependent dynamical exponents which are represented on Fig. 7.7. For strong disorder we obtain $z(D) < D$, which means that disorder is reduced in the course of the renormalization. In the terminology of Motrunich et al. [105], this system is a *finite randomness* system, as opposed to the infinite randomness systems that will be considered in the next subsections. For weak disorder the dynamical exponent predicted by the approximative MDH renormalization is lowered below one for $D < D_0 \approx 1$. Here we argue that in this region the effect of disorder is irrelevant, so that the system is in the gapped RUS phase. Indeed, in a pure quantum system, where scaling in time and space is isotropic, the dynamical exponent is $z_{\mathrm{pure}} = 1$. For disorder induced gapless systems, where disorder in the time direction is strictly correlated, the dynamical exponent can not be smaller, than in the pure system, so that $z_{\mathrm{random}} \geq z_{\mathrm{pure}} = 1$. Consequently, if the disorder induced dynamical exponent is $z_{\mathrm{random}} < 1$, then disorder could only influence the correction to scaling behavior, but the system stays gapped. In view of this remark, D_0 can be considered as the lower limiting value of the disorder, where the conventional finite randomness behavior ends. So that the phase diagram of random conventional two-leg spin ladders consists of two phases: a gapped RUS (Haldane) phase and a random gapless Haldane phase. The latter is characterized by a finite dynamical exponent $z(D)$ for any strong but finite initial disorder.

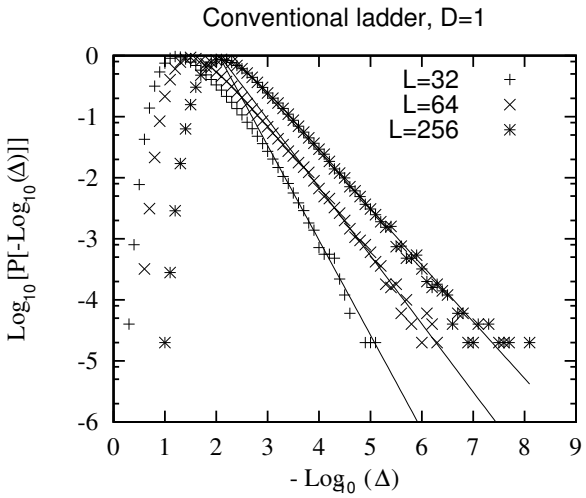

Figure 7.6: Probability distribution of the first gaps for the conventional random ladder with $D = 1$ (see (7.24)) and system size $L = 32$, $L = 64$, and $L = 256$. For clarity, we have not shown the data corresponding to $L = 128$. The solid lines represent the best fit to the form $\log_{10}[P[-\log_{10}\Delta]] = A_L - \frac{1}{z_L}\log_{10}\Delta$, with $A_{32} = 3.18$, $A_{64} = 2.30$, $A_{128} = 1.92$, $A_{256} = 2.14$ and $z_{32} = 0.65$, $z_{64} = 0.90$, $z_{128} = 1.06$, and $z_{256} = 1.07$. We deduce that the asymptotic value of the dynamical exponent is $z_\infty \simeq 1.07$.

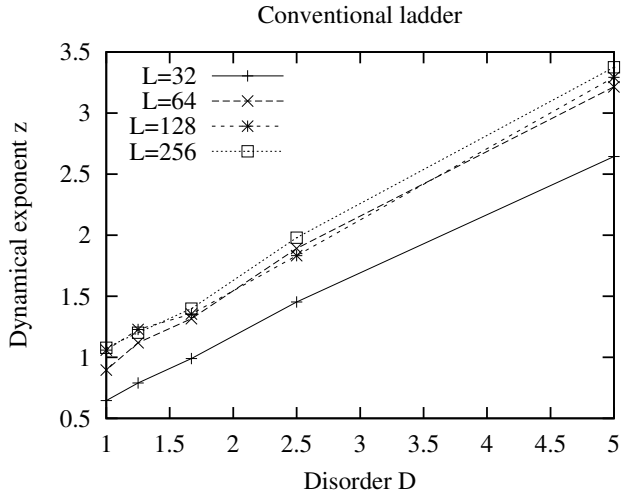

Figure 7.7: Variation of dynamical exponent z with disorder D for the conventional ladder with lengths $L = 32$, $L = 64$, $L = 128$, and $L = 256$. For large system sizes and strong disorder, one has $z_\infty \simeq 0.42 + 0.58D < D$. In the region with $z_\infty < 1$, where the disorder is irrelevant, the system is in the gapped Haldane phase (see text).

Consequently there is an important difference with the random AF spin-1 chain which flows into the infinite-randomness fixed point above a finite critical value of randomness (see Fig. 4.4).

7.4.2 Random ladders with staggered dimerization

In this subsection we consider conventional ladders with staggered dimerization having a dimerization parameter, $0 \leq \gamma \leq 1$, in (7.3). The different type of couplings in the ladder are taken from the power-law distribution in (7.24), each having the same disorder parameter, D, however the range of the distribution for the different type of couplings are, $0 < J_l^R < J_{\max}^R$ for the rung couplings, $0 < J_l^{\text{weak}} < (1-\gamma)J_{\max}$ and $0 < J_l^{\text{strong}} < (1+\gamma)J_{\max}$ for the weaker and stronger chain couplings, respectively. For a fixed value of γ and D we have calculated the finite-size dependent effective dynamical exponent, z, as a function of the coupling ratio, $J_{\max}^R/J_{\max}$.

As shown in Fig. 7.8 the effective exponents have the same qualitative behavior for different values of the dimerization parameter, γ. In each case the curves have a maximum at some value of the couplings, where the finite-size dependence is the strongest, whereas farther from the maximum the convergence of the data is faster.

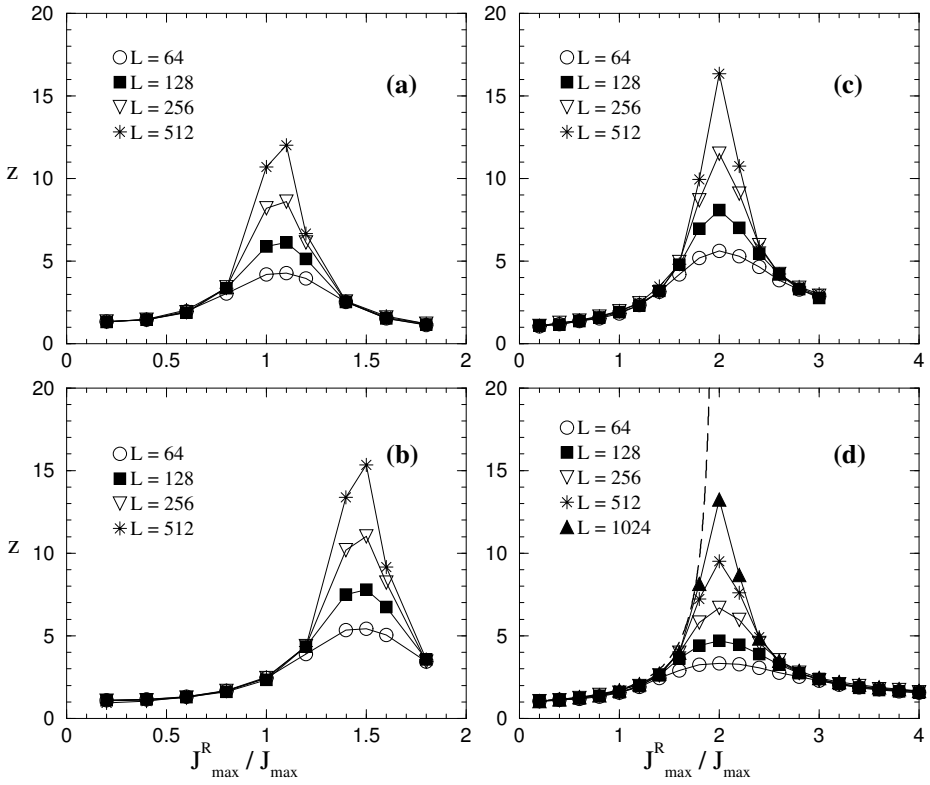

Figure 7.8: Finite-size estimates of the dynamical exponent of random conventional ladders with staggered dimerization as a function of the coupling ratio, $J_{\max}^R/J_{\max}$, with a disorder parameter $D = 1$ and for different dimerizations: (a) $\gamma = 0.5$, (b) $\gamma = 0.75$, (c) $\gamma = 1$. In (d) a similar calculation for the random XX-chain is presented ($D = 1,\ \gamma = 1$), where the exact dynamical exponent in (7.25), obtained in the $L \to \infty$ limit, is shown by dashed line.

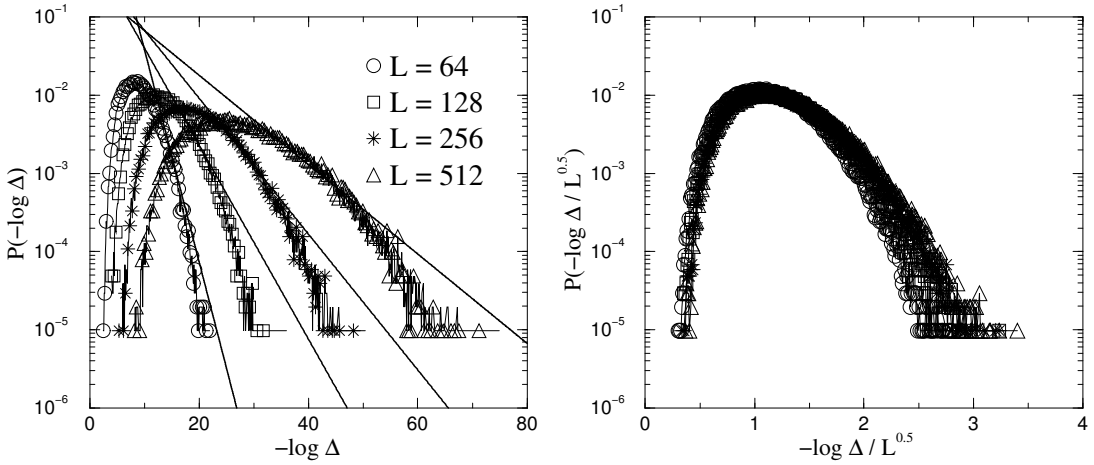

(a) (b)

Figure 7.9: (a): Probability distribution of the first gap at the transition point of the random conventional ladder with staggered dimerization, $D = 1$, $\gamma = 0.5$, $J^R_{\max}/J_{\max} = 1.1$. The effective dynamical exponent, given by the inverse slope of the curves and indicated by straight lines, is increasing with size without limits. (b): Scaling plot of the data given in (a), using the scaling combination, using the scaling $-\ln \Delta \sim L^{\psi}$ with $\psi = 1/2$.

To decide about the possible limiting value of z, in particular at the maximum of the curves, we analyze the behavior for $\gamma = 1$ in Fig. 7.8(c), which is just a dimerized random chain, the properties of which are exactly known by some extent [41, 106]. The random critical point of this system is situated at $J^R_{\max}/J_{\max} = 2$, where the critical behavior governed by an infinite-randomness fixed point, so that the dynamical exponent, z, is formally infinity. For any other values of the couplings, $J^R_{\max}/J_{\max}$, the system is in the random dimer phase, where the dynamical exponent is finite and coupling dependent. To see the general tendency of finite-size convergence of the z exponent around the critical point, we have repeated the calculation at the $D = 1,\ \gamma = 1$ case for the random XX-chain. The numerical finite-size results are compared in Fig. 7.8(d) with the exact value of the dynamical exponent given by the solution of the equation (cf. (4.38)):

$$\frac{J^R_{\max}}{J_{\max}} = 2\left(\frac{D^2}{D^2 - z^{-2}}\right)^{-z} , \tag{7.25}$$

known from [106, 115, 126]. As seen in Fig. 7.8, the dynamical exponents of random XX- and Heisenberg-ladders have very similar coupling dependence and one expects the same type of divergence at the critical point for all values of γ.

In Fig. 7.9 we illustrate the scaling behavior of the gap at the transition point, i.e. at the maximum of the curve in Fig. 7.8(a). The distributions in Fig. 7.9(a) become broader and broader with the size and the effective dynamical exponent is increasing with the size without limits. An appropriate scaling collapse of the gap-distributions has been obtained

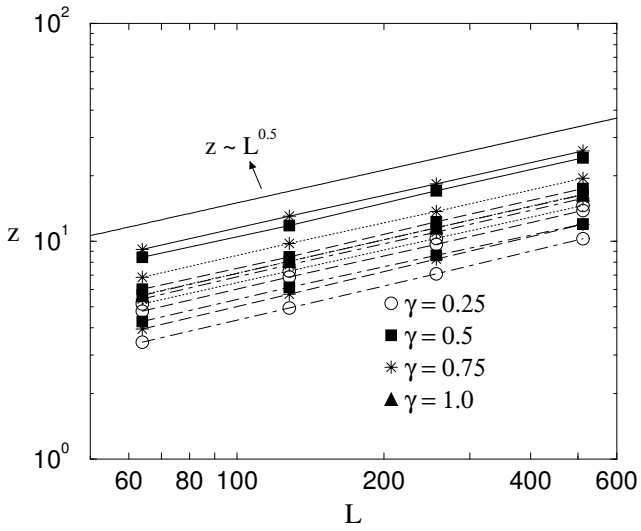

Figure 7.10: Finite-size dependence of the dynamical exponent at the transition point of random staggered dimerized ladders for different values of the dimerization and for different strength of disorder: $D = 0.25$ (solid line), $D = 0.5$ (dotted line), $D = 0.75$ (dashed line) $D = 1$ (dashed-dotted line). In the log-log plot the slopes of the curves are compatible with $\psi = 1/2$.

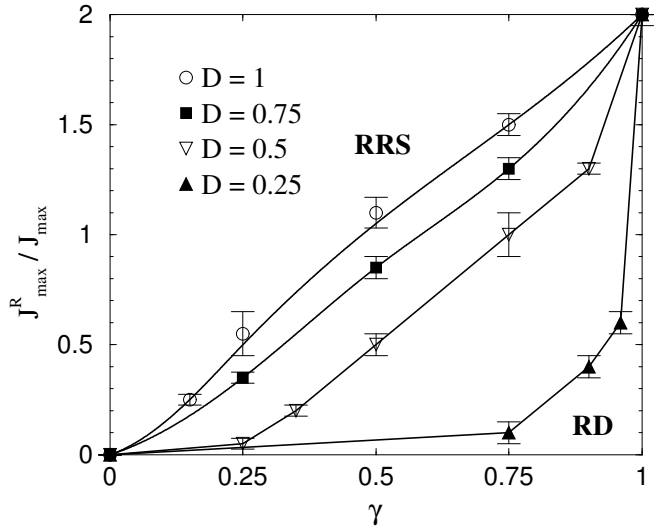

Figure 7.11: Phase diagram of random conventional ladders with staggered dimerization for different disorder parameters. The random dimer (RD) phase and the random rung singlet (RRS) phase are separated by a random critical line of infinite randomness behavior.

in Fig. 7.9(b), where the scaling variable in (7.23) with $\psi = 1/2$ is used. We have also studied the finite-size dependence of the dynamical exponent at other points of the critical line in Fig. 7.10. From the relation $z \simeq -\ln \Delta \sim L^{\psi}$, we obtained estimates for the

ψ exponent relating the time scale τ and length scale L via $\ln \tau \sim L^{\psi}$, which are all compatible with the value, $\psi = 1/2$, which is characteristic of the infinite-randomness fixed point of the random AF chain.

Thus we conclude that the random conventional ladder with staggered dimerization has two Griffiths-McCoy gapless phases, the random dimer phase and the random rung singlet phase, which are separated by a random critical line, along which there is *infinite randomness* behavior. For different disorder parameter, D, the position of the random critical line is modified, see Fig. 7.11.

We note that the previously studied random conventional ladder is contained as a special point in this phase diagram at $J^R_{\max}/J_{\max} = 1$ and $\gamma = 0$. This point is in the random rung singlet phase for any value of D, thus the dynamical exponent is finite in accordance with the previous results.

7.4.3 Random zig-zag ladders

For the zig-zag ladders the nearest neighbor couplings ($J^R_l = J^Z_l \equiv J^1_l$) are taken from the power-law distribution in (7.24) with the coupling J^1_l within the range $0 < J^1_l < J^1_{\max}$. Similarly, the next-nearest neighbor couplings ($J_l \equiv J^2_l$) are taken from the same type of power-law distribution and the range of couplings is now $0 < J^2_l < J^2_{\max}$.

The calculated dynamical exponent, z, as shown in Figs. 7.12, has its maximum at $J^2_{\max}/J^1_{\max} = 0$ and around this point one can observe strong finite-size dependence, the range of which is wide, in particular for weak disorder. At $J^2_{\max}/J^1_{\max} = 0$, where the zig-zag ladder reduces to a random AF chain, the system is governed by an infinite-randomness fixed point, thus the extrapolated value of the dynamical exponent is formally infinity. Given the strong finite-size corrections in the numerical RG data of the dynamical exponent[3] in Fig. 7.12, it is difficult to decide whether the infinite-randomness behavior of the zig-zag ladders is extended to a finite region of the couplings $J^2_{\max}/J^1_{\max} > 0$ or whether this region shrinks to a single point only. The first scenario may be related to the existence of a gapless phase of the pure model for $J^2/J^1 < 0.24$.

To discuss this issue, we have calculated the dynamical exponent by an independent method based on density matrix renormalization-group (DMRG). In principle, the dynamical exponent is related to the distribution of the first gap, Δ, in the small Δ limit, as given in (7.22). However, a precise numerical calculation of a small Δ by the DMRG method is very difficult, therefore we used another strategy, as described in details in [115, 126, 124]. By this method one considers the equivalent AF chain with random first- and second-neighbor

[3]The strong finite-size dependence of the RG-data indicates that several decimation steps are needed before the asymptotic region of the RG-flow is reached. This type of slow convergence for the zig-zag and the $J_1 - J_2$ ladders is probably connected with the effect of frustration, which is not there for the conventional ladder, with and without dimerization.

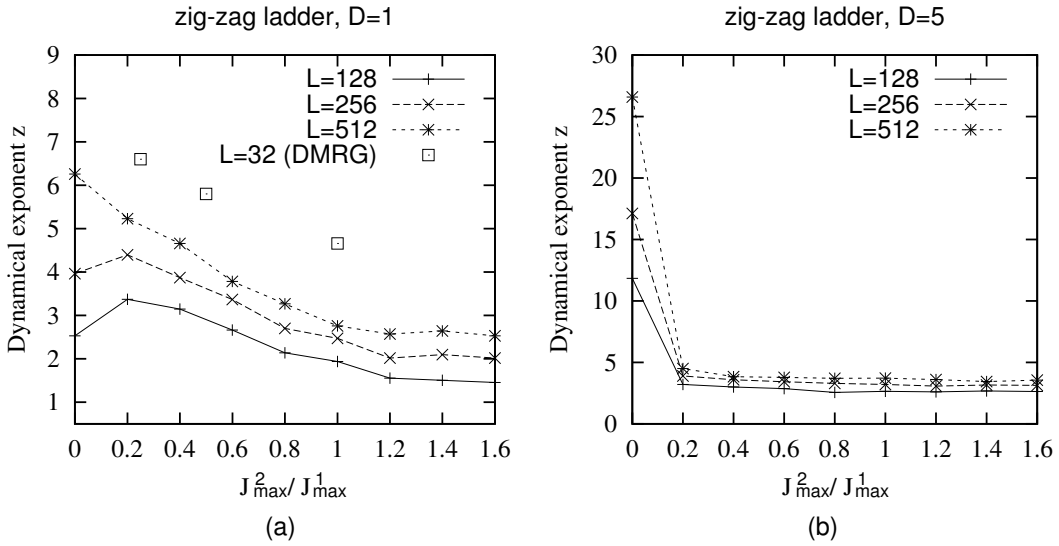

Figure 7.12: Variation of the dynamical exponent z versus $J^2_{\max}/J^1_{\max}$ for the zig-zag ladder with a disorder parameter $D = 1$ (a) and $D = 5$ (b). For $D = 1$, the MDH renormalization group data with $L = 128$, $L = 256$ and $L = 512$ have been compared to the DMRG calculation with $L = 32$ (see Fig. 7.13). The lines connecting the calculated points are guides to the eyes.

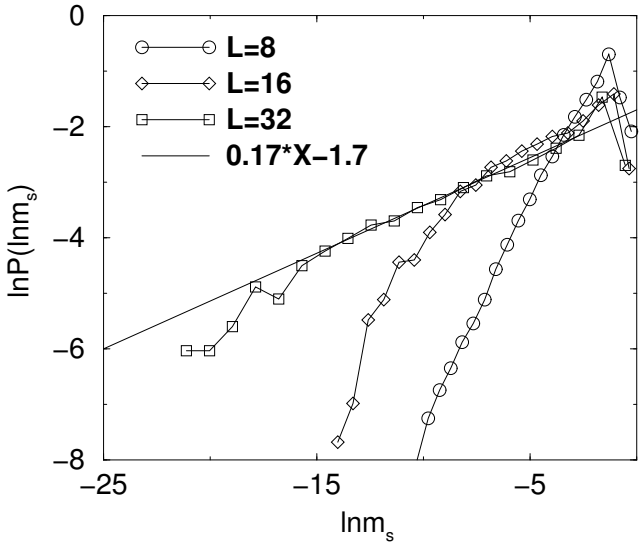

Figure 7.13: Distribution of the log surface magnetization of the random zig-zag ladder using a power-law distribution ($D = 1$, $J^2_{\max}/J^1_{\max} = 0.5$), for different lengths of the ladder, L. The asymptotic slope of the distribution, indicated by the straight line, is the inverse of the dynamical exponent, see (7.26).

couplings (see Fig. 7.1d) and with fixed-free boundary conditions and calculate the surface magnetization, m_s, at the free end, which can be done very accurately by the DMRG method. As argued in [115, 126, 124] for a random chain m_s and Δ can be considered as dual quantities, so that the distribution of the surface magnetization is asymptotically given by

$$P(\ln m_s) \sim m_s^{1/z}, \quad m_s \to 0. \tag{7.26}$$

Thus the dynamical exponent z can be obtained from an analysis of the small m_s tail of the distribution, as illustrated in Fig. 7.13 where the distribution function of $\ln m_s$ is given in a log-log plot for different lengths of the ladder. As seen in this Figure, the slope of the distribution is well defined for larger systems, from which one can obtain an accurate estimate for the dynamical exponent, which is finite. Repeating the calculation for other values of the coupling ratio, $J^2_{\max}/J^1_{\max}$, we have obtained a set of the dynamical exponents, which are plotted in Fig. 7.12. These accurate DMRG data show that the extrapolated values of the effective exponents calculated by the numerical RG-method are finite for any $J^2_{\max}/J^1_{\max} > 0$. Consequently the random zig-zag ladder has just one infinite-randomness fixed point at $J^2_{\max}/J^1_{\max} = 0$, and is in a gapless random dimer phase in the region of $J^2_{\max}/J^1_{\max} > 0$. In view of the numerical results in Fig. 7.12, where z_∞ seems to stay over $z_{\rm pure} = 1$, it is quite probable that the random dimer phase exists for any small value of the disorder.

7.4.4 Random J_1–J_2 ladders

The full ladder, as represented in Fig. 7.1(e) has three different type of couplings: J_l, J_l^R and J_l^D. Here we consider a special case of this model: the chain (J_l) and rung (J_l^R) couplings are taken from the same power-law distribution with a disorder parameter D and having a range of $0 < J_l, J_l^R < J^1_{\max}$, while the diagonal couplings are taken from the same type of power-law distribution but are within the interval $0 < J_l^D < J^2_{\max}$. This model, having first- and second-neighbor interactions, is called a J_1–J_2 ladder.

We have calculated the finite-size dynamical exponents as a function of the coupling ratio $J^2_{\max}/J^1_{\max}$ for different strength of disorder (see Fig. 7.14). These curves show similar qualitative behavior as those calculated for the random conventional ladders with staggered dimerization in Fig. 7.8, so that we can draw similar conclusions. The extrapolated position of the maximum of the z curves is identified as a quantum critical point with infinite randomness behavior. The shape of the probability distribution of the first gaps is very suggestive of an infinite randomness behavior. It is visible on Fig. 7.15 that close to the maximum of the z curves, $P\left[-\log_{10}\Delta\right]$ does not extrapolate to the linear behavior $A_\infty - \frac{1}{z_\infty}\log_{10}\Delta$ in the limit of large L, unlike the finite randomness behavior in Fig. 7.6. Instead the exponent z tends to infinity as the system size is increased, and the exponent ψ, determined similarly to Fig. 7.10, is compatible with $\psi = 1/2$, as observed for random

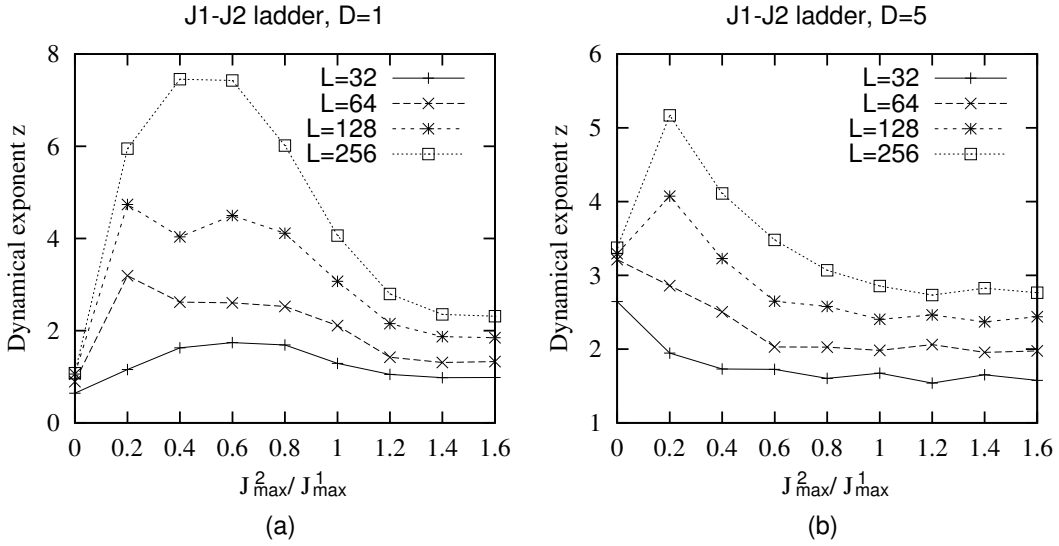

Figure 7.14: Variation of the dynamical exponent z versus $J^2_{\max}/J^1_{\max}$ for the random J_1–J_2 ladder with a disorder parameter $D = 1$ (a) and $D = 5$ (b). The lines connecting the calculated points are guides to the eyes. The uncertainty in the value of z measured around the maximum of the curves is due to the numerical method, as illustrated in Fig. 7.15 and explained in the text. Note the strong finite-size corrections in the Griffiths-McCoy phases.

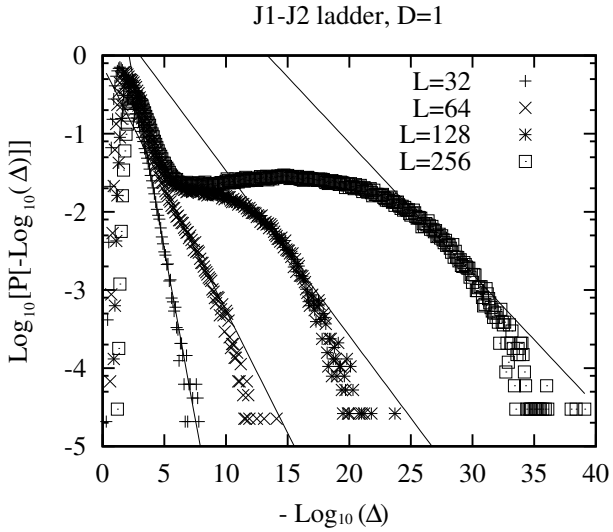

Figure 7.15: Probability distribution of the first gaps for the J_1–J_2 random ladder with a disorder parameter $D = 1$ (see (7.24)), corresponding to the maximum of the z-curve in Fig. 7.14. The straight lines indicate the fits used to estimate the value of z in Fig. 7.14.

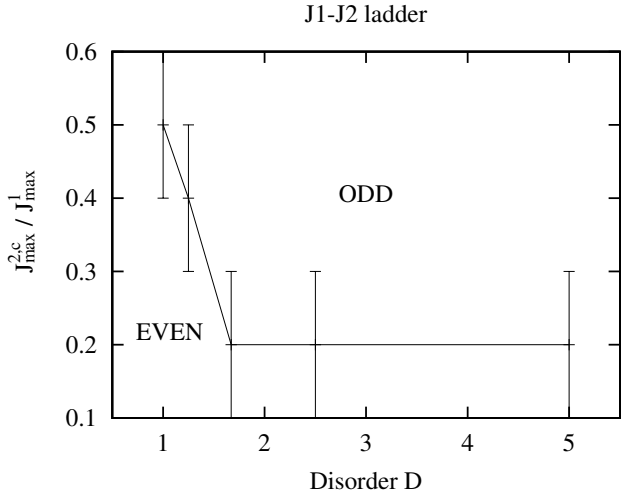

Figure 7.16: Phase diagram of the random J_1–J_2 ladder obtained from the maximum in the variation of the dynamical exponent versus $J^2_{\max}/J^1_{\max}$ for the largest available sizes $L = 256$ (see Fig. 7.14 for $D = 1$ and $D = 5$). The two straight lines connecting the calculated transition points are guides to the eyes. The whole transition line between the two phases with even and odd topological orders, respectively, is presumably a line of infinite-randomness fixed points.

ladders with a staggered dimerization. The random quantum critical point separates two gapless Haldane phases, having odd and even topological order, respectively.

Repeating the calculation for different disorder parameters we obtain a phase diagram shown in Fig. 7.16. In the range of disorder we used in the calculation the random critical point is always attracted by an infinite-randomness fixed point, this property probably remains true for any small value of disorder.

7.5 Discussion

In this chapter different types of random AF spin ladder models have been studied by a numerical strong-disorder RG method. In particular we considered the questions i) how the phase diagrams of the pure models are modified due to quenched disorder, and ii) whether the scenarios observed in random AF chains, such as infinite randomness and Griffiths-McCoy singularities, are valid for these more complicated quasi-one-dimensional models.

From our numerical calculations, we have found that for strong enough disorder the ladder models, like the random chains, generally become gapless. The dynamical exponent z of the models is generally non-universal i.e. it depends on the strength of disorder and on the value of the couplings. In random models where there is a competition between different types of phases, either due to staggered dimerization or due to frustration, such as in the J_1–

J_2 model, the critical behavior at the phase boundary is generally controlled by an infinite-randomness fixed point, at least for strong enough disorder. The low-energy properties of the systems near the infinite-randomness fixed point are known from asymptotically exact analytical calculations for random AF spin chains [41, 106]. From these one might presume that the general phase diagram consists of Griffiths-McCoy phases with different topological order separated by an infinite-randomness fixed point. The zig-zag ladder is an exception, where only one Griffiths-McCoy phase exists and the random critical point is located at its boundary.

Next we consider the crossover effects as the strength of disorder is varied. These problems can not be directly studied by the simple strong-disorder RG method. Nevertheless, from the sign of $z_{\rm random} - z_{\rm pure}$ obtained from our calculation and from other investigations on quantum spin chains [69, 75, 124], we may presume the following picture: Some gapped phases are stable against weak disorder, and they become gapless only if the strength of disorder exceeds some critical value. This scenario has been observed for the random conventional ladder discussed in Subsec. 7.4.1. On the other hand, for frustrated ladders, such as the zig-zag and the J_1–J_2 ladders, the system seems to be driven to a random gapless phase by any small amount of disorder. At a phase boundary, such as in the staggered dimerized ladder and the J_1–J_2 model, the random critical behavior is controlled by the infinite-randomness fixed point, probably for any small amount of disorder.

It is worth mentioning the similarity of the low-energy behavior of half-odd-integer $2S =$ odd (integer $2S =$ even) spin chains and that of odd n- (even n-) leg spin-1/2 ladders: It is generally believed that for gapless pure systems, like $2S = n =$ odd, strong enough disorder is expected to drive the system into the infinite-randomness fixed point. For $2S = n =$ odd ≥ 3, there is a limiting disorder strength, $D_c(n)$, below which the system is described by a conventional random fixed point with $z < \infty$; For $2S = n =$ even, both systems are gapped with weak disorder, and turn into a gapless Griffiths-McCoy phase for stronger disorder. While the random ladder stays in this conventional random phase for any strength of the disorder, the random spin chain will turn into infinite-randomness behavior at some finite limiting randomness. With frustration or dimerization, infinite randomness can also be found in two-leg ladders, as we have seen. Thus, one might hypothesize that random ladders with even and odd number of legs belong to different universality classes. To scrutinize this hypothesis the investigation of n-leg ladders with $n > 2$ should be performed.

As a final note: a random antiferromagnetic square lattice can be regarded as a ladder with infinite n legs. By increasing n the value of the limiting strength of disorder, $D_c(n)$, is expected to increase for both $n = \text{even}$ (for frustrated ladders) and $n = \text{odd}$. In the limit $n \to \infty$, $D_c(n)$ may tend to infinity, so that the critical behavior of that system is described by a conventional random fixed point. Work in this direction is in progress to verify this scenario and to obtain a general physical picture about the low-energy properties of random two-dimensional antiferromagnets.

Chapter 8

Summary

We have seen that the zero-temperature quantum phase transition in disordered systems is different in many aspects from the finite-temperature phase transition, driven by thermal fluctuations. Two of the most pronounced effects arising from quenched randomness on quantum phase transitions are activated dynamical scaling at transitions governed by an infinite-randomness fixed point, and the prominent Griffiths-McCoy singularities in the off-critical phases. We have studied these disorder effects in the low-dimensional quantum spin systems numerically, including the random transverse-field Ising model in one/two dimensions, in ladder geometry and various antiferromagnetic spin ladder models with strong disorder.

From the analytical point of view, quenched randomness can affect the critical behavior in different ways, characterized by its appearance in the low-energy limit. One of the most interesting scenario is so-called infinite randomness, which means the systems appears more and more random on lower and lower energy scales, so the relative magnitude of the inhomogeneities approaches infinity (or zero) [98, 105]. In the renormalization-group language, this kind of critical behavior is controlled by an infinite-randomness fixed point [98, 105]. One hallmark of infinite-randomness fixed points is activated dynamical scaling, i.e. the dynamical critical exponent z, which relates the scales of energy ε ($\sim$ 1/time) and length L conventionally via a power-law $\varepsilon \sim L^{-z}$, is infinite, thus one has instead an exponential relation $\varepsilon \sim \exp(-\text{const. } L^{\psi})$ with $\psi < 1$. Another feature of infinite-randomness fixed points is the different scaling behavior of the typical and average values of some quantities, e.g. the spatial correlation function, due to their very broad probability distributions. The quantum critical point of the solvable random transverse-field Ising spin chain is an example of such infinite-randomness fixed points [37, 49].

Away from the criticality, there are the so-called Griffiths-McCoy phases, in which the low-energy randomness is strong, but not infinite, and various susceptibilities diverge. These singularities arise from rare regions, which are more strongly coupled than average and exhibit local order. The low-energy excitations of these strongly coupled "clusters" are

related with the length scale—the typical spacing between clusters—via $\varepsilon \sim L^{-z}$, with z a nonuniversal finite dynamical exponent that varies continuously within the phase. It has turned out that the Griffiths-McCoy singularities can be parameterized by this dynamical exponent [49, 55].

Employing two powerful numerical tools — the continuous-imaginary-time cluster algorithm [99, 101] and the Ma-Dasgupta-Hu renormalization-group method [20, 21, 37, 49, 105], we have confirmed the remarkable analytical predictions [37, 49, 88] of the random transverse-field Ising spin chain, and found that the critical properties of the double chain and the two dimensions are also controlled by infinite-randomness fixed points. Moreover, the universality class of the double chain has been found to be the same as the single chain.

We have extended our numerical renormalization-group study to the random transverse-field Ising ferromagnets with broadly distributed random couplings J according to Lévy flight statistics: $P(\ln J) \sim (1+|\ln J|)^{-1-\alpha}$ with $\alpha > 1$. For sufficiently broad distributions of disorder, $\alpha < \alpha_c$, the critical properties are governed by a line of the infinite-randomness fixed points, where the critical exponents are no more universal, but vary continuously with the Lévy index α. For $\alpha > \alpha_c$, the broadness of the distributions is irrelevant, and the critical exponents turn into the same values as for the normal distributions. In one dimension, the critical value $\alpha_c = 2$, as well as the α-dependent exponents within $\alpha < \alpha_c$, can be obtained analytically through a mapping to surviving Riemann walks. In two dimensions, we have numerically found $\alpha_c \approx 4.5$. Thus, in the region $2 < \alpha < \alpha_c$, where the central limit theorem holds for $|\ln J|$, the broadness of the the distribution is relevant for the two dimensional case.

Another subject of this thesis is the effect of quenched disorder on the low-energy properties of various antiferromagnetic spin ladder models, including the conventional ladder model, the staggered dimerized ladder, the zig-zag ladder and the full ladder with rung and diagonal couplings. The pure (non random) antiferromagnetic spin ladders with various interchain couplings and dimerization have been investigated by [110, 74], and their phase diagrams and gapped spectrums are known. From our numerical study by the Ma-Dasgupta-Hu renormalization-group method, we have observed a general scenario for these ladder models: With strong enough disorder, the system undergoes a transition from a gapped phase with finite topological or dimer order to a gapless Griffiths-McCoy phase, in which the scaling of energy, as well as singularities of the dynamical quantities, are characterized by a nonuniversal finite dynamical exponent z — the similar scenario is known for the Heisenberg spin-1 chain [69, 75]. At the phase boundaries, separating topologically distinct Griffiths-McCoy phases the singular behavior of the disordered ladders has been found to be generally controlled by an infinite randomness fixed point.

So far, we have studied the random transverse-field Ising ferromagnet for $d \leq 2$ including the double chain and the Heisenberg antiferromagnetic spin ladders. In all models we investigated, Griffiths-McCoy singularities appear and the critical behavior is mostly governed by infinite-randomness fixed points. A natural question is whether such disorder

effects will also be found in the quantum Ising ferromagnets with dimensionality $d \geq 3$ and the Heisenberg antiferromagnets for $d \geq 2$. Detailed numerical work in these subjects is still lacking, nevertheless, unpublished data indicate that the infinite-randomness fixed point is stable in the three-dimensional random transverse-field Ising ferromagnet, but unstable towards a state with finite randomness for quantum random antiferromagnets with dimensionality $d \geq 2$ [105]. We are also interested in the antiferromagnetic spin ladders with more than two legs, in particular, the question about the crossover scenario from a two-leg ladder to a square lattice. Investigations in this direction will be in progress [129].

Appendix: Surviving probability of Lévy flights

In this Appendix we present some details about the persistence properties of Lévy flights, related to Chapter 6.

Consider the following sum

$$S_n = \sum_{j=1}^{n} x_j \ , \tag{A.1}$$

where the independent random variables, x_j, follow the same broad probability distribution, $\pi(x)$, which asymptotically behaves as

$$\pi(x) \underset{x\to\infty}{\simeq} px^{-(1+\alpha)} \ , \quad \pi(x) \underset{x\to-\infty}{\simeq} q|x|^{-(1+\alpha)} \ ,$$

with $1 < \alpha < 2$. We are interested in the probability distribution of S_n, $P(S,n)$, for large n. According to exact results [3], there is a limit distribution, $\widetilde{p}(u)\mathrm{du}$, in term of the variable, $u = S_n/l_n - c_n$, as $n \to \infty$. Here the normalization:

$$l_n = n^{1/\alpha} \ , \tag{A.2}$$

is the transverse fluctuation of the walk if we interpret $n = t$ as the (discrete) time and $S_{n=t}$ as the position of the walker in the transverse direction. The second normalization is given by

$$c_n = -n^{1-1/\alpha}\delta_{\mathrm{w}} \ , \tag{A.3}$$

where $\delta_{\mathrm{w}} = -\langle x \rangle$ is defined as the bias of the walk. For a small δ_{w} one obtains from the combination in (A.3) the scaling relation between time and bias as:

$$t \sim |\delta_{\mathrm{W}}|^{-\nu(\alpha)} \ , \quad \text{with } \nu(\alpha) = \frac{\alpha}{\alpha - 1} \ . \tag{A.4}$$

For a symmetric distribution, when $\pi(x)$ is an even function, thus $p = q$ and $\delta_{\mathrm{W}} = 0$, we have for the limit distribution:

$$\widetilde{p}(u) = L_{\alpha,0}(u) = \frac{1}{2\pi}\int_{-\infty}^{\infty} e^{iku-|k|^{\alpha}}\mathrm{dk} \ , \tag{A.5}$$

which has an expansion around $u = 0$

$$L_{\alpha,0}(u) = \frac{1}{\pi\alpha}\sum_{k=0}^{\infty}(-1)^k \frac{u^{2k}}{(2k)!}\Gamma\left(\frac{2k+1}{\alpha}\right) \tag{A.6}$$

and for large u it is asymptotically given by

$$L_{\alpha,0}(u) = \frac{1}{\pi}u^{-(1+\alpha)}\Gamma(1+\alpha)\sin(\pi\alpha/2)\ , \tag{A.7}$$

where $\Gamma(x)$ denotes the gamma function.

Consider next the surviving probability, $P_{\rm surv}(t, \delta_{\rm w})$, which is given by the fraction of those walks that have not crossed the starting position until $t = n$, i.e. $S_i > 0$ for $i = 1, 2, \ldots, n$. For a biased walk with $0 < |\delta_{\rm w}| \ll 1$, the asymptotic behavior of $P_{\rm surv}(n, \delta_{\rm w})$ is equivalent to that of a symmetric walk ($\delta_{\rm w} = 0$) but with a moving adsorbing boundary site, which has a constant velocity of $v = \delta_{\rm w}$. For the event with $S_i > vi$ for $i = 1, 2, \ldots, n$, the surviving probability is denoted by $F(n, v)$, and the probability for $S_n > vn$, irrespective of the previous steps, is denoted by $P(n, v)$, which is given by:

$$P(n, v) = \int_{nv}^{\infty} p(S, n)\mathrm{dS}\ . \tag{A.8}$$

Between the generating functions

$$F(z, v) = \sum_{n\geq 0} F(n, v)z^n \tag{A.9}$$

and

$$P(z, v) = \sum_{n\geq 1} \frac{P(n, v)}{n}z^n\ , \tag{A.10}$$

there is a useful relation suggested by Sparre Andersen [1, 2]:

$$F(z, n) = \exp\left[P(z, v)\right]\ , \tag{A.11}$$

which has been used recently in [104].

In the zero velocity case, $v = 0$, which is equivalent to the symmetric walk with $\delta_{\rm w} = 0$, we have $P(n, 0) = 1/2$. Consequently $P(z, 0) = -\frac{1}{2}\ln(1 - z)$ and $F(z, 0) = (1 - z)^{-1/2}$, from which one obtains for the final asymptotic result:

$$P_{\rm surv}(t, 0) = F(n, 0)\,|_{n=t} \sim t^{-\theta}\ , \quad \text{with } \theta = \frac{1}{2}\ . \tag{A.12}$$

Note that the persistence exponent, $\theta = 1/2$, is independent of the form of a symmetric probability distribution $\pi(x)$, thus it does not depend on the Lévy index α.

For $v > 0$, i.e. when the allowed region of the particle shrinks in time, the correction to $P(n,0) = 1/2$ has the functional form: $P(n,v) = 1/2 - g(\tilde{c})$, with $\tilde{c} = vn^{1-1/\alpha}$. Evaluating (A.8) with (A.6) one obtains in leading order, $P(n,v) = \frac{1}{2}\tilde{c}A(\alpha) + \mathcal{O}(\tilde{c}^3)$, with $A(\alpha) = \Gamma(1+1/\alpha)/\pi$. Then $(P(z,v) - P(z,0) \simeq A(\alpha)v\sum_{n\geq 1} z^n n^{-1/\alpha}$ is singular around $z \to 1^-$. Therefore, we have

$$F(z,v) \simeq (1-z)^{-1/2} \exp\left[-A(\alpha)v(1-z)^{-(1-1/\alpha)}\right] , \tag{A.13}$$

in leading order and close to $z = 1^-$. Here the second factor gives the more singular contribution to the surviving probability, which is in an exponential form:

$$\begin{aligned} P_{\rm surv}(t,\delta_{\rm W}) &\sim F(n,v)\,\big|_{v=\delta_{\rm w},n=t} \\ &\sim t^{-1/2} \exp\left[-\text{const}\,\delta_{\rm w} \mathrm{t}^{1-1/\alpha}\right] . \end{aligned} \tag{A.14}$$

For $v < 0$, i.e. when the allowed region of the particle increases in time, we consider the large $|v|$ limit and write (A.8) as $P(n,v) \simeq 1 - B(\alpha)\tilde{c}^{-\alpha} + \mathcal{O}(\tilde{c}^{-3\alpha})$ with $B(\alpha) = \Gamma(1+\alpha)\sin(\pi\alpha/2)/\pi\alpha$. In the large $|v|$ limit, we have then $P(z,v) = -\ln(1-z) - B(\alpha)|v|^{-\alpha}\sum_{n\geq 1} z^n n^{-\alpha}$, where the second term is convergent even at $z = 1$. As a result, the surviving probability remains finite as $n \to \infty$ and we obtain $F(n,v) \simeq 1 - \text{const}|v|^{-\alpha}$, for $|v| \gg 1$. For a small velocity, $0 < |v| \ll 1$, we can estimate $F(n,v)$ by the following reasoning. After $n = n_c$ steps, the distance between the adsorbing site and the starting point, $y_s = vn_c$, will exceed the size of transverse fluctuations of the walk in (A.2), $l_{tr} \sim n_c^{1/\alpha}$, with $n_c \sim |v|^{-\nu(\alpha)}$. Then the walker which has survived until n_c-steps with a probability of $n_c^{-1/2}$, will survive in the following steps with probability $\mathcal{O}(1)$. Consequently,

$$\lim_{t\to\infty} P_{\rm surv}(n,\delta_{\rm w}) \sim \lim_{n\to\infty} F(n,v)\,|_{v=\delta_{\rm w},n=t} \sim |\delta_{\rm w}|^{\nu(\alpha)/2} . \tag{A.15}$$

Bibliography

[1] E. Sparre Andersen, Math. Scand. **1**, 263 (1953).

[2] E. Sparre Andersen, Math. Scand. **2**, 195 (1954).

[3] B. V. Gnedenko and A.N. Kolmogorov, *Limit Distributions for Sums of Independent Random Variables* (Addison-Wesley, Reading, MA, 1954).

[4] H. F. Trotter, Proc. Am. Math. Soc. **10**, 545 (1959).

[5] R. P. Feynman and A.R. Hibbs, *Quantum Mechanics and Path Integrals*, (McGraw-Hill, Inc. 1965).

[6] B. M. McCoy and T. T. Wu, Phys. Rev. **176**, 631 (1968).

[7] B. M. McCoy and T. T. Wu, Phys. Rev. **188**, 982 (1968).

[8] B. M. McCoy, Phys. Rev. **188**, 1014 (1969).

[9] R. B. Griffiths, Phys. Rev. Lett. **23**, 17 (1969).

[10] B. M. McCoy, Phys. Rev. Lett. **23**, 383 (1969).

[11] R. J. Elliott, P. Pfeuty and C. Wood, Phys. Rev. Lett. **25**, 443 (1970).
R. J. Elliott and C. Wood, J. Phys. C **4**, 2359 (1971).

[12] P. Pfeuty and R. Elliot, J. Phys. C **4**, 2370 (1971).

[13] B. M. McCoy and T.T. Wu, *The two-dimensional Ising model*, Harvard University Press, Cambridge, Massachusetts, (1973).

[14] A. B. Harris, J. Phys. C **7**, 1671 (1974).

[15] A. B. Harris, J. Phys. C **7**, 3082 (1974).

[16] A. B. Harris, Phys. Rev. B **12**, 203 (1975).

[17] M. Suzuki, Progr. Theor. Phys. **56**, 1454 (1976).

[18] G. Theodorou and M.H. Cohen, Phys. Rev. Lett. **37**, 1014 (1976).

[19] M. C. Cross and D. S. Fisher, Phys. Rev. B **19**, 402 (1979).

[20] S. K. Ma, C. Dasgupta and C.-K. Hu, Phys. Rev. Lett. **43**, 1434 (1979).

[21] C. Dasgupta and S. K. Ma, Phys. Rev. B**22**, 1305 (1980).

[22] K. Binder, Z. Phys. B **43**, 119 (1981).

[23] F. D. M. Haldane, Phys. Lett. **93A**, 464 (1983).

[24] I. Peschel, Phys. Rev. B **30**, 6783 (1984).

[25] H. De Raedt and A. Lagendijk, Phys. Reports **127 N0. 4**, 233 (1985).

[26] See, for example, J. J. Sakurai, *Mondern Quantum Mechanics* (Benjamin/Cummings, Menlo Park, 1985).

[27] R. Shankar and G. Murthy, Phys. Rev. B **36**, 536 (1987).

[28] R. H. Swendsen and J.-S. Wang, Phys. Rev. Lett. **58**, 86 (1987).

[29] I. Affleck, T. Kennedy, E. H. Lieb and H. Tasaki, Phys. Rev. Lett. **59**, 799 (1987).

[30] S. Chakravarty, B. I. Halperin, and D. R. Nelson: Phys. Rev. B **39**, 2344 (1989).

[31] M. P. M. den Nijs and K. Rommelse, Phys. Rev. B **40**, 4709 (1989).

[32] K. Binder and J.-S. Wang, J. Stat. Phys. **55**, 87 (1989).

[33] U. Wolff, Phys. Rev. Lett. **62**, 361 (1989).

[34] D. J. Buttrey, J. D. Sullivan, and A. L. Rheingold, J. Solid. State Chem. **88**, 291 (1990).

[35] W. Wu, B. Ellmann, T. F. Rosenbaum, G. Aeppli and D.H. Reich, Phys. Rev. Lett. **67**, 2076 (1991).

[36] E. Dagotto, J. Riera and D. J. Scalapino, Phys. Rev. B **45**, 5744 (1992).

[37] D. S. Fisher, Phys. Rev. Lett. **69**, 534 (1992).

[38] H. G. Evertz, G. Lana and M. Marcu, Phys. Rev. Lett. **70**, 875 (1993).

[39] W. Wu, D. Bitko, T. F. Rosenbaum and G. Aeppli, Phys. Rev. Lett. **71**, 1919 (1993).

[40] A. H. Castro Neto, G. Castilla and B. Jones, Phys. Rev. Lett. **81**, 3531 (1993).

[41] D. S. Fisher, Phys. Rev. B **50**, 3799 (1994).

[42] M. Guo, R. N. Bhatt, and D. A. Huse, Phys. Rev. Lett. **72**, 4137 (1994).

[43] H. Rieger and A. P. Young, Phys. Rev. Lett. **72**, 4141 (1994).

[44] A. Crisanti and H.Rieger, J. Stat. Phys. **77**, 1087 (1994).

[45] B. Batlogg, S. W. Cheong, and L.W. Rupp Jr, Physica B **194-196**, 173 (1994).

[46] J. F. DiTusa, S. W. Cheong, J. H. Park, G. Aeppli, C. Broholm, and C. T. Chen, Phys. Rev. Lett. **73**, 1857 (1994).

[47] U.-J. Wiese and H.-P. Ying, Z. Phys. B **93**, 147 (1994).

[48] K. Kojima, A. Keren, L. P. Lee, G. M. Luke, B. Nachumi, W. D. Wu, Y. J. Uemura, K. Kiyono, S. Miyasaka, H. Takagi, and S. Uchida, Phys. Rev. Lett. **74**, 3471 (1995).

[49] D. S. Fisher, Phys. Rev. B **51**, 6411 (1995).

[50] M. J. Thill and D. A. Huse, Physica A **214**, 321 (1995).

[51] M. Hase, N. Koide, K. Manabe, Y. Sasago, K. Uchinokura and A. Sawa, Physica B **215**, 164 (1995).

[52] A. P. Young, *Lecture at StatPhys 19, Xiamen, China, August 1995.* ed. H. Bailin, (World Scientific, 1996).

[53] A. P. Young and H. Rieger, Phys. Rev. B**53**, 8486 (1996).

[54] S. R. White, Phys. Rev. B**53**, 52 (1996).

[55] H. Rieger and A.P. Young, Phys. Rev. B**54**, 3328 (1996).

[56] R. A. Hyman, K. Yang, R. N. Bhatt and S. M. Girvin, Phys. Rev. Lett. **76**, 839 (1996).
K. Yang, R. A. Hyman, R. N. Bhatt and S. M. Girvin, J. Appl. Phys. **79**, 5096 (1996).

[57] D. Bitko, T. F. Rosenbaum and G. Aeppli: Phys. Rev. Lett. **77**, 940 (1996).

[58] T. Senthil and S. N. Majumdar, Phys. Rev. Lett. **76**, 3001 (1996).

[59] T. Senthil and S. Sachdev, Phys. Rev. Lett. **77**, 5292 (1996).

[60] B. B. Beard, U. J. Wiese, Phys. Rev. Lett. **77**, 5130 (1996).

[61] N. V. Prokof'ev, B. V. Svistunov and I. S. Tupistyn, JETP Letters **64**, 911 (1996).

[62] For a review see: E. Dagotto and T. M. Rice, Science **271** 618 (1996).

[63] M. Hase, K. Uchinokura, R.J. Birgeneau, K. Hirota and G. Shirane, J. Phys. Soc. Jpn. **65**, 1392 (1996).

[64] B. Boechat, A. Sagnin, and M. A, Continentino, Solid State Commun. **98**, 411 (1996).

[65] B.K. Chakrabarti, A. Dutta and P. Sen, *Quantum Ising Phase and Transitions in Transverse Ising Models*, (Spinger, Berlin, 1996).

[66] J. Cardy, *Scaing and Renormalization in Statistical Physics*, (Cambridge University Press, 1996).

[67] P. Bak, *How nature works*, (Springer, New York, 1996).

[68] S. L. Sondhi, S.M. Girvin, J. P. Carini and D. Shahar, Rev. Mod. Phys. **69**, 315 (1997).

[69] R. A. Hyman and K. Yang, Phys. Rev. Lett. **78**, 1783 (1997).

[70] M. Fabrizio and R. Mélin, Phys. Rev. Lett. **78**, 3382 (1997).

[71] E. Westerberg, A. Furusaki, M. Sigrist and P.A. Lee, Phys. Rev. B**55**, 12578 (1997).

[72] M. C. Martin, M. Hase, K. Hirota and G. Shirane, Phys. Rev. B **56**, 3173 (1997).

[73] M. Fabrizio and R. Mélin, Phys. Rev. B **56**, 5996 (1997).

[74] M. A. Martin-Delgado, J. Dukelsky and G. Sierra, Phys. Lett. A 250, 431; N. Flocke, Phys. Rev. B **56**, 13673 (1997).

[75] C. Monthus, O. Golinelli, and Th. Jolicoeur, Phys. Rev. Lett. **79**, 3254 (1997).

[76] M. Fabrizio and R. Mélin, J. Phys.:Condens. Matter **9**, 10429 (1997).

[77] H. Rieger and F. Iglói, Europhys. Lett. **39**, 135 (1997).

[78] F. Iglói and H. Rieger, Phys. Rev. Lett. **78**, 2473 (1997).

[79] F. Iglói, L. Turban, D. Karevski and F. Szalma, Phys. Rev. B**56**, 11031 (1997).

[80] A. P. Young, Phys. Rev. B**56**, 11691, (1997).

[81] T. Miyazaki, M. Troyer, M. Ogata, K. Ueda and D. Yoshioka, J. Phys. Soc. Jpn. **66**, 2580 (1997).

[82] H. Rieger and A.P. Young, *Complex Behaviour of Glassy Systems*, ed. M. Rubí and C. Pérez-Vicente, p. 256 (Springer, Heidelberg, 1997).

[83] E. Orignac and T. Giamarchi, Phys. Rev. B**57**, 5812 (1998).

[84] F. Iglói and H. Rieger, Phys. Rev. B**57**, 11404 (1998).

[85] P. Henelius and S. M. Girvin, Phys. Rev. B **57**, 11457 (1998).

[86] C. Monthus, O. Golinelli, and Th. Jolicoeur, Phys. Rev. B **58**, 805 (1998).

[87] D. S. Fisher and A. P. Young, Phys. Rev. B **58**, 9131 (1998).

[88] F. Iglói and H. Rieger, Phys. Rev. E**58**, 4238 (1998).

[89] K. Manabe, H. Ishimoto, N. Koide, Y. Sasago, and K. Uchinokura, Phys. Rev. B **58**, R575 (1998).

[90] T. Masuda, A. Fujioka, Y. Uchiyama, I. Tsukada, and K. Uchinokura, Phys. Rev. Lett. **80**, 4566 (1998).

[91] C. Pich, A.P. Young, H. Rieger and N. Kawashima, Phys. Rev. Lett. **81**, 5916 (1998). C. Pich and A.P. Young, preprint cond-mat/9802108 (1998).

[92] T. Ikegami, S. Miyashita und H. Rieger, J. Phys. Soc. Jap. **67**, 2761 (1998).

[93] R. N. Bhatt, *Spin Glasses and Random Fields*, ed. A.P. Young p. 225 (World Scientific, Singapore, 1998).

[94] D. Karevski, R. Juhász, L. Turban and F. Iglói, Phys. Rev. B **60**, 4195 (1999).

[95] F. Iglói, L. Turban and H. Rieger, Phys. Rev. E **59**, 1465 (1999).

[96] Y. Ichiyama, Y. Sasago, I. Tsukuda, K. Uchinokura, A. Zheludev, T. Hayashi, N. Miura, and P. Boni, Phys. Rev. Lett. **83**, 632 (1999).

[97] K. Hida, Phys. Rev. Lett. **83**, 3297 (1999).

[98] D. S. Fisher, Physica A **263**, 222 (1999).

[99] H. Rieger und N. Kawashima, Europ. Phys. J. B **9**, 135 (1999).

[100] H. Rieger Comp. Phys. Comm. **121-122**, 505 (1999).

[101] H. Rieger and F. Iglói, Phys. Rev. Lett. **83**, 3741 (1999).

[102] H. Rieger and F. Iglói, Europhys. Lett. **45**, 673 (1999).

[103] F. Iglói, R. Juhász and H. Rieger, Phys. Rev. B **59**, 11308 (1999).

[104] M. Bauer, C. Godreche and J .M. Luck, J. Stat. Phys. **96**, 963 (1999).

[105] O. Motrunich, S.-C. Mau, D.A. Huse and D.S. Fisher, Phys. Rev. B **61**, 1160 (2000).

[106] F. Iglói, R. Juhász and H. Rieger, Phys. Rev. B **61**, 11552 (2000).

[107] C. Payen, E. Janod, K. Schoumacker, C. D. Batista, K. Hallberg, and A.A. Aligia, Phys. Rev. B **62**, 2998 (2000).

[108] K. Yang and R. A. Hyman, Phys. Rev. Lett. **84**, 2044 (2000).

[109] Y.-C. Lin, N. Kawashima, F. Iglói and H. Rieger, Prog. Th. Phys. (Suppl.) **138**, 470 (2000).

[110] E. H. Kim, G. Fáth, J. Sólyom and D. J. Scalapino, Phys. Rev. B **62**, 14965 (2000).

[111] R. Mélin, Eur. Phys. J. B **16**, 261 (2000).

[112] R. Mélin, Eur. Phys. J. B **18**, 263 (2000).

[113] D. P. Landau and K. Binder, *A Guide to Monte Carlo Simulations in Satistical Physics*, (Cambridge Unversity Press, 2000).

[114] D. Karevski, Y.-C. Lin, H. Rieger, N. Kawashima and F. Iglói, Eur. Phys. J. B**20**, 267 (2001).

[115] F. Iglói, R. Juhász and P. Lajkó, Phys. Rev. Lett. **86**, 1343 (2001).

[116] M. I. Marqués and J. A. Gonzalo, Phys. Rev. E **63**, 056114 (2001).

[117] O. Motrunich, K. Damle and D. A. Huse, Phys. Rev. E **63**, 134424 (2001).

[118] S. Sachdev, *Quantum Phase Transitions*, (Cambridge Unversity Press, 2001).

[119] N.V. Prokof'ev, B. V. Svistunov, I. S. Tupistyn, preprint cond-mat/9703200 (1997).

[120] M. Azuma, M. Takano, R. S. Eccleston, preprint cond-mat/9706170 (1997).

[121] A. O. Gogolin, A. A. Nersesyan, M. Tsevlik and L. Yu, preprint cond-mat/9707341 (1997).

[122] M. S. L. du Croo de Jongh and J. M. J. van Leeuwen, preprint cond-mat/9709103 (1997).

[123] D. Belitz and T. R. Kirkpatrick, preprint cond-mat/9811058 (1998).

[124] E. Carlon, P. Lajkó and F. Iglói, preprint cond-mat/0106325 (2001).

[125] V. Villar, R. Mélin, C. Paulsen, J. Souletie, E. Janod, and C. Payen, priprint cond-mat/0107294 (2001).

[126] F. Iglói, preprint cond-mat/0108350.

[127] R. Mélin, Y.-C. Lin, P. Lajkó, H. Rieger, and F. Iglói, accepted by Phys. Rev. B for publication.

[128] N. Kawashima and F. Iglói (unpublished).

[129] R. Mélin et al (unpublished).

Acknowledgments

I would like to thank

- Prof. Heiko Rieger and Prof. Ferenc Iglói for supervising this thesis, and many stimulating suggestions and comments. I am especially grateful to Prof. Heiko Rieger for a critical reading of the manuscript.
- the co-workers of our publications.
- Prof. P. Grassberger for kindly permitting me to stay in his research group in NIC throughout my PhD study.
- all members in NIC for providing a pleasant working atmosphere.
- Dr. Vishal Mehra for correcting the manuscript, and Beate Kraus for many suggestions on German composition.

I gratefully acknowledge financial support from Forschungszentrum Jülich.

Zusammenfassung

Reale physikalische Systeme weisen stets ein gewisses Maß an Unordnung auf. Der Einfluss von Unordnung, insbesondere von eingefrorener Unordnung, auf das kollektive Verhalten eines physikalisches Systems bei Phasenübergängen ist ein faszinierendes Untersuchungsgebiet im Rahmen der Festkörperphysik. Für Quantenphasenübergänge, die bei verschwindender Temperatur durch quantenmechanische Fluktuationen hervorgerufen werden, sind die Effekte der Unordnung besonders drastisch. In diesem Zusammenhang sind neue physikalische Phänomene bei Quantenspinsystemen entdeckt und in den letzten Jahren intensiv untersucht worden.

Theoretische Untersuchungen deuten darauf hin, dass die Wechselwirkungen zwischen Unordnung und Quantenfluktuationen am kritischen Punkt zu aktivierter Dynamik führen können, was bedeutet, dass die Zeitskalen am kritischen Punkt exponentiell divergieren. Der dynamische Exponent, der die Zeitskalen und die Längenskalen verbindet, ist hier also unendlich. Der kritische Punkt dieser Art wird als ein Fixpunkt unendlicher Unordnung (infinite-randomness fixed point) benannt. Unter unendlicher Unordnung versteht man, dass die relative Größenordnung der Inhomogenität im System unendlich ist. Dieses Szenario ist bisher aufgrund analytischer Überlegungen für einige eindimensionale ungeordnete Quantenspinsysteme bekannt. Es handelt sich beispielsweise um die ungeordneten Ising-Ketten im transversalen Magnetfeld sowie die ungeordneten antiferromagnetischen Heisenberg-Ketten.

Ein weiterer wichtiger Aspekt ungeordneter Systeme ist das Auftreten von vereinzelten ordnenden Regionen in der Phase, in der dem ganzen System keine langreichweitige Ordnung vorliegt: Anhand eines ungeordneten Magneten liefert eine solche lokale ferromagnetische Ordnung große Beiträge zur Suszeptibilität und kann deren Singularitäten in der paramagnetischen Phase verursachen. Diese Phänomene werden Griffiths-McCoy-Singularitäten genannt. Obwohl der Effekt sich nicht nur auf das Quantenregime beschränkt, ist er in der Nähe eines Quantenphasenübergangs doch weitaus spektakulärer als bei klassischen Phasenübergängen. Der Grund dafür liegt in der Verbündung von Statik und Dynamik in den Quantensystemen. In der Pfadintegral-Darstellung lässt sich ein d-dimensionales Quantensystem auf ein effektives (d+1)-dimensionales klassisches Modell mit einer zusätzlichen imaginären Zeitdimension abbilden. So wird sich eine geordnete Region, die wie ein räumlich punktartiger Defekt im klassischen Modell ist, in die Zeitrichtung entwickeln

und es wird sich eine Linie ergeben. Die Wirkungen derartiger vereinzelter Regionen sind dadurch in den Quantensystemen besonders ausgeprägt.

Die Untersuchungen ungeordneter Quantenspinsysteme im Zusammenhang mit den obengenannten Phänomenen stellen den Schwerpunkt dieser Arbeit dar. Die Thematik wurde aus numerischen Aspekten anhand des Ising-Ferromagneten im transversalen Feld und der antiferromagnetschen Heisenberg-Spin-Leitern betrachtet. Für den transversalen Ising-Ferromagneten wurden zunächst die Quanten-Monte-Carlo-Simulationen mittels eines von Rieger und Kawashima neu entwickelten Cluster-Algorithmus in kontinuierlicher imaginärer Zeit implementiert. Die daraus gewonnenen Ergebnisse wurden sodann mit numerischen Ma-Dasgupta-Hu Renormierungsgruppen-Rechnungen verglichen. Wir erweiterten unsere Renormierungsgruppen-Rechnungen auf einen speziellen Fall für den transversalen Ising-Ferromagneten, in dem die Unordnung gemäß der Lévy-Verteilung angeordnet ist. Zum Schluss wurden die antiferromagnetischen Heisenberg-Spin-Leitern mit Hilfe der Renormierungsgruppen-Rechnungen untersucht.

Die einzelnen Teile dieser Arbeit lassen sich wie folgt zusammenfassen:

Nach einem einführenden Kapitel befassen sich Kapitel 2 und 3 mit den Quanten-Monte-Carlo-Simulationen an ein- und zweidimensionalen Ising-Ferromagneten im transversalen Feld. Das Quantensystem in der Pfadintegral-Darstellung – in Verbindung mit der Trotter-Formel, die das Problem der nichtkommutierenden Operatoren eliminieren kann – wird auf ein klassisches Ising-Modell mit einer neu eingeführten imaginären Zeitdimension abgebildet, wobei die Länge der Zeitdimension der inversen Temperatur des Quantensystems entspricht. Das effektive klassische System lässt sich gut mit Monte-Carlo-Methoden simulieren. Jedoch ist die Äquivalenz zwischen dem Quantensystem und dem effektiven klassischen Modell erst exakt, wenn sich der infinitesimale Abstand zweier imaginärer Zeitscheiben nach Null (Trotter-Limes) extrapolieren lässt. Diese Extrapolation wird in dem in unseren Simulationen eingesetzten Cluster-Algorithmus in kontinuierlicher imaginärer Zeit implizit durchgeführt. Zu beachten ist, dass der Algorithmus auf dem Swendsen-Wang-Cluster-Verfahren basiert und damit erheblich weniger von Equilibrierungsproblemen im kritischen Bereich betroffen ist als die lokalen Algorithmen.

Was das ungeordnete Quantenspinsystem betrifft, ist das effektive klassische Modell anisotrop, d.h. die Raumdimensionen und die imaginäre Zeitdimension zeigen ein unterschiedliches Finite-Size-Skalenverhalten. Es handelt sich daher um mehr Skalen-Variablen bei der Exponentenbestimmung. Unter Zuhilfenahme des dimensionslosen Binder-Kumulanten und seiner Systemgrößenabhängigkeit konnten wir den kritischen dynamischen Exponenten bestimmen und daraus die entscheidende Schlussfolgerung ziehen, dass das kritische Verhalten der transversalen Ising-Ferromagneten in Zweidimensionen sowie in Eindimension von einem Fixpunkt unendlicher Unordnung bestimmt ist.

Kapitel 4 beleuchtet die Arbeit mit der Ma-Dasgupta-Hu Renormierungsgruppen(RG)-Methode. Sie eignet sich, sowohl analytisch als auch numerisch, für die Untersuchung jener Quantensysteme im Bereich niedriger Energien, die eine starke Unordnung aufweisen,

vor allem solche, in denen ein Fixpunkt unendlicher Unordnung vorliegt. Bei der Renormierung werden die stärksten Energie-Einheiten des Hamilton-Operators iterativ dezimiert und gemäß der Störungstheorie durch schwächere Terme ersetzt. Diese RG-Prozedur führt im Endeffekt zu einem System mit weniger Spins, geänderten Kopplungen und einer niedrigeren Energie-Skala. Die renormierten Kopplungen bei jedem Schritt sind voneinander unabhängig, so dass sich die sich ergebende Verteilung der Kopplungen, genau gesagt der logarithmischen Kopplungen, mit immer niedrigeren Energie-Skalen allmählich verbreitert. Die Approximation der Störungstheorie ist hierdurch verbessert, da die zu dezimierenden Terme mit höchster Wahrscheinlichkeit viel größer als ihre Nachbarn sind, welche wir bei der Renormierung als Störungen behandeln. Für einen Fixpunkt unendlicher Unordnung ist die relative Größenordnung zweier benachbarter Termen unendlich oder Null. In diesem Limes sind die RG-Rechnungen also asymptotisch exakt, weil die zu dezimierenden Terme absolut dominiert sind.

In Kapitel 5 präsentieren wir die aus unseren numerischen RG-Rechnungen gewonnenen Ergebnisse für die ungeordneten transversalen Ising- Ferromagneten in Eindimension, in einer Leiter-Geometrie (Doppelkette) und in Zweidimensionen. Es wird aufgezeigt, dass die Doppelketten zu derselben Universalitäts-Klasse wie die Einfachketten gehören; die sich ergebenden kritischen Exponenten für das zweidimensionale System stimmen gut mit den Ergebnissen aus den Monte-Carlo-Simulationen überein. Darüber hinaus wurden die Griffiths-McCoy-Singularitäten untersucht. Der dynamische Exponent, der die Griffiths-McCoy-Singularitäten charakterisiert, wurde in Abhängigkeit von der Distanz zum kritischen Punkt bestimmt.

Kapitel 6 befasst sich mit dem Thema der Lévy-Verteilung anhand des transversalen Ising-Ferromagneten in Ein- und Zweidimensionen. Im Gegensatz zur den Untersuchungen bis Kapitel 5, wo sich die Verteilungen der Unordnung als regulär präsentierten, ist die Lévy-Verteilung sehr breit. Mit einer Unordnungs-Verteilung dieser Art wird das kritische Verhalten des Systems nicht nur von einem einzigen Fixpunkt bestimmt, sondern von einer Reihe von Fixpunkten. Die kritischen Exponenten in diesem Fall sind von den Anfangsbedingungen der Verteilung abhängig. Durch Abbildung auf ein Random-Walk-Problem kann man die Abhängigkeiten der kritischen Exponenten vom Lévy-Index, der die Anfangsbedingungen der Verteilung parametrisiert, analytisch exakt bestimmen. Solange der Lévy-Index kleiner als ein kritischer Wert bleibt, ist die Breite der Lévy-Verteilung relevant und variieren die kritischen Exponenten mit dem Lévy-Index. Oberhalb des kritischen Wertes bleiben die kritischen Exponenten konstant und sind identisch mit denen für eine reguläre Verteilung. Solche Abhängigkeiten vom Lévy-Index für den zweidimensionalen Fall wurden mittels der numerischen RG-Rechnungen untersucht. Wie die Ergebnisse zeigen, liegt der kritische Wert des Lévy-Indexes für das zweidimensionale System weiter höher als für den eindimensionalen Fall, was bedeutet, dass die Breite der Verteilung in einem größeren Bereich des Lévy-Indexes für das zweidimensionale System relevant ist.

In Kapitel 7 diskutieren wir unsere Untersuchungen an antiferromagnetischen Heisenberg-Spin-Leitern mit Spin-1/2. Die Spin-Leiter-Systeme sind in den letzten Jahren intensiv un-

tersucht worden. Ein Grund dafür ist sicher ihre experimentelle Realisierbarkeit. Vom theoretischen Aspekt her betrachtet, sind Spin-Leitern mit Spin-1/2 analoge Objekte zur Spin-Kette mit Spin-1. Letztere weist in Abwesenheit der Unordnung ein Energie-Spektrum mit einem Gap — dem Haldane-Gap — auf. Nach Untersuchungen anhand der modifizierten RG-Methoden, die speziell für Systeme mit Spin-1 entwickelt wurden, meint man sagen zu können, dass die starke Unordnung das Haldane-Gap zerstören kann und im extremen Fall das System in eine — von den oben genannten Fixpunkten unendlicher Unordnung kontrollierte — Random-Singlet-Phase versetzt, wo die Spins sich paareweise in einen Singulettzustand einfinden. Mit Hilfe der numerischen RG-Verfahren haben wir Spin-Leitern mit starker Unordnung in verschiedenen Modellen untersucht: konventionelle Leitern, dimerisierte Leitern, Zig-Zag-Leitern und Leitern mit diagonalen Kopplungen. Die Resultate zeigen, dass die Gaps in jedem Modell bei starker Unordnung gefüllt werden und das System sich dadurch in einer Griffiths-McCoy-Phase befindet. Die Phasen-Grenze zwischen zwei topologisch unterschiedlichen Griffiths-McCoy-Phasen wird im allgemeinen von einem Fixpunkt unendlicher Unordnung kontrolliert.

Im letzten Kapitel wird eine Zusammenfassung gegeben.

Abstract

The effects of quenched disorder on the low-energy properties of quantum spin systems in low dimensions are studied numerically by quantum Monte Carlo simulations and the Ma-Dasgupta-Hu renormalization group scheme. The algorithm used for the Monte Carlo simulations combines the Swendsen-Wang cluster update method and the continuous time algorithm, and can simulate the effective classical model of the quantum system efficiently; The Ma-Dasgupta-Hu renormalization group based on the perturbation theory is designed to be accurate for strongly disordered systems. We focus on the critical behavior, as well as the Griffiths-McCoy singularities, of the random transverse-field Ising model and various antiferromagnetic spin ladders with strong disorder.

Kurzzusammenfassung

Die Effekte der eingefrorenen Unordnung auf physikalische Eigenschaften der Quantenspinsysteme im Bereich niedriger Energien bzw. Temperaturen werden mittels der Quanten-Monte-Carlo-Simulationen und der Ma-Dasgupta-Hu Renormierungsgruppen-Methode numerisch untersucht. Für die Monte-Carlo-Simulationen wird ein Cluster-Algorithmus in kontinuierlicher imaginärer Zeit eingesetzt, mit dem das zum Quantensystem äquivalente klassische Modell effizient simuliert werden kann. Die Ma-Dasgupta-Hu Renormierungsgruppen-Methode, die auf einer Störungstheorie basiert, zeigt ihre Genauigkeit vor allem in stark ungeordneten Systemen. Wir untersuchen das vom Fixpunkt unendlicher Unordnung kontrollierte kritische Verhalten und die Griffiths-McCoy-Singularitäten anhand von Ising-Ferromagneten im transversalen Feld und antiferromagnetischen Spinleitern.

Ich versichere, daß ich die von mir vorgelegte Dissertation selbständig angefertigt, die benutzten Quellen und Hilfsmittel vollständig angegeben und die Stellen der Arbeit - einschließlich Tabellen, Karten und Abbildungen -, die anderen Werken im Wortlaut oder dem Sinn nach entnommen sind, in jedem Einzelfall als Entlehnung kenntlich gemacht habe; daß diese Dissertation noch keiner anderen Fakultät oder Universität zur Prüfung vorgelegen hat; daß sie - abgesehen von unten angegebenen Teilpublikationen - noch nicht veröffentlicht worden ist sowie, daß ich eine solche Veröffentlichung vor Abschluß des Promotionsverfahrens nicht vornehmen werde. Die Bestimmungen dieser Promotionsordnung sind mir bekannt. Die von mir vorgelegte Dissertation ist von Prof. H. Rieger betreut worden.

Köln, den 25. September 2001

Yu-Cheng Lin

Teilpublikationen:

- Y.-C. Lin, N. Kawashima, F. Iglói und H. Rieger:
  Numerical renormalization group study of random transverse Ising models in one and two space dimensions,
  Prog. Theor. Phys. **138** (Suppl.), 470 (2000).
- D. Karevski, Y.-C. Lin, H. Rieger, N. Kawashima und F. Iglói:
  Random quantum magnets with broad disorder distribution,
  Europ. Phys. J. B **20**, 267 (2001).
- R. Mélin, Y.-C. Lin, P. Lajkó, H. Rieger und F. Iglói:
  Strongly disordered spin ladders, Preprint, eingereicht bei Phys. Rev. B (2001).

Already published:

Modern Methods and Algorithms of Quantum Chemistry - Proceedings
Johannes Grotendorst (Editor)
NIC Series Volume 1
Winterschool, 21 - 25 February 2000, Forschungszentrum Jülich
ISBN 3-00-005618-1, February 2000, 562 pages
out of print

Modern Methods and Algorithms of Quantum Chemistry - Poster Presentations
Johannes Grotendorst (Editor)
NIC Series Volume 2
Winterschool, 21 - 25 February 2000, Forschungszentrum Jülich
ISBN 3-00-005746-3, February 2000, 77 pages
out of print

Modern Methods and Algorithms of Quantum Chemistry - Proceedings, Second Edition
Johannes Grotendorst (Editor)
NIC Series Volume 3
Winterschool, 21 - 25 February 2000, Forschungszentrum Jülich
ISBN 3-00-005834-6, December 2000, 638 pages

Nichtlineare Analyse raum-zeitlicher Aspekte der hirnelektrischen Aktivität von Epilepsiepatienten
Jochen Arnold
NIC Series Volume 4
ISBN 3-00-006221-1, September 2000, 120 pages

Elektron-Elektron-Wechselwirkung in Halbleitern: Von hochkorrelierten kohärenten Anfangszuständen zu inkohärentem Transport
Reinhold Lövenich
NIC Series Volume 5
ISBN 3-00-006329-3, August 2000, 145 pages

Erkennung von Nichtlinearitäten und wechselseitigen Abhängigkeiten in Zeitreihen
Andreas Schmitz
NIC-Serie Volume 6
ISBN 3-00-007871-1, May 2001, 142 pages

Multiparadigm Programming with Object-Oriented Languages - Proceedings
Kei Davis, Yannis Smaragdakis, Jörg Striegnitz (Editors)
NIC-Serie Volume 7
Workshop MPOOL, 18 May 2001, Budapest
ISBN 3-00-007968-8, June 2001, 160 pages

Europhysics Conference on Computational Physics - Book of Abstracts
Friedel Hossfeld, Kurt Binder (Editors)
NIC-Serie Volume 8
Conference, 5 - 8 September 2001, Aachen
ISBN 3-00-008236-0, September 2001, 500 pages

NIC Symposium 2001 - Proceedings (in preparation)
Horst Rollnik, Dietrich Wolf (Editors)
NIC-Serie Volume 9
Symposium, 5 - 6 December 2001, Jülich, Germany
ISBN 3-00-009055-X

Quantum Simulations of Complex Many-Body Systems: From Theory to Algorithms - Lecture Notes
Johannes Grotendorst, Dominik Marx, Alejandro Muramatsu (Editors)
NIC Series Volume 10
Winter School, 25 February - 1 March 2002, Rolduc Conference Centre, Kerkrade, The Netherlands
ISBN 3-00-009057-6, February 2002, 548 pages

Quantum Simulations of Complex Many-Body Systems:
From Theory to Algorithms- Poster Presentations

Johannes Grotendorst, Dominik Marx, Alejandro Muramatsu (Editors)
NIC Series Volume 11
Winter School, 25 February - 1 March 2002, Rolduc Conference Centre,
Kerkrade, The Netherlands
ISBN 3-00-009058-4, February 2002, 88 pages